Title

MOLECULAR BEAMS STUDIES OF THE ENERGETICS AND DYNAMICS OF ELEMENTARY CHEMICAL REACTIONS

Author

Hayden, C.C.

Publication Date

1982-05-01

LBL-13660

Lawrence Berkeley Laboratory
UNIVERSITY OF CALIFORNIA

Materials & Molecular Research Division

MOLECULAR BEAMS STUDIES OF THE ENERGETICS AND DYNAMICS OF ELEMENTARY CHEMICAL REACTIONS

Carl Clay Hayden
(Ph.D. thesis)

May 1982

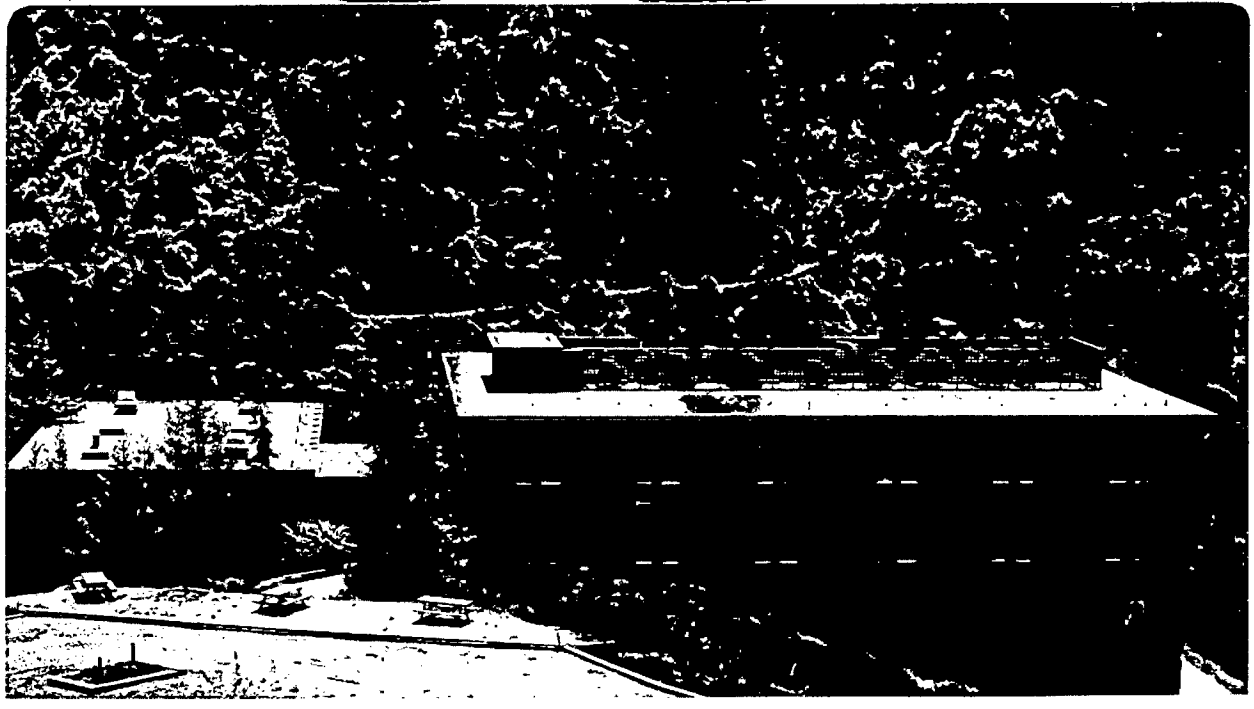

Prepared for the U.S. Department of Energy under Contract DE-AC03-76SF00098

DISCLAIMER

LBL-13660

Molecular Beams Studies of the Energetics and Dynamics of Elementary Chemical Reactions

Carl Clay Hayden
Ph.D. Thesis

Lawrence Berkeley Laboratory
University of California
Berkeley, California

This work was supported by the Director, Office of Energy Research, Office of Basic Energy Science, Chemical Sciences Division of the U. S. Department of Energy under Contract No. DE-AC03-76SF00098, and by the Office of Naval Research under Contract No. N00014-75-C-0671.

Contents

Molecular Beams Studies of the Energetics and Dynamics of Elementary Chemical Reactions

Carl Clay Hayden
Ph.D. Thesis

Lawrence Berkeley Laboratory
University of California
Berkeley, California

ABSTRACT

Quantum mechanical effects on the angular distribution of HF products from the F + H_2 reaction were studied using crossed atomic and molecular beams with a rotatable mass spectrometer detector and time-of-flight velocity analysis. Measurement of the singlet-triplet splitting of CH_2 from the recoil velocities of fragments from ketene photodissociation in a molecular beam are also reported.

Partial center-of-mass angular distributions, and velocity flux contour maps have been derived for individual vibrational states of the HF product from the F + H_2 reaction at collision energies of 2 and 3 kcal/mole. The center-of-mass distributions were obtained by analysis of laboratory angular and time-of-flight measurements of the reactive scattering. The results are consistent with recent three dimensional quantum mechanical scattering calculations, which predict that resonance effects should appear in the product angular distributions in this energy range.

The photofragmentation of ketene in a molecular beam was used to measure the singlet-triplet splitting in CH_2. A rare gas halide excimer laser operating at 351 nm (XeF) and 308 nm (XeCl) dissociated the ketene. Time-of-flight measurements of the fragment velocities allowed determination of the energetics of the dissociation. The

$^1A_1 - {}^3B_1$ splitting in CH_2 was found to be 8.5 ± 0.8 kcal/mole. This agrees with many experimental results, but not with the value of 19.5 kcal/mole derived from recent photodetachment experiments on CH_2^-.

Acknowledgements

I would like to express my thanks to Prof. Yuan T. Lee for the privilege of being a member of his research group. His unique combination of patience and enthusiasm accommodates the varied personal styles of all the people in the group. A number of other people contributed to the work reported here. Randy Sparks was responsible for most of the design and construction of the apparatus used in these experiments. I worked closely with him and Kosuke Shobatake for a long time on the $F + H_2$ experiment. Kosuke also wrote the original versions of the computer programs for the data analysis. Dan Neumark and I spent many days and nights together both taking and analyzing most of the data presented here. He brought a new perspective on how to do the experiments, and understand the results.

I've had the pleasure of working with several other people during my time as a graduate student. Manfred Faubel taught me many of the basic ideas of molecular beams experiments. He was instrumental in providing the background knowledge necessary for later projects. I worked with Matt Vernon on elastic scattering, and he instructed me (with excellent volume) on the details of putting together computer programs. John Hepburn and I built an apparatus to do multiphoton ionization, and from him I learned about dye lasers and light collection. I also appreciated his constant good humor. The entire research group has provided a stimulating atmosphere and a continuing source of entertainment for the years I've been associated with it. Doug Krajnovich in particular has given my attitude periodic adjust-

ments when it was needed. Ms. June DeLaVergne did an extremely accurate and fast job of typing, and her help greatly eased the preparation of this manuscript. Last, but perhaps most importantly, I would like to thank my parents and the other members of my family for their understanding and support. I am very grateful to them.

This work was supported by the Director, Office of Energy Research, Office of Basic Energy Sciences, Chemical Sciences Division of the U. S. Department of Energy under Contract No. DE-AC03-76SF00098 and by the Office of Naval Research under Contract No. N00014-75-C-0671. The rare gas halide laser used in this research was a loan from the San Francisco Laser Center supported by the National Science Foundation under Grant No. CHE79-16250 awarded to the University of California at Berkeley in collaboration with Stanford University.

I. REACTIVE SCATTERING OF F WITH H_2

INTRODUCTION

The $F + H_2 \rightarrow HF + H$ reaction is one of the simplest examples of a highly exoergic chemical reaction. A variety of experimental methods have been used to determine both the absolute overall rate constant, and relative state to state probabilities for this reaction. These quantities, and some other characteristics of the reaction, have also been the object of numerous theoretical calculations. Even for this simple reaction, the dynamics have proved to be sufficiently complicated that many features are either unknown or poorly understood.

The most striking aspect of the $F + H_2$ reaction is the inversion of the vibrational state populations in the HF products. Of course this is the reason for much of the interest in the $F + H_2$ system since a powerful chemical laser can be built using it as the pumping reaction. Many measurements have been made of the energy distribution in the reaction products to determine detailed rates for product formation in various quantum states. Chemical laser[1,2,3] and infrared chemiluminescence experiments[4,5,6,7] have given product vibrational distributions at several temperatures (Table 1) and there is fair agreement among values determined by different methods. Infrared chemiluminescence has also been used to determine product rotational state distributions for HF V = 1,2 and 3.

The use of para hydrogen in the reaction has shown that the rotational state of the reactant H_2 influences the vibrational energy distribution in the products. With para hydrogen a significantly higher fraction of the available energy appears in product vibration.[8] Infra-

red chemiluminescence measurements using para hydrogen in the reaction at two different temperatures have made it possible to resolve the effects of individual rotational states.[6] The reaction with H_2 J = 1 yields products with somewhat less population in V = 3, but this trend is reversed between J = 1 and J = 2 at 290 °K with J = 2 giving a larger fraction of product in V = 3.

Measurements of the overall rate constant for the F + H_2 reaction[9-14] using different methods and over different temperature ranges have not agreed very well. Values for the activation energy range between 510 and 2470 cal, with Arrhenius preexponential factors between 9.2×10^{-11} and 2.7×10^{-10} cm^3/molecule-sec. The most recent direct measurements[12,13,14] all gave activation energies below 1.2 kcal/mole. The actual values for the rate constant from those studies agree within about a factor of two over the temperature range covered.

The experimental work mentioned has revealed several characteristics of the dynamics of the F + H_2 reaction. The overall reaction has a small activation energy, indicating there is a low barrier to the reaction. Increasing the reagent temperature tends to decrease the fraction of the available energy appearing in product vibration and increases the energy in product rotation.[7] The effect of reagent rotation is difficult to determine separately from changes in translational energy, but there certainly is evidence that the rotational states of the reactants significantly influence the vibrational distribution of the products.

A great deal of effort has been directed toward explaining these results by comparison with various types of calculations. An accurate

potential energy surface is an important prerequisite for calculations of collision dynamics. Most of the surfaces proposed are of the LEPS[15] or generalized LEPS[16] form with parameters adjusted to fit some experimental results. Actually, some of the classical dynamics calculations were attempts to derive the potential from experimental results. The features common to all the ground state surfaces used for studying the $F + H_2$ reaction are an exothermicity of about 32 kcal/mole, and a small barrier to the reaction for a collinear approach of F to H_2 with an increasing barrier as the configuration departs from linear.

A surface derived by Muckerman,[17] designated M5, is the most widely used for dynamics studies. It was determined from a two parameter LEPS form with the requirements that it yield a transition state theory activation energy of 1.71 kcal/mole, which was the best experimental value[18,19] when the potential was first proposed, and an average vibrational energy of the HF products of 29.5 kcal/mole (from data of Ref. 20) from classical trajectory calculations. Results of three dimensional classical trajectory calculations on this surface are shown in Table 1. The theoretical studies[17] correctly predict the vibrational population inversion of the HF products. The experimentally observed trend toward increasing population in HF V = 1 relative to HF V = 2 as the temperature is increased also appears in the calculations. The classical trajectory studies show a monotonic decrease in the fraction of available energy appearing as vibration in the products as reactant rotation is increased, whereas experiments tend to show that the vibrational excitation of HF has a minimum for H_2 J = 1. Experiments and calculations show roughly the same fraction of available energy in

product rotation, although the conditions of the experiments are not exactly those used in the calculations.

Similar classical trajectory studies have been done on other potential energy surfaces.[21-25] The main feature of the reaction, product vibrational population inversion, is adequately described in all of these calculations. The major differences among the results on different potential surfaces are the reaction rate constants, which are not in agreement with the experimental value for any surface, and the threshold for the reaction, which cannot be directly compared to currently available experimental data. The semiempirical potential energy surfaces used for the trajectory studies described can be compared to some ab initio quantum mechanical calculations of the $F + H_2$ surface. These calculations showed that the collinear configuration is the minimum energy path for the reaction, with the barrier for the perpendicular approach being 12 kcal/mole higher.[26] Quantum mechanical calculations along the minimum energy path gave a barrier of 1.66 kcal/mole and an exothermicity of 34.4 kcal/mole.[27] The qualitative features agree well with the most widely used semiempirical surfaces. More recent calculations gave an exothermicity of 31.3 kcal/mole, agreeing well with experiment, and a barrier of 3.35 ± 1.0 kcal/mole for the collinear reaction.[28] The barrier is significantly higher than that which gives classical trajectory results most nearly in agreement with experiment.

Quantum mechanical calculations of reaction probabilities for $F + H_2$ have indicated that there are features of the reaction that are not adequately described by classical dynamics. Calculations for

the collinear F + H_2 configuration on the M5 potential surface with ground state reactants show a sharp peak in reaction probability for the production of HF V = 2 at a relative collision energy of about 0.014 eV.[29] The HF V = 3 product first appears at a collision energy of about 0.045 eV, 0.032 eV higher than the point at which it becomes energetically accessible. The fraction of available energy in product vibration when averaged over the relative energy range from 0.0 to 0.4 eV is nearly the same for the quantum mechanical (0.79) and collinear classical trajectory (0.81) calculations, but as a function of energy the value varies between 0.66 and 0.89 in the quantum mechanical results and is nearly constant classically. The very rapid change in the reaction probability as a function of energy for the HF V = 2 product is attributed to dynamic resonance effects. This resonance structure results from interference between direct reaction processes and those having longer lived intermediate states. There are no wells in the collinear potential along the reaction path, so the potential supporting the resonance must be along a different coordinate, corresponding to internal excitation of the collision complex. Vibrationally adiabatic curves for the M5 potential surface have wells for excited vibrational states due to a decrease in the force constant in the collision region which lowers the energy of a given state.[30] If the potential surface is changed to remove these wells the resonance structure in the quantum dynamics calculations disappears, but in this case it is not possible to associate the resonance with the well for one particular vibrational level. The adiabatic potentials depend on the choice of coordinates used to define the vibrational energy, so

this also causes some confusion in attempting to find a physical explanation of the resonances. Very recently a classical method for unambiguously determining the position and energy of vibrationally adiabatic barriers and wells on a collinear potential surface has been described.[31] Application of this technique to the $F + H_2$ reaction on the M5 surface identified barriers in the reactant and product regions for a given classical vibrational action. Quantizing the action according to $F = (n + 1/2)h$ (n an integer) then determines the barriers for particular vibrational states. Appropriately quantized periodic orbits between the barriers were then found and the energies of these trajectories matched almost exactly the energies of the quantum mechanically calculated resonances.[32] It thus seems that these barriers play a crucial role in determining the resonance energies.

Collinear quantum mechanical calculations have been done with several other model $F + H_2$ potential surfaces,[33] including one based on the ab initio surface.[34] Resonance structure is observed in all of the results, but there is little similarity among them. Thus it appears that the quantum mechanical behavior is very sensitive to the potential surface.

For comparison to experimental results three dimensional calculations are necessary. These calculations have been performed for $F + H_2$ ($V = 0$, $J = 0$) on the M5 potential using a J_Z - conserving approximation.[35] They show the effects of quantum mechanical resonances in three dimensions. There are no longer sharp peaks in reaction probabilities as a function of energy as appear in the collinear results. Instead, there is a peak in the reaction probability as a function of

total angular momentum for the HF V = 2 product which shifts to higher angular momentum as the energy is increased. In contrast, the reaction probability for HF V = 3 remains peaked at J = 0 throughout the collision energy range from 0.06 to 0.33 eV. The angular momentum for the reaction is supplied entirely by the orbital angular momentum of the collision, determined by the impact parameter. Since the product scattering angle is related to the impact parameter, the large change in the reaction probability versus angular momentum is expected to produce a corresponding change in the HF V = 2 product angular distribution as the collision energy is varied. A more detailed discussion of this effect is given in conjunction with the analysis of the results of the experimental work to be described here. Probability densities and fluxes have been calculated from the three dimensional wavefunction.[36] The resonance is characterized by buildup of density in the transition state region after the entrance barrier. This is analogous to the collinear case,[30] and supports the idea that the resonance is due to the existence of a quasibound transition state. It is also interesting to note that the energy of the resonance in the collinear calculation agrees well with that in three dimensions if the zero point energy of the transition state and the centrifugal energy from the orbital angular momentum of the collision are added to it.[36]

There is an additional complication in the F + H_2 reaction, the effect of which is not yet well understood. The ^2P fluorine atom can interact with H_2 to give three different doubly degenerate FH_2 electronic states. For a collinear geometry these are a $^2\Sigma$ state corresponding to the singly occupied fluorine P orbital lying along the axis

of the collision complex, and two $^2\pi$ states with the singly occupied P orbitals perpendicular to the collision axis. In the more general case the complex has C_s symmetry and the $^2\Sigma$ state becomes $1^2A'$ while the $^2\pi$ states are $^2A''$ and $2^2A'$.[37] Only the $1^2A'$ state correlates to the $^1\Sigma$ ground state of the HF product. The other states correlate to $^3\pi$ states of HF, which are inaccessible for the collision energies being considered here. In the reactants the $^2A'$ and the $2^2A'$ are separated by the spin-orbit splitting in fluorine, 1.16 kcal/mole.[38] In the experimental studies of the F + H_2 reaction unknown mixtures of ground state F $^2P_{3/2}$ and the spin-orbit excited F $^2P_{1/2}$ were produced. If the $^2P_{1/2}$ state can react by making a transition to the ground electronic state, then the observed results are the sum of two reactions with possibly different dynamics. Comparison with calculations on a single potential energy surface may lead to unreliable conclusions. Calculations show small reaction probabilities for the $^2P_{1/2}$ state of fluorine at low collision energies.[39,40] The potential surfaces for the $^2A''$ and 2 $^2A'$ states are found to be highly repulsive for small F - H_2 separations.[40,41,42] Using semiclassical approximations for the electronic transition probabilities, and classical trajectories for the nuclear motion, calculations give a cross section for F $^2P_{1/2}$ reaction with H_2 that is between 5 and 20% of that for the ground state reaction for collision energies up to 5 kcal/mole.[39,40] The cross section rises quickly with increasing collision energy. The presence of the low lying excited states may also effect the reaction if it is initiated in the ground state. Collinear quantum mechanical calculations

using Muckerman 5 as the ground state potential surface and another model for the spin-orbit excited state had much different results for the energy dependence of the reaction probability than single surface calculations.[43] State to state reaction probabilities had additional structure when two surfaces were considered. All of these calculations depend on the forms of the potential surfaces involved, which are not well known. Therefore it is not possible to say in any detail what effects can be expected from the multiple potential energy surfaces, or how mixtures of F $^2P_{1/2}$ and F $^2P_{3/2}$ influence the interpretation of experimental results.

EXPERIMENTAL

In order to determine the importance of dynamical resonance effects and to judge the accuracy of currently used potential energy surfaces it is necessary to obtain more detailed experimental results on the $F + H_2$ reaction. Differential cross sections for individual HF vibrational states produced in the reaction at well defined collision energies would be particularly valuable for comparison with calculations. Using crossed beams of the reactants and a sensitive mass spectrometer detector angular and velocity distributions of the HF product have been measured. The resulting center-of-mass distributions give, with some limitations, differential cross sections for the various HF product states.

The arrangement of the molecular beam machine used in this work is shown in Fig. 1. A beam of fluorine atoms crosses an H_2 beam at 90° in a chamber evacuated to about 1×10^{-7} torr. The chamber is lined with a copper shield cooled with liquid nitrogen to rapidly pump condensable gases. Reaction products are detected by a mass spectrometer which can be rotated around the collision center. Product time-of-flight was measured by spinning a slotted disk in front of the detector and recording the time needed for products to go from the disk to the detector.

The detector has three nested regions suspended from a lid which rotates on a bearing mounted in the main vacuum chamber. Each detector region is individually pumped by an ion pump. Small slits connect the regions and allow product molecules to reach the innermost one, while providing differential pumping of background gas. The slits determine

the viewing area around the collision center and the angular resolution. In the experiments described a square area 3mm on a side at the collision center was viewed by the detector. The angular acceptance was 1°. The third detector region is liquid nitrogen cooled and has an electron impact ionizer mounted in it. Product molecules passing through all the slits enter the ionizer. Ions formed are mass selected by a quadrupole mass filter. After leaving the quadrupole the ions are accelerated to a target at about -30 kV. Electrons are ejected from the target towards a plastic scintillator and the light flashes from the scintillator are detected by a photomultiplier tube. The resulting pulses go to various kinds of counting electronics.

To measure total product intensity as a function of angle the fluorine beam is modulated at 150 Hz with a tuning fork chopper. A dual channel counter that is synchronously gated in phase with the chopper counts signal pulses with the beam on and off. Choosing a particular angle as a reference and checking the signal periodically ensures that the intensity is stable over the course of the several hours needed to obtain an entire laboratory angular distribution.

Time-of-flight measurements were used to determine product velocity distributions. In the simplest arrangement for doing this a wheel with a small number (usually 4 or 8) of slots was rotated in front of the detector entrance. A small light bulb and a photodiode on opposite sides of the wheel indicate when a slit goes by. This triggers a 255 channel scaler which counts signal pulses for a predetermined time in each channel. The signal can be accumulated for many triggers and transferred to a laboratory computer. The distribution of counts

among the scaler channels is then the distribution of product arrival times after traveling the distance (29.8 cm) from the wheel to the ionizer. A mass dependent correction due to the ion flight time must be made for accurate results. The ion flight time is determined by looking at the arrival times of ions with different mass from fragmentation of a parent neutral in the ionizer. For the conditions of this experiment the ions' flight time was found to be given by

$$T_{ion} = 3\sqrt{M}\ \mu sec$$

where M is the mass to charge ratio of the ion. Thus for HF^+ the value is 13.4 μsec. The time-of-flight wheel can be rotated at frequencies up to about 500 Hz. To spin the wheel a two phase audio oscillator with outputs 90° apart drives two amplifiers with independently adjustable gain. These two outputs run a hysteresis synchronous motor[44] which turns at the driving frequency. The motor is water cooled and rests in a spring loaded mount to maximize the bearing lifetimes at high speeds.

For the $F + H_2$ reaction this simple time-of-flight scheme was unsatisfactory. The low signal level and relatively high background at the mass detected made counting times unreasonably long. Therefore a cross correlation technique was used to increase the duty cycle and shorten counting times. The technique has been described in detail in several places.[45,46,47] It relies on the existence of sequences with the properties that the autocorrelation function is constant except for one point

$$A(x) = \sum_{i=0}^{N-1} S(i)\, S(i+x) = \begin{cases} N, & x = 0 \\ -1, & x \neq 0 \end{cases}$$

and

$$\sum_{i=0}^{N-1} S(i) = 1 \ .$$

Here N is the sequence length, and the sequence elements s are equal to ± 1. If a sequence of this type is cut into the time-of-flight wheel the products are modulated with the same period as the wheel rotation. If the counting time of one channel of the scalar is equal to the wheel period divided by the sequence length the observed intensity after one wheel revolution is

$$I(i) = \sum_{t=0}^{N-1} (S'(i-t) \quad F(t)) + B/N.$$

F is the actual time-of-flight distribution of the detected particles per open element of the wheel, B/N is the background per channel, and S' is now a sequence of ones and zeroes corresponding to whether the particles were transmitted or stopped by the wheel. Cross correlating the intensity with the original sequence and using the fact that $S'(i) = \frac{1}{2}(S(i) + 1)$ gives

$$C(t') = \sum_{i=0}^{N-1} S(i-t') \ I(i)$$

$$= \sum_{i=0}^{N-1} S(i-t') \left[\sum_{t=0}^{N-1} \left(\frac{1}{2} (S(i-t) + 1) \quad F(t) \right) + B/N \right]$$

$$= \sum_{i=0}^{N-1} \left[\sum_{t=0}^{N-1} \left(\frac{1}{2} S(i-t') \ (S(i-t) + 1) \quad F(t) \right) + S(i-t')B/N \right]$$

$$= \frac{1}{2} (N+1) \ F(t') + \sum_{i=0}^{N-1} S(i-t')B/N$$

$$= \frac{1}{2}(N+1)\,F(t') + B/N$$

The result is that the signal is multiplied by the factor (N+1)/2 due to increased transmission of the sequence of slits versus a single slit, while the background is unchanged. In spite of the large increase in the signal obtained, the cross correlation technique is not always preferable to single shot time-of-flight. After cross correlation the signal at each time is the result of either adding or subtracting the observed counts in all channels. Thus the statistical uncertainty for any time is due to the uncertainty in the total number of counts rather than in the counts in a single channel. In the case where the background is much higher than the signal, the cross correlation method is superior to single shot time-of-flight, and in this experiment it would not have been possible to obtain time-of-flight distributions without it.

A modification of the motor driving system described was necessary for the reliable use of the cross correlation time-of-flight method. The advance of channels in the multichannel scalar must be accurately synchronized with the rotation of the wheel. To do this the oscillator defining the rotation frequency was phase-locked to a signal derived by dividing the channel advance clock frequency by the sequence length (255).

The molecular (atomic) beams used in this experiment were produced by supersonic expansion to provide the narrow velocity distributions necessary for good energy resolution. Each consists of a nozzle, from which the gas exhausts into a chamber which is pumped to a pressure of

about 2×10^{-4} torr by an oil diffusion pump. A conical skimmer is mounted facing the nozzle. The skimmer has a small hole to extract a narrow beam from the center of the gas coming from the nozzle. This beam enters a differential pumping region where it is further collimated before entering the main interaction chamber.

Producing a stable, high intensity source of fluorine atoms with a narrow velocity distribution proved to be the biggest problem in studying the $F + H_2$ reaction. The source used produced fluorine atoms by thermal dissociation of a small percentage of F_2 in a carrier gas. It consisted of a nickel tube with a cap welded on one end and a concentric sleeve welded to the cap. A hole in the cap approximately 0.1mm in diameter served as the nozzle orifice. This assembly was heated by coaxial heater cable[48] in three places, two on the inner tube and one right at the end. The oven was supported at the end of the outer sleeve and the end of the inner tube by water cooled copper blocks. The three individually controlled heaters were found necessary to solve several problems in earlier designs. The nickel tube forms a fluoride layer that protects it from further attack, but at the operating temperature of around 700°C the vapor pressure of the nickel fluoride coating is significant. Thus the nozzle had a strong tendency to clog if it was not the hottest point. If the tip alone was heated, then when fluorine was seeded in a gas such as krypton with a low thermal conductivity the mixture would not get hot enough to efficiently dissociate the F_2. The nozzle lifetime was quite sensitive to temperature and heating it much above 700°C would cause the hole to enlarge rapidly. With three heaters it was possible to

adjust the temperatures at various parts of the oven to minimize clogging, and still get dissociation without destroying the tip. The relative concentrations of F $^2P_{3/2}$ and $^2P_{1/2}$ in the beam were not measured. Calculating statistical populations from the energy splitting of 1.16 kcal/mole and the degeneracies of the states gives 20% F $^2P_{1/2}$ at the 700°C oven temperature. This should be an upper limit, as some electronic relaxation may occur in the supersonic expansion.

The molecular hydrogen beam was obtained from high pressure (25 - 70 atm) expansion of H_2. The nozzle was simply a 30 μm aperture in a small platinum disk brazed to the end of a stainless steel tube. The tube was mounted so that the nozzle skimmer distance could be changed from outside the vacuum to optimize the beam intensity. A long (1.92 cm) electroformed nickel skimmer[48] was used to minimize disturbance of the beam. The nozzle temperature could be regulated between 25°C and 450°C. The H_2 velocity distributions were very narrow, the full width at half maximum was only 1-2% of the peak velocity. Although the translational cooling in the supersonic expansion was very effective, rotational relaxation was not complete. Rotational level populations can be estimated from the energy relations for the adiabatic expansion producing the beam. For a diatomic gas at a temperature at which vibration is not excited the total energy available per molecule is 7/2 kT, kT of which is accounted for by rotation. From the source at 28°C the measured H_2 velocity was 2.72×10^5 cm/sec, so the translational energy per molecule was

$$E = 1/2\ mV^2 = 1.77 \text{ kcal/mole.}$$

At 28°C, 7/2 kT = 2.09 kcal/mole. Since the translational temperature in the beam is very low, the difference between 7/2 kT and the energy of a molecule in the beam must be due to H_2 rotation. Thus there is 0.32 kcal/mole of rotational energy remaining after the expansion. This corresponds to a rotational temperature of 160K. To determine the populations of the H_2 levels the ortho and para forms must be properly accounted for. At 300K the ratio of para (even J) to ortho (odd J) hydrogen is determined almost entirely by the nuclear spin degeneracy, with spin 1 molecules having odd rotational levels and zero spin associated with even levels. Since spin 1 has a degeneracy of three, three fourths of the H_2 molecules are in the ortho form at 300K. The two forms do not equilibrate during the short time of the expansion, so the ratio between them is fixed at the room temperature value. Calculated relative populations for the rotational levels are shown in Table 2, assuming a rotational temperature of 160K. To show the effect of heating the H_2 results are also shown for the beam with the nozzle at 276°C. Using the same procedure as above, a terminal rotational temperature of 240K was calculated. These relative populations may not be extremely accurate, because as the gas cools in the expansion they may not follow a normal temperature distribution. The important points are that the dominant rotational state is J = 1, and that on the average about 50% of the initial rotational energy remains after expansion.

DATA ANALYSIS

The experimental apparatus described measures flight times and intensities as a function of angle for molecules moving in the laboratory frame of reference. To compare these results with scattering calculations, data must be converted to intensity in the center-of-mass coordinate system of the colliding particles. The final result is then a map of product flux as a function of center-of-mass angle and velocity or energy. The velocity vector or Newton diagram (Fig. 2) shows the two coordinate systems, and conveniently relates angles and velocities in them. The vertical and horizontal velocity vectors correspond to the fluorine and hydrogen beams respectively. Their base is the origin of the laboratory coordinate system. The center-of-mass moves through the lab as shown by the vector labeled C.M. The tip of this vector is the origin of the center-of-mass system, and F and H_2 velocities are labeled. Circles are drawn at constant center-of-mass speeds corresponding to the maximum energies available for various HF product vibrational states. The usual rules of vector addition can be used to determine the relation between lab and center-of-mass angles. The fluorine atom direction is chosen as zero degrees in both systems.

For a single Newton diagram the intensity in one frame can be directly transformed into the other. Unfortunately the laboratory data to be presented here result from a distribution of Newton diagrams, due to beam velocity and angular spreads, and are also influenced by the resolution of the apparatus. Because of this it is not possible to associate scattered intensity with a particular center-of-mass angle and velocity, making a direct laboratory to center-of-mass transforma-

tion very difficult. The reverse procedure was actually used, because it is easier to model the effects of the experimental conditions on a given center-of-mass intensity distribution. The big drawback is that this distribution must then be guessed, and many trials are needed to find the correct one.

The assumed center-of-mass product flux distribution is specified individually for each product vibrational state. Each state has a maximum translational energy available to it determined by

$$\Delta E + E_{coll.} - E_{vib} = T_{max}$$

as shown on the energy level diagram (Fig. 3). ΔE is the reaction exoergicity, $E_{coll.}$ is the collision energy, E_{vib} is the vibrational energy of the HF product relative to HF (V = 0), and T_{max} is the maximum translational energy. Probability distributions for product translational energy of the form

$$P(E) = E^{\alpha} (T_{max} - E)^{\beta}$$

were used. For convenience in choosing the parameters the distributions were actually characterized by β and E_p, with E_p being the energy at which the probability peaks. The value of α can be calculated from

$$\alpha = \frac{\beta E_p}{T_{max} - E_p} .$$

To obtain a complete center-of-mass flux distribution the parameter β was specified for each vibrational state, and a value of E_p was assigned along with a relative intensity every 5° center-of-mass angle for each state. Values for other angles were found by interpolation. This center-of-mass energy and angular distribution can be transformed to the lab frame for a single Newton diagram. Center-of-mass velocity

is calculated from the energy, then vector relationships provide the angular and velocity transformations to laboratory coordinates. The ratio of volume elements in the two frames determines the intensity transformation. For the center-of-mass energy distribution $I_{c.m.}(E_{c.m.}\theta_{c.m.})\, dE_{c.m.}\, d\Omega_{c.m.}$ the corresponding velocity distribution is

$$I_{c.m.}\ (U,\ \phi_{c.m.}) \propto UI_{c.m.}\ (E_{c.m.}\ \theta_{c.m.})$$

where U is center-of-mass velocity, θ is the scattering angle, and Ω is the solid angle. The lab frame intensity $I_{Lab}\ (V,\theta_{Lab})\ dVd\Omega_{Lab}$ is then found from

$$I_{Lab}(V,\theta_{Lab}) = \frac{V^2}{U^2}\ I_{c.m.}(U,\theta_{c.m.})\ .$$

V is the laboratory velocity. This relation has been derived previously by several people.[50,51] A further transformation allows calculation of the time-of-flight distribution.

$$N(t,\theta_{Lab}) = \frac{V}{T}\ I_{Lab}\ (V,\theta_{Lab})$$

Here N is a number density distribution. The conversion from velocity to time, $t = l/V$, with l being the flight path, has been made, along with a change from flux to number density. This is necessary since the number of ions produced in the electron impact ionizer per unit time is proportional to the number density in the ionizer.

Once the center-of-mass intensity distribution is specified the transformations described can be performed for any initial velocities of the reactants. A computer program written primarily by Dr. Kosuke Shobatake was used to calculate the laboratory intensity for different

Newton diagrams. These intensities were weighted according to the probability for the specific combination of beam speeds and fluorine beam angle, then summed to give simulated laboratory distributions. Additional averaging accounted for the effects of the detector angular resolution and the uncertainty in the flight path due to the ionizer length. A laboratory angular distribution was calculated and scaled to best fit the experimental one. Time-of-flight distributions were calculated at each angle and their area was normalized to the value of the angular distribution. The calculated and experimental results were compared, and the input center-of-mass distribution was changed until satisfactory agreement with the laboratory distributions was obtained.

RESULTS

The results of crossed beam reactive scattering measurements on the F + H_2 reaction are presented here. Experiments were done with the velocities of the fluorine atom and hydrogen beams adjusted to give center-of-mass collision energies of about 2 and 3 kcal/mole. Two complete sets of time-of-flight and laboratory angular distribution data will be shown for collision energies around 3 kcal/mole. The fluorine atom velocities are quite different for the two data sets, and the H_2 velocity was changed to give about the same collision energy in both cases.

A. RESULTS FOR 2 kcal/mole COLLISION ENERGY

The fluorine atom beam was produced by flowing 2 to 3% F_2 seeded in N_2 at a total pressure of 675 torr through the nickel nozzle described before. The temperature of the tip of the source as measured by a chromel-alumel thermocouple was 710°C. The velocity distribution of the component of the beam appearing at mass 19 in the mass spectrometer was determined from time-of-flight measurements. The velocity distribution was assumed to be of the form

$$P(V)dV \quad V^2 e^{-\beta(V-V_F)^2} dV$$ (see Ref. 52, and references therein). For this beam the values of the parameters were $\beta = 1.97 \times 10^{-9}$ sec^2/cm^2 and $V_F = 1.35 \times 10^5$ cm/sec. The distribution had a full width at half maximum of about 25%. The H_2 beam was produced from the expansion of hydrogen at a pressure of 27 atm and a temperature of 29°C through a 30μm aperture. The resulting beam had a velocity distribution with a full width at half maximum less than 3% (the limit imposed by the resolution of the apparatus) and a peak velocity of 2.73×10^5 cm/sec. A Newton diagram is shown in Fig. 2 for the most probable beam velocities. Figure 4 shows the distribution of collision energies due to the angular and velocity distributions of the beams. The actual data obtained with these conditions consist of the laboratory angular distribution Fig. 5, and the set of time-of-flight data at various lab angles, Figs. 6-15. Reliable data could not be obtained closer than 10° from the fluorine beam because of a large increase in background at mass 20. This is due to HF and other contaminants in the beam. For time-of-flight spectra taken closer than 20°

from the fluorine beam the background was not perfectly flat, and was fit with a polynomial before subtraction. This background component from the fluorine beam source should not effect the angular distribution since the H_2 beam was modulated. This minor constituent of the beam detected at mass 20 (HF produced by reactions of fluorine in the nozzle) could contribute to the angular distribution due to elastic scattering by H_2. To find out if this was important, a 0.5% mixture of HF in N_2 was flowed through the nickel nozzle, which was heated to the same temperature as used for reactive scattering. Elastically scattered HF was then detected with the H_2 beam conditions identical to those when the $F + H_2$ reaction product was measured. The intensity of the HF beam was compared to the mass 20 signal from the fluorine beam by obtaining time-of-flight distributions of both beams. This allows scaling of the HF elastic scattering angular distribution to the conditions in the reactive scattering experiment. After doing this it was found that elastic scattering contributed no more than 5% to the reactive signal at angles greater than 10° from the fluorine beam. No attempt was made to correct for this, but the HF content of the fluorine beam was minimized by placing a liquid nitrogen cooled trap between the tank containing the $F_2 - N_2$ mixture and the nozzle.

The laboratory angular distribution shown is the average of several scans, with a total of about 500 seconds of counting time at each angle. The error bars are one standard deviation of the mean calculated from all the scans at each angle. This error was invariably somewhat

larger than that calculated solely from the statistical error associated with the total number of counts.

The time-of-flight spectra are the result of about 90 minutes of counting at each angle, using the cross correlation method described. The wheel used had a sequence length of 255, and spinning it at 392 Hz gave a time channel length of 10 μsec. Peaks due to individual product vibrational states are resolved at several angles.

A center-of-mass product velocity flux contour map derived from these data is shown in Fig. 16. The fitting procedure used to obtain the center-of-mass distribution has already been described. The solid lines in Figs. 5-15, are the calculated laboratory angular and time-of-flight distributions. Contributions from the individual vibrational states are also shown. In the time-of-flight fits an ion drift time of 13.4 μsec, and an offset of 5 μsec due to the placement of the photodiode assembly used to trigger the multichannel scalar have been added to compare directly with the experimental data. The contour map is shown positioned on a portion of the laboratory Newton diagram with 14° laboratory angle indicated. Although the entire distribution is shown, the data from this experiment do not provide information on that part which falls inside of 14°.

The method used to do the laboratory to center-of-mass conversion automatically yields angular distributions for each vibrational state, since these distributions are the input used to calculate trial fits to the laboratory data. In Fig. 17 the total flux per unit solid angle (the differential cross section) is plotted as a function of center-of-mass angle (zero degrees is defined as the direction of an

unscattered F atom) for each vibrational state that is observed. Contributions of HF V = 0 were neglected because very little of it is produced in the reaction, and it could not be resolved from HF V = 1. The quantity displayed in Fig. 17 should be contrasted with that in the contour map, which is product flux per unit solid angle, per unit velocity.

The actual parameters used to calculate fits to the data are presented in the Appendix. The maximum translational energy for each state is calculated using the reaction exothermicity. This is obtained from the dissociation energies of H_2, 103.265 kcal/mole[53] and HF, 135.3 ± 0.17 kcal/mole,[54] giving 32.0 ± 0.17 kcal/mole. This value of the exothermicity assumes ground state reactants and products. In the experiment there is some residual rotational energy of H_2, the rotational temperature is on the order of 160K. The average energy in rotation is then about 0.3 kcal/mole. Since it is not known how this reactant energy appears in the products there is no clear way to determine the correction to the exothermicity needed to account for it. This is not a problem for the HF V = 1 and V = 2 states, but for V = 3 there is only 1.5 kcal/mole available for translation, and the exothermicity must be known accurately to determine the maximum product velocity. The best fit to the data was obtained using an exothermicity of 32.5 kcal/mole, which seems reasonable considering the rotational energy in the H_2 beam. The value chosen for the exothermicity has some effect on the partitioning of intensity between V = 3 and V = 2 at angles where they are not resolved, so a value was chosen which allowed a good fit to be obtained to the time-of-flight data at angles where the V = 3 and V = 2 peaks are well separated.

B. RESULTS FOR 3 kcal/mole COLLISION ENERGY

The first set of data to be presented in this section was obtained using fluorine atom source conditions very similar to those in the experiment at 2 kcal/mole collision energy, and a faster H_2 beam to reach the higher collision energy. A mixture of 2.5% fluorine seeded in nitrogen was used at a total pressure of 1100 torr. The nozzle tip was heated to 655°C, since the somewhat lower temperature increased the life expectancy. The parameters for the beam, as defined in the previous section, were $\beta = 1.5 \times 10^{-9}$ sec^2/cm^2 and $V_F = 1.39 \times 10^5$ cm/sec. The hydrogen beam source was heated to accelerate the H_2. At a temperature of 219°C and pressure of 37 atm the velocity of the peak of the H_2 beam was 3.51×10^5 cm/sec, and the width of the distribution was less than the resolution of the time-of-flight system. A Newton diagram for the most probable beam velocities is shown in Fig. 18. The data appear in Figs. 19-30. In this case the time-of-flight wheel was spinning at 490 Hz giving a time channel length of 8 μsec. Counting periods for both the angular and time-of-flight data were similar to those for the data at lower collision energy. Figure 31 is a contour map of the center-of-mass distribution which gave the fit to the data as indicated by the solid lines. A plot of the total flux as a function of center-of-mass angle for each product vibrational state is shown in Fig. 32.

To check the accuracy of these results another complete set of data was taken using different experimental conditions to obtain the same collision energy. A mixture of 3% F_2 in krypton at 650 torr was used with a nozzle temperature of 650°C to produce the F atom beam.

This beam was described with the parameters $V_F = 6.98 \times 10^4$ cm/sec and $\beta = 1.6 \times 10^{-8}$ sec^2/cm^2. Thus the peak velocity is half that of the F in N_2 beams, and the full width at half maximum is about 20% of the peak velocity. The H_2 source was used at 275°C with a pressure of 37 atm. The H_2 velocity was 3.74×10^5 cm/sec. Figure 33 is the Newton diagram for the reaction under these conditions. There are several advantages in using the fluorine seeded in krypton beam. Since the atoms are moving much slower than when seeded in N_2, the laboratory frame velocity of the products is lower. For a given time resolution this yields better velocity resolution. The spread in collision energies is also much smaller as is apparent in Fig. 34, where it is compared with the distribution of collision energies when the fluorine is seeded in N_2. Unfortunately the characteristics of the krypton seeded beam make the reactive scattering signal much smaller. Since the krypton is much heavier than fluorine the fluorine tends to get scattered out of the beam during the expansion, reducing its intensity at the collision center. The lower lab velocities make the ratio of lab to center-of-mass speeds smaller and reduces the fraction of the scattered product intercepted by the detector at any one angle. This is evident from the center-of-mass to lab intensity transformation where $I_{LAB}(V,\theta_{LAB}) \propto \frac{V^2}{U^2} I_{c.m.}(U,\theta_{c.m.})$. A further limitation of using F_2 in Kr is that krypton has isotopes at masses 80 and 82. When these masses are quadruply ionized the mass to charge ratio is at or near 20 so the mass specrometer cannot distinguish them from the HF product.

This prevents meaningful measurements over the range of angles in which elastically scattered krypton can appear, from zero degrees (the direction of the F beam) out to about 20 degrees. In spite of these problems, it was possible to observe the reactive scattering for a wide range of angles. The data are shown in Figs. 35-42. The counting time for each point of the angular distribution was 300 to 500 seconds. The fractional error is 3 to 4 times that for the angular distribution obtained using fluorine seeded in nitrogen. The time-of-flight measurements required extremely long counting times, from 5 to 12 hours at each angle. Even after such long accumulation times the data is fairly noisy. The data were smoothed to give a better indication of how it should be fit, but the points shown in the figures are the actual data. The center-of-mass contour map in Fig. 43 shows some unusual features associated with V = 2 product that are necessary to fit the data. The same structure appears in Fig. 44 when the center-of-mass angular distribution is plotted for each vibrational state. An extensive effort was made to fit the fluorine in nitrogen and fluorine in krypton data at the same collision energy simultaneously with the same center-of-mass distribution. This does not seem to be possible. Reasons for the differences and some similarities will be discussed.

The input parameters used to fit all of the data at 3 kcal/mole are given in the Appendix. The value used for the reaction exothermicity was raised to 33.0 kcal/mole, which reflects the increased population of higher rotational levels of H_2 at the source temperatures needed to reach a collision energy of 3 kcal/mole.

Before any meaningful conclusions about the dynamics of the F + H_2 reaction can be drawn it is important to consider some of the uncertainties involved in the analysis of these data. There are several sources of error in the data, noise due to counting statistics and small fluctuations in beam intensity, the calibration and inherent resolution limits of the time-of-flight system, and possible small contributions from scattering of contaminants in the F atom beam. The effect of these uncertainties in the laboratory data on the center-of-mass distributions can be estimated from the transformation equation

$$I_{LAB}(V,\theta_{LAB}) \propto \frac{V^2}{U^2} I_{cm}(U,\theta_{cm}) .$$

Clearly the laboratory intensity is very sensitive to the ratio of the lab to center-of-mass velocities. This is a serious problem for interpreting the F in N_2 + H_2 data. From the Newton diagram (Fig. 2) it can be seen that the ratio of the maximum center-of-mass velocity of the V = 3 product to its laboratory velocity is about 1 to 6. An error of 1% in the laboratory velocity causes an error of 12% in the center-of-mass intensity. The peaks in the time-of-flight spectra ap- pear at about channel 30, so the velocity increment corresponding to one time channel is 3 to 4%. The inherent velocity resolution thus severely limits the accuracy of the determination of center-of-mass intensity, at least for V = 3 product. At angles where the individual vibrational states are not resolved, the velocities of states contributing to the time-of-flight spectrum must be extrapolated from angles where the states are resolved. This introduces further uncertainty beyond the limits due to apparatus resolution. The velocity spread of

the fluorine beam causes reaction products scattering with a range of Newton diagrams to contribute to the observed signal. The F in N_2 beam has a full width at half maximum velocity spread comparable to the diameter of the V = 3 product circle. Although the beam is carefully modelled in the data fitting procedure, it is not possible to accurately recover features of the center-of-mass distribution which change on a velocity scale small compared to the beam spread. When all of the limitations on deriving the center-of-mass distribution from the lab data are taken into account, it is clear that the data obtained using the F in N_2 beam may not be sufficient to give a reliable description of the V = 3 product distribution. It would also be desirable to resolve the V = 3 and V = 2 products in the time-of-flight distributions at more angles. This was the motivation for doing the experiment with the F in Kr beam. The Newton diagram in Fig. 33 shows that the lab velocity is only about 3.7 times the center-of-mass velocity for the fastest V = 3 products. A fractional error in the lab velocity causes a smaller error in the center-of-mass velocity than when the F in N_2 beam is used. This, in addition to the fact that the beam fwhm is only about one fourth of the diameter of the V = 3 product circle, makes the conversion of the data to center-of-mass coordinates potentially much more accurate. A major drawback is, as mentioned before, that the signal level was very low and statistical fluctuations in the time-of-flight data were large.

The main features of the center-of-mass scattering distributions can now be summarized with careful attention to the experimental limitations just discussed, and noting the regions of the contour maps that

are within the range of laboratory angles for which data were obtained (see Figs. 16, 31 and 43). At a collision energy of about 2 kcal/mole the HF product is predominantly backward scattered (180° relative to the fluorine atom direction). The backward peaking is not sharp, a large fraction of the peak intensity remains at a center-of-mass angle of ninety degrees for all vibrational states. The forward scattering could not be observed due to interference from the fluorine beam. The velocity distribution for the V = 2 product is narrower and peaks at higher speed in the backward direction than at the sides. At a collision energy of about 3 kcal/mole the data taken with fluorine seeded in krypton result in a very unusual contour map. The HF V = 2 product distribution as a function of center-of-mass angle has a sharp peak at about 105°. The intensity drops rapidly in the forward direction, while at larger angles a second peak appears at 125°. The exact height of these peaks is poorly determined due to the noise in the data. For comparison, the best fit to the lab angular and time-of-flight data is shown in Figs. 45-52 for isotropic center-of-mass distributions. Clearly the structure in the angular distribution is not well fit with isotropic distributions, but the error bars allow a fairly wide range of peak heights in the HF V = 2 product intensity while adequately simulating the laboratory data. The V = 3 product intensity has a weak backward peak at this collision energy, similar to that at 2 kcal/mole collision energy. Somewhat more of the forward scattering can be observed in this case, and it appears that the V = 3 intensity is increasing as the center-of-mass angle decreases, but krypton elastic scattering prevents measurements at lab angles small enough to de-

termine if the V = 3 product actually has a forward peak. The shape of the V = 1 distribution is similar to that at the lower collision energy. The center-of-mass contour diagram derived from the data taken with F seeded in N_2 at a collision energy of 3 kcal/mole is significantly different from that obtained at nominally the same collision energy with F seeded in krypton. The distributions assigned to the V = 3 and V = 1 products are very similar to the F in Kr results, but the peaks in the intensity of the V = 2 product are less pronounced in the F in N_2 results. Several factors may contribute to causing different V = 2 distributions to be derived from the two data sets. The intensities at the peaks are not very accurately determined by either data set. As mentioned before, the statistical noise in the F in Kr data causes some uncertainty, while for the F in N_2 data the states are not resolved in the time-of-flight, making the transformation to the center-of-mass difficult. The problem is complicated by the slowing and broadening of the V = 2 velocity distribution in the vicinity of the peaks in the center-of-mass angular distribution. This effect is illustrated in Figs. 47 and 48, showing time-of-flight distributions at 26° and 28° from F in Kr. Attempting to fit these angles with isotropic center-of-mass velocity (energy) distributions that fit well at a center-of-mass angle of 25° results in two resolved peaks that do not correspond well to the data.

The preceding discussion assumes that the center-of-mass distributions produced in the F in N_2 and F in Kr + H_2 experiments are the same, and that the differences we observe result from errors in deriving them. Figures 53 and 54 show that this probably cannot explain all

of the difference. Figure 53 shows the F in Kr + H_2 angular distribution, and an attempted fit with the center-of-mass input parameters used to fit the F in N_2 + H_2 data at 3 kcal/mole. Figure 54 is the corresponding attempt to fit the F in N_2 data with the F in Kr center-of-mass distribution. There seem to be systematic differences well outside the uncertainty in the data.

The most likely explanation for this apparent inconsistency is that the product scattering is strongly energy dependent, and the differences are due to the translational energy distributions for the two experiments (see Fig. 34). Further discussion of possible reasons for this energy dependent behavior follows.

DISCUSSION

The purpose of the experiments described was to obtain more specific information about the dynamics of the $F + H_2$ reaction than that provided by the use of other methods. The experimental center-of-mass angular distributions presented are needed to assess the importance of dynamical effects predicted by quantum mechanical calculations but absent in classical results.

Much work has been done using classical trajectories to attempt to understand the $F + H_2$ reaction, and also to evaluate proposed potential surfaces. The most widely used potential surface (known as the Muckerman V or M5 potential) for both classical and quantum studies of the reaction was determined by requiring that a set of classical trajectories reproduce the experimentally determined average product vibrational energy and give what was the best value of the activation energy when this surface was proposed. Classical calculations of the product angular distributions using this surface have predicted the scattering to be strongly backward peaked.[17] This is the expected result since collinear approach of the reactants is strongly favored. Recent classical calculations of the differential cross sections for individual HF product vibrational states yield backward peaked distributions for all states even at the fairly high collision energy of 5.37 kcal/mole.[55] The results are similar for all states, V = 1, 2 and 3, with approximately a 3 to 1 ratio of backward to forward product intensities. Calculations at 3 kcal/mole gave a more sharply peaked differential cross section, but did not distinguish among vibrational states.[17]

The experimental results do not agree with the prediction from classical trajectory studies of strongly backward peaked HF scattering in the energy range studied. The comparison is best made for the V = 2 product distribution since it is most accurately determined in the experiment, it is the only one that shows a strong energy dependence and V = 2 is the most abundant product. At 2 kcal/mole collision energy the V = 2 product distribution peaks at about 140° and is fairly broad. At a collision energy of 3 kcal/mole there is not even qualitative agreement with classical results, the experiments show prominent sideways peaking of the V = 2 product intensity. One explanation for the discrepancy is that the potential surface used for the classical trajectory calculations is simply not accurate enough to give the correct results. It seems that in this case quantum mechanical effects are important enough that even if the exact potential were known classical calculations would not give the correct angular distributions.

Results of recent three dimensional quantum mechanical calculations show changes in the reaction probability as a function of energy for HF V = 2 product that should cause changes in the product angular distribution similar to those observed in these experiments. The sharp peaks in the reaction probability for production of HF V = 2 seen in one dimensional calculations are gone in three dimensions. Instead, there is a change in the shape of the reaction probability for HF V = 2 product as a function of angular momentum as the collision energy is varied. This is shown in Fig. 55. The initial total angular momentum consists entirely of collision orbital angular momentum, since the calculations are for H_2 J = 0. The orbital angular momentum is

directly related to the collision impact parameter. For collisions where rotational excitation of the product is not important, conservation of angular momentum requires the HF product to scatter at smaller center-of-mass angles (away from the backward direction) as the impact parameter, and hence the orbital angular momentum, increases. The effect expected from the results shown in Fig. 55 for HF V = 2 is that as the collision energy increases, the peak product scattering intensity should shift to smaller center-of-mass angles as the collision energy increases. The actual angle of the peak depends on the potential surface for the reaction. A simple classical model of the reaction has been used to calculate the differential cross section from the quantum mechanical reaction probability.[36] At a collision energy of 0.08 eV (1.85 kcal/mole) the model predicts backward peaking of the V = 2 product, while at 0.13 eV (3.0 kcal/mole) the product peaks strongly at a center-of-mass angle of about 120°. This sideways shift of the peak in the differential cross section is similar to that experimentally observed for the V = 2 product. The calculation cannot be expected to agree quantitatively with the experiments because of the simple model used, and the neglect of bent configurations of the reaction intermediate. It should give an indication of the effect of dynamical resonances predicted in one dimensional calculations on the actual three dimensional reaction. The rapid change in the differential cross section as a function of energy may explain the differences between the center-of-mass distributions derived from F in Kr and F in N_2 data at 3 kcal/mole collision energy. As shown in Fig. 34 the collision energy spread in the experiment using F in N_2 is fairly

large compared to the energy range over which the angular distribution is expected to change drastically. This could cause the sharp features observed with F in Kr to be smeared out when F in N_2 was used. Very recent quantum mechanical scattering calculations using the Reactive Infinite Order Sudden Approximation on the M5 surface show similar shifts of HF V = 2 scattered intensity to smaller angles as the energy is raised.[56] Oscillations also appear in the V = 2 differential cross section at energies above 2.14 kcal/mole. Cross sections were calculated with the IOS approximation up to a relative energy of 0.233 eV (5.37 kcal). The results can be directly compared to classical calculations and show the V = 2 differential cross section peaking at 60° and then dropping rapidly in the forward direction, while, as mentioned before, in the classical results the cross sections for all states peak at 180° (backwards).

The results of the experiments described here are consistent with important aspects of the dynamics of the F + H_2 reaction predicted from quantum mechanical calculations on model potential surfaces. Detailed interpretation of these calculations indicates that the energy dependence of the dynamics is strongly influenced by resonance effects. In one dimensional collinear models the resonance energies appear to correspond to the levels of quasibound states resulting from trapping of energy in vibration of the collision complex along coordinates that do not lie on the reaction path. These quasibound states also appear to play a role in the reaction dynamics in three dimensions, but the observable effect is more subtle. At any point during the collision the relative translational energy is partitioned between a radial com-

ponent due to the motion of the particles toward the center-of-mass, and the centrifugal energy, which is determined by the orbital angular momentum and the separation of the particles. If the centrifugal energy is evaluated at the transition state then the peak in the reaction probability (Fig. 55) occurs at a radial energy which corresponds well with the one dimensional resonance energy shifted by the zero point energy of the bending vibration for the collision complex. Thus for any collision energy, within a certain range, the resonance effect can occur for some values of the orbital angular momentum. This leads to the changes in the product angular distribution as a function of collision energy mentioned previously.

To avoid giving the impression that the dynamics of the $F + H_2$ reaction are now well understood it is important to mention some problems which were ignored in the preceeding discussion. No attempt was made to compare the experimentally determined center-of-mass distributions for HF V = 3 and V = 1 products to theoretical results. There are several reasons for this omission. The resolution limitations of the experimental setup cause large uncertainties in the determination of these distributions, so comparison with calculated results might be misleading. Also, the dynamics of the reaction producing these products have received much less theoretical attention because the most interesting effects show up in the V = 2 product channel (at least on the Muckerman V potential). The calculations that have been done indicate that the V = 1 and V = 3 products are expected to be backward peaked over the energy range in which the experiments were performed.[56] All the quantum mechanical calculations to which the experimental re-

sults were compared assumed the reactant H_2 molecule was in rotational state J = 0. The H_2 beam in these experiments contains a distribution of rotational states peaking for J = 1. Possible effects of the initial rotational state on the center-of-mass distributions is not known.

To establish that the interpretation of the results given here is correct requires more information on the accuracy of the approximate quantum mechanical scattering calculations, and also the sensitivity of the calculated results to the potential energy surface. There is evidence that the Muckerman V surface is not entirely correct. Quantum calculations using it do not predict the experimentally observed product branching ratios. The J_Z - conserving and Infinite Order Sudden calculations give different branching ratios, but use potentials that differ for non-collinear collision configurations. Neither reproduces the experimental branching ratios. The calculated integral cross section for the reaction at relative energies above 1.5 kcal/mole is significantly smaller from the quantum mechanical results than from classical calculations,[35] yet the rate constant determined using classical trajectories is about a factor of four smaller than recent experimental values. At present it is not possible to separate the effects of inadequacies in the potential surface from those in the techniques of calculation.

Although neither the experimental nor the calculated results are as conclusive as one would like, it does appear that quantum mechanical dynamic resonance effects play a role in the F + H_2 reaction. The

qualitative agreement between the results, and marked deviation from the behavior predicted classically certainly seem to support this conclusion.

REFERENCES

1. J. H. Parker and G. C. Pimentel, J. Chem. Phys. 51, 91 (1969).
2. R. D. Coombe and G. C. Pimentel, J. Chem. Phys. 59, 251 (1973).
3. M. J. Berry, J. Chem. Phys. 59, 6229 (1973).
4. N. Jonathan, C. M. Melliar-Smith, and D. H. Slater, Mol. Phys. 20, 93 (1971).
5. J. C. Polanyi and K. B. Woodall, J. Chem. Phys. 57, 1574 (1972).
6. D. J. Douglas and J. C. Polanyi, Chem. Phys. 16, 1 (1976).
7. D. S. Perry and J. C. Polanyi, Chem. Phys. 12, 419 (1976).
8. R. D. Coombe and G. C. Pimentel, J. Chem. Phys. 59, 1535 (1973).
9. K. H. Homann, W. C. Solomon, J. Warmatz, H. Gg. Wagner, and C. Zetzsch, Ber. Bunsenges. Physik. Chem., 74, 585 (1970).
10. R. Foon and C. P. Reid, Trans. Faraday Soc., 67, 3513 (1971).
11. V. I. Igoshin, L. U. Kulakov, and A. I. Nikitin, Sov. J. Quant. Electron., 3, 306 (1974).
12. V. P. Bulatov, U. P. Balakhin, and O. M. Sarkisov, Akad. Nauk. SSSR, Div. Chem. Sci., 26, 1600 (1977).
13. E. Wurzberg and P. L. Houston, J. Chem. Phys. 72, 4811 (1980).
14. R. F. Heidner III, J. F. Bott, C. E. Gardner, and J. E. Melzer, J. Chem. Phys. 72, 4815 (1980).
15. S. Sato, J. Chem. Phys. 23, 592 (1955).
16. P. J. Kuntz, E. M. Nemeth, J. C. Polanyi, S. D. Rosner, and C. E. Young, J. Chem. Phys. 44, 1168 (1966).
17. J. T. Muckerman, Theoretical Chemistry: Advances and Perspectives, Vol. 6A, Academic Press, New York (1981) p. 1-77.
18. P. D. Mercer and H. O. Pritchard, J. Phys. Chem. 63, 1468 (1959).

19. G. C. Fettis, J. H. Knox, and A. F. Trotman-Dickenson, Can. J. Chem. 38, 1643 (1960).

20. J. C. Polanyi and D. C. Tardy, J. Chem. Phys. 51, 5717 (1969).

21. J. T. Muckerman, J. Chem. Phys. 56, 2997 (1971).

22. R. L. Jaffe and J. B. Anderson, J. Chem. Phys. 54, 2224 (1971).

23. R. L. Wilkins, J. Chem. Phys. 57, 912 (1972).

24. N. C. Blais and D. G. Truhlar, J. Chem. Phys. 58, 1090 (1973).

25. J. C. Polanyi and J. L. Schreiber, Faraday Disc. Chem. Soc. 62, 267 (1977).

26. C. F. Bender, P. K. Pearson, S. V. O'Neil, and H. F. Schaefer III, J. Chem. Phys. 56, 4626 (1972).

27. C. F. Bender, S. V. O'Neil, P. K. Pearson, and H. F. Schaefer III, Science 176, 1412 (1972).

28. S. R. Ungemach, H. F. Schaefer, and B. Liu, Faraday Disc. Chem. Soc. 62, 330 (1977).

29. G. C. Schatz, J. M. Bowman, and A. Kupperman, J. Chem. Phys. 63, 674 (1975).

30. S. L. Latham, J. F. McNutt, R. E. Wyatt, and M. J. Redmon, J. Chem. Phys. 69, 3746 (1978).

31. E. Pollak, J. Chem. Phys. 74, 5586 (1981).

32. E. Pollak, and M. S. Child, Chem. Phys. 60, 23 (1981).

33. S. F. Wu, B. R. Johnson, and R. D. Levine, Molec. Phys. 25, 839 (1973).

34. J. N. L. Connor, W. Jakubetz, and J. Manz, Molec. Phys. 29, 347 (1975).

35. M. J. Redmon, and R. E. Wyatt, Chem. Phys. Lett. 63, 209 (1979).

36. W. E. Wyatt, J. F. McNutt, and M. J. Redmon, to be published, Ber. Bunsenges. Physik. Chem.

37. D. G. Truhlar, J. Chem. Phys. 56, 3189 (1972).

38. U. S. National Bureau of Standards Circular 467, 60 (1949).

39. J. C. Tully, J. Chem. Phys. 60, 3042 (1974).

40. A. Komornicki, K. Morokuma, and T. F. George, J. Chem. Phys. 67, 5012 (1977).

41. R. L. Jaffe, K. Morokuma, and T. F. George, J. Chem. Phys. 63, 3417 (1975).

42. F. Rebentrost and W. A. Lester, Jr., J. Chem. Phys. 63, 3737 (1975).

43. I. H. Zimmerman, M. Baer, and T. F. George, J. Chem. Phys. 71, 4132 (1979).

44. T. R. W. Globe Motors, 2275 Stanley Ave., Dayton, Ohio 45404.

45. D. L. Price and K. Skold, Nucl. Instrum. Meth. 82, 208 (1970).

46. C. V. Nowikow and R. Grice, J. Phys. E. 12, 515 (1979).

47. G. Comsa, R. David, and B. J. Schumacher, Rev. Sci. Intrum. 52, 789 (1981).

48. Semco Inc., 11505 Vanowen Street, No. Hollywood, CA 91605.

49. Beam Dynamics, Inc., 708 East 56th Street, Minneapolis, Minnesota 55417.

50. T. T. Warnock and R. B. Bernstein, J. Chem. Phys. 49, 1878 (1968).

51. G. L. Catchen, J. Husain, and R. N. Zare, J. Chem. Phys. 69, 1737 (1978).

52. M. Vernon, "Kelvin Rare Gas Time-of-Flight Program," LBL-12422, (1981).

53. W. C. Stwalley, Chem. Phys. Lett. 6, 241 (1970).

54. G. Di Lonardo and A. E. Douglas, Can. J. Phys. 51, 434 (1973).

55. N. C. Blais and D. G. Truhlar, to be published.

56. M. Baer, J. Jellinek, and D. J. Kouri, submitted to J. Chem. Phys.

57. N. Jonathan, C. M. Melliar-Smith, S. Okuda, D. H. Slater, and D. Timlin, Mol. Phys., 22, 561 (1971).

58. R. N. Sileo and T. A. Cool, J. Chem. Phys. 65, 117 (1976).

Table 1. Experimental and Theoretical HF Product Vibrational Distributions for the F + H_2 Reaction.

	Relative Reaction Rates for HF Product Vibrational States V = 1	V = 2	V = 3
Experimental Results			
Chemical Laser			
Ref. 2			
236°K		1.0	0.505 ± 0.01
298°K		1.0	0.478 ± 0.005
364°K		1.0	0.463 ± 0.006
172°K	0.222 ± 0.01	1.0	
432°K	0.345 ± 0.03	1.0	
Ref. 3			
297°K	0.294 ± 0.01	1.0	0.63 ± 0.04
Infrared Chemiluminescence			
Ref. 57[a]			
300°K	0.28 ± 0.02	1.0	0.58 ± 0.12
Ref. 7			
279°K	0.28	1.0	0.55
718°K	0.38		0.55
1315°K	0.44	1.0	0.55
Theoretical Results			
Classical Trajectories on the M5 Surface			
Ref. 17			
200°K	0.18	1.0	0.475
300°K	0.19	1.0	0.42
1000°K	0.26	1.0	0.48

[a]Values corrected in Ref. 3 for more accurate HF transition probabilities in Ref. 58.

Table 2. Estimated Relative H_2 Rotational State Populations in the Molecular Beam

H_2 Rotational State	Nozzle Temperature 301°K	549°K
0	2.83×10^{-1}	2.26×10^{-1}
1	1.00	1.00
2	5.34×10^{-2}	1.27×10^{-1}
3	1.00×10^{-2}	6.11×10^{-2}
4	4.58×10^{-5}	1.39×10^{-3}
5	8.326×10^{-7}	1.37×10^{-4}

FIGURE CAPTIONS

Fig. 1. Schematic diagram of the crossed molecular beams machine.

Fig. 2. Newton diagram for the collision of F and H_2 at a center-of-mass energy of about 2 kcal/mole. Vertical and horizontal vectors show the velocities in the lab frame of F and H_2 respectively. Center-of-mass velocities for the two particles are also indicated. Circles are drawn at the maximum center-of-mass speeds for the various HF product vibrational states observed. The angle of the center-of-mass velocity vector, relative to the F atom velocity, is shown.

Fig. 3. Energy level diagram for the F + H_2 reaction. The dashed line indicates the energy of the reactants. All energies are given in kcal/mole. Vibrational state energies for HF are from Ref. 54.

Fig. 4. Distribution of collision energies for the experiment with F in N_2 and H_2 reacting with a collision energy around 2 kcal/mole.

Fig. 5. Laboratory angular distribution for HF product from the F + H_2 reaction at a collision energy of 2 kcal/mole. The solid dots are the data, with typical error bars shown. The solid line is the best fit to data. The dashed lines labeled 1, 2 and 3 show the contributions of the various HF vibrational states to the best fit. Zero degrees corresponds to the direction of the F atom beam in the lab frame. Intensity is in arbitrary units.

Figs. 6-15. Time-of-flight data for HF product from the F + H_2 reaction at 2 kcal/mole. Crosses are the data points, and the solid line is the best fit. The dashed lines labeled 1, 2 and 3 are the contributions of the HF vibrational states to the fit. N(t) is the product number density as a function of flight time. N is in arbitrary units.

Fig. 16. Center-of-mass velocity flux contour map for the HF product from the F + H_2 reaction at 2 kcal/mole. The contour spacing is 0.05 with the highest point assigned the value of 1.0. Part of the Newton diagram at this energy is included to show the relation between lab and center-of-mass quantities. The line at 14° shows the lower angular limit of the data taken, and the part of the contour map to the left of this line is not really determined by this experiment.

Fig. 17. Center-of-mass angular distribution for HF V = 1, 2 and 3 products from the F + H_2 reaction at a collision energy of 2 kcal/mole. The dashed line gives the approximate limit to the range of angles for which these distributions are determined from the data of this experiment. Products at center-of-mass angles less than 80° could not be observed due to interference from the F atom beam.

Fig. 18. Newton diagram for the F in N_2 + H_2 experiment at a collision energy of 3 kcal/mole. The center-of-mass angle is shown, and the circles give the maximum center-of-mass speed for different HF product vibrational states.

Fig. 19. Laboratory angular distribution for the HF product from the $F + H_2$ reaction at a collision energy of 3 kcal/mole, with F seeded in N_2. The dots are the data, the solid line is the best fit, and contributions of the various HF vibrational states are shown with dashed lines.

Figs. 20-30. Time-of-flight data for F in $N_2 + H_2$ at a collision energy of 3 kcal/mole. The crosses are the data, the solid line the best fit, and the dashed lines the contributions of individual vibrational states. N(t) is the number density as a function of flight time.

Fig. 31. Center-of-mass velocity flux contour map determined from the data for F in $N_2 + H_2$ at 3 kcal/mole. The contour interval is 0.05 with the highest point equal to 1.0. Part of the Newton diagram is shown with the center-of-mass velocity vector. No time of flight data were taken for lab angles smaller than 18°.

Fig. 32. Center-of-mass angular distributions for HF product vibrational states as determined from the data for the $F + H_2$ reaction at 3 kcal/mole collision energy with F seeded in N_2. The dashed line indicates approximately the smallest center-of-mass angle for which laboratory data were obtained.

Fig. 33. Newton diagram for most probable F and H_2 velocities with F seeded in Kr, and a center-of-mass collision energy of 3 kcal/mole. The center-of-mass velocity is at an angle of 29° to the laboratory F atom velocity. Maximum center-of-mass HF product speeds are given by the labeled circles.

Fig. 34. Comparison of the distribution of collision energies for the reactive scattering of F seeded in Kr with H_2 and F seeded in N_2 with H_2 at collision energies around 3 kcal/mole.

Fig. 35. Laboratory angular distribution for the HF product from the reaction of F in Kr with H_2 at a collision energy of about 3 kcal/mole. The dots are the data with some typical error bars shown. The solid line is the best fit, and the dashed lines are contributions of individual vibrational states to the fit.

Fig. 36–42. Time-of-flight data for HF product fom F in Kr + H_2 at around 3 kcal/mole collision energy. The crosses are the data, the solid line the best fit, and the labeled dashed lines the contributions of various HF vibrational states to the best fit.

Fig. 43. Center-of-mass velocity flux contour map for the HF product from the reaction of F in Kr + H_2 at around 3 kcal/mole collision energy. The contour interval is 0.05 and the highest point is set to 1.0. The smallest lab angle for which time-of-flight data were obtained is 22° due to elastic scattering of Kr.

Fig. 44. Center-of-mass angular distribution of HF product vibration states from the reaction of F in Kr + H_2 at 3 kcal/mole collision energy. The dashed line is approximately the smallest center-of-mass angle that could be observed.

Fig. 45. Laboratory angular distribution for HF product from the reaction of F in Kr + H_2 at a collision energy of about 3 kcal/mole. The dots are the data. The solid line is the best fit to the angular distribution that was obtained by constraining the center-of-mass angular distribution of each HF vibrational state to be isotropic.

Figs. 46-52. Time-of-flight data for the HF product from the reaction of F in Kr + H_2 at 3 kcal/mole. The crosses are the data. The solid line is the fit obtained using isotropic center-of-mass angular distributions for the HF vibrational states. The laboratory angular distribution in Fig. 45 was fit simultaneously.

Fig. 53. Laboratory angular distribution for HF products from the F in Kr + H_2 reaction at 3 kcal/mole. The points are the data. The solid line was obtained using the best fit center-of-mass product distribution for the F in N_2 + H_2 data at 3 kcal/mole collision energy. This distribution was used with the beam parameters appropriate for the F in Kr + H_2 data. Contributions of individual HF vibrational states to this fit are also shown.

Fig. 54. Laboratory angular distribution of HF product from the reaction of F in N_2 with H_2 at about 3 kcal/mole. The dots are the data. The solid line results from using the center-of-mass product distribution obtained from the F in Kr + H_2 data with beam parameters from the F in N_2 + H_2 experiment. Contributions of individual HF vibrational states are shown by the dashed lines.

Fig. 55. a) Plot of reaction probability for F + H_2(V = 0) → HF(V = 2) + H as a function of total angular momentum J and total energy (includes H_2 zero point energy). From Refs. 35 and 36.

b) Plot of reaction probability for F + H_2(V = 0) → HF(V = 3) + H as a function of total angular momentum and total energy. From Ref. 35 and 36.

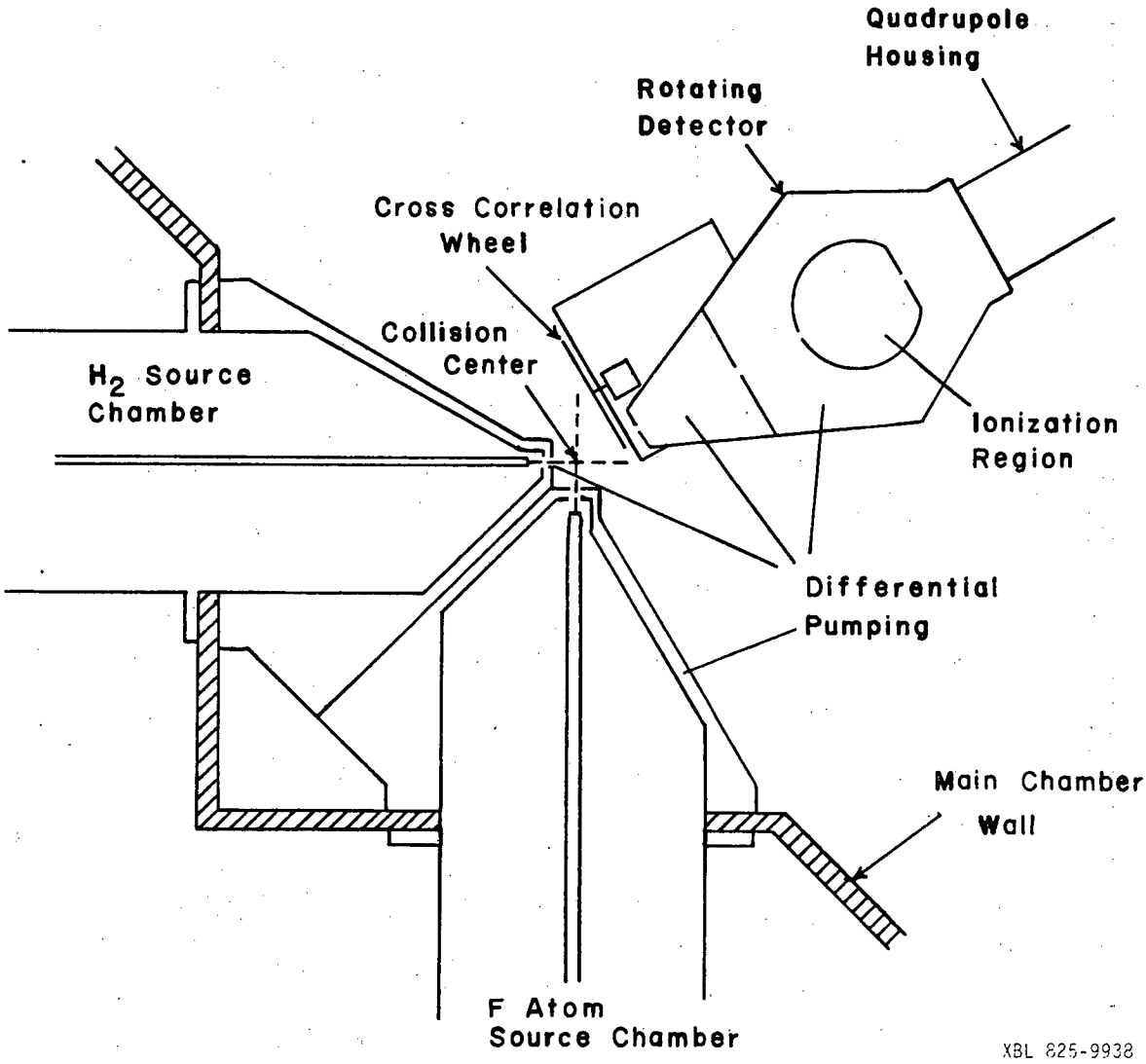
Quadrupole
Housing
Rotating
Detector
Cross Correlation
Wheel
Collision
Center
H_2 Source
Chamber
Ionization
Region
Differential
Pumping
Main Chamber
Wall
F Atom
Source Chamber
XBL 825-9938

Fig. 1.

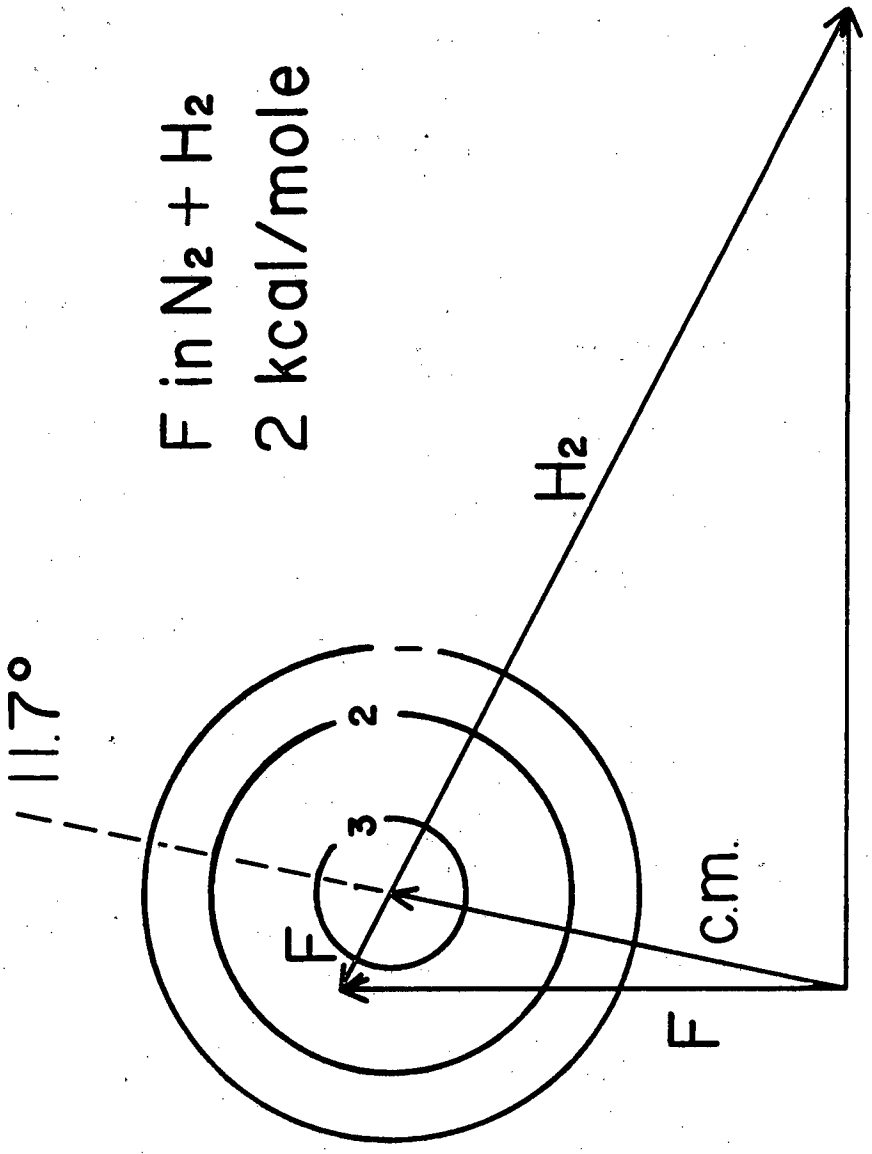

XBL 825-9939

Fig. 2.

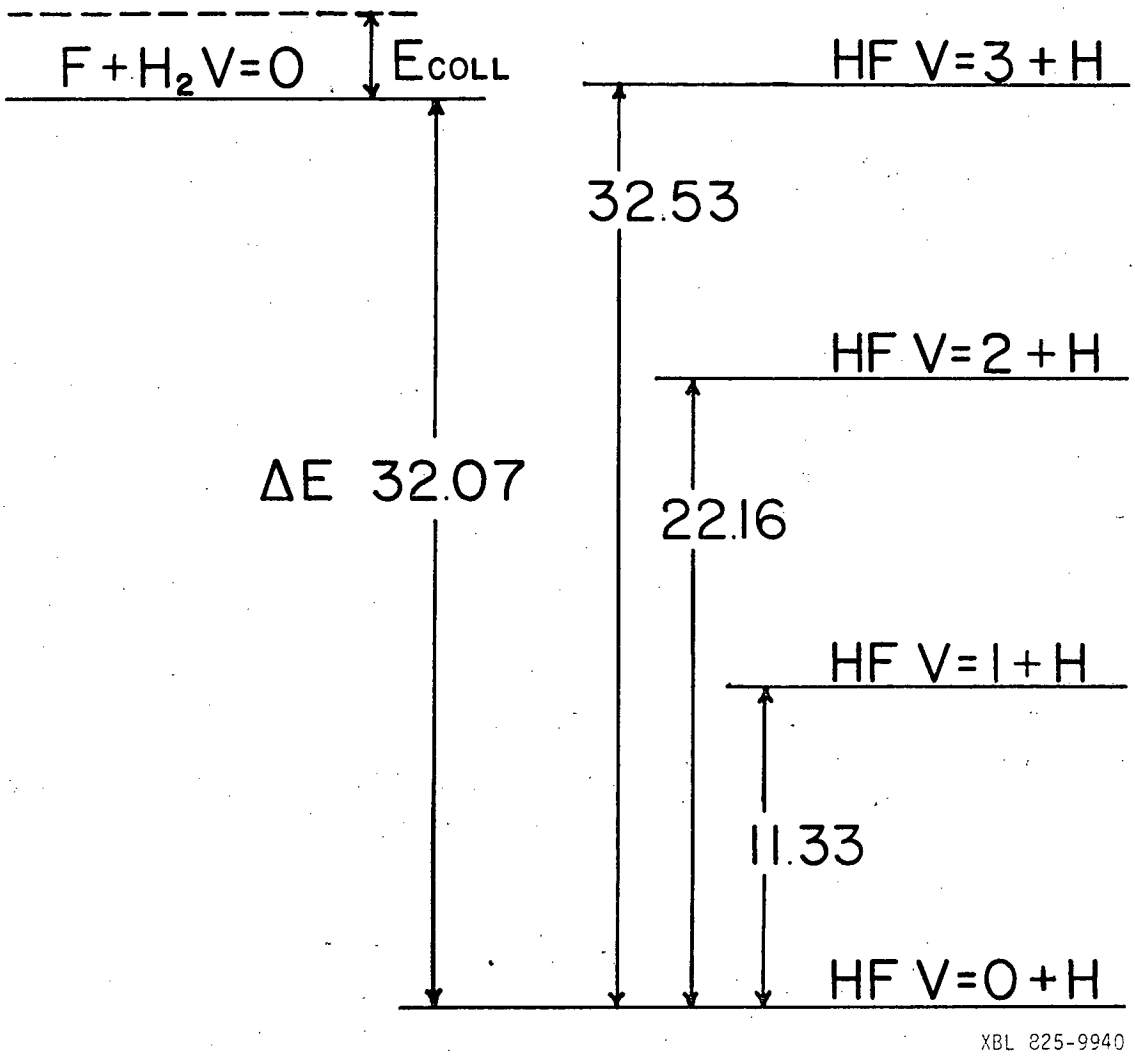
F + H2 V=0
ECOLL
HF V=3 + H
32.53
HF V=2 + H
ΔE 32.07
22.16
HF V=1 + H
11.33
HF V=0 + H
XBL 825-9940

Fig. 3.

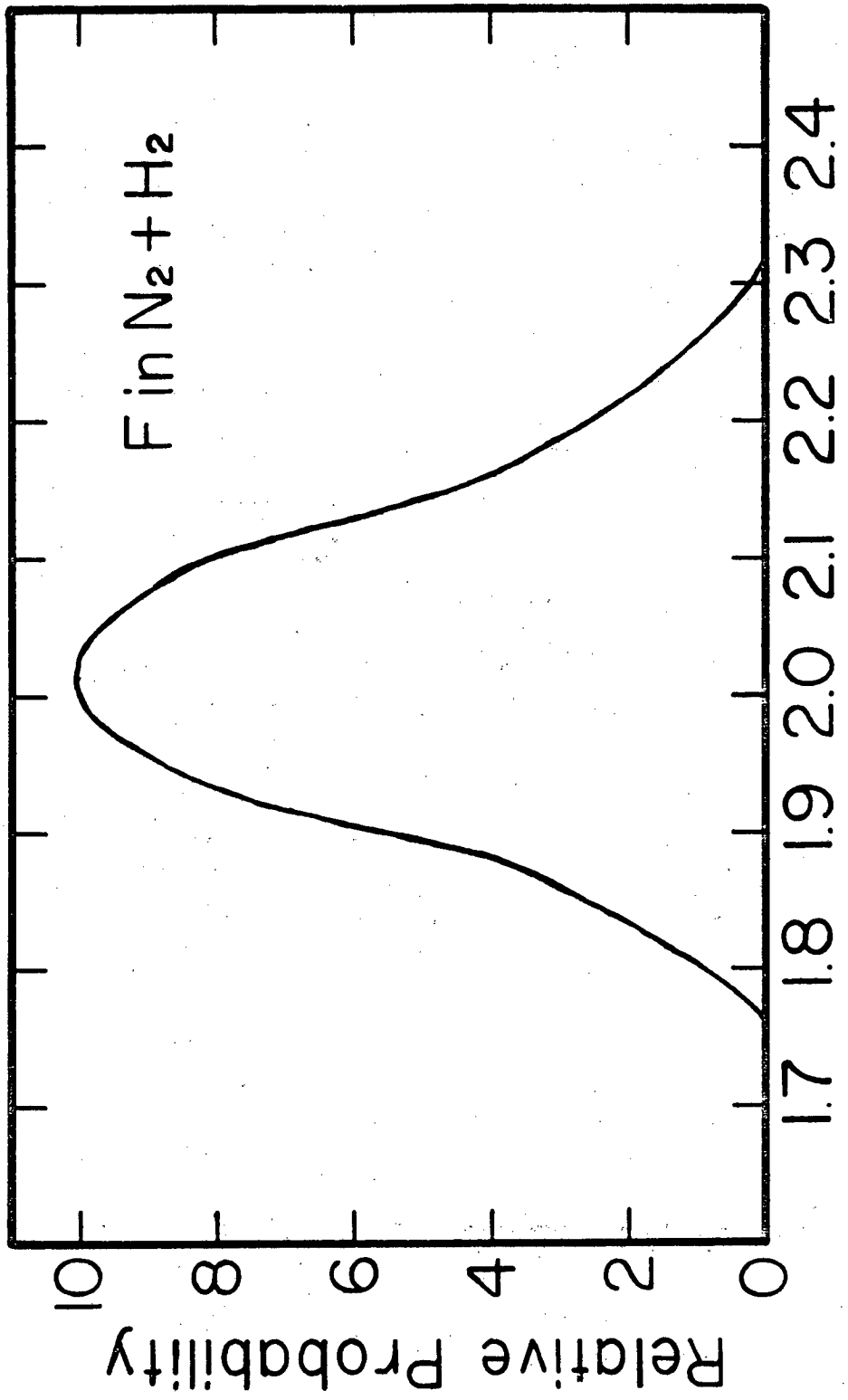

XBL 825-9941

Fig. 4.

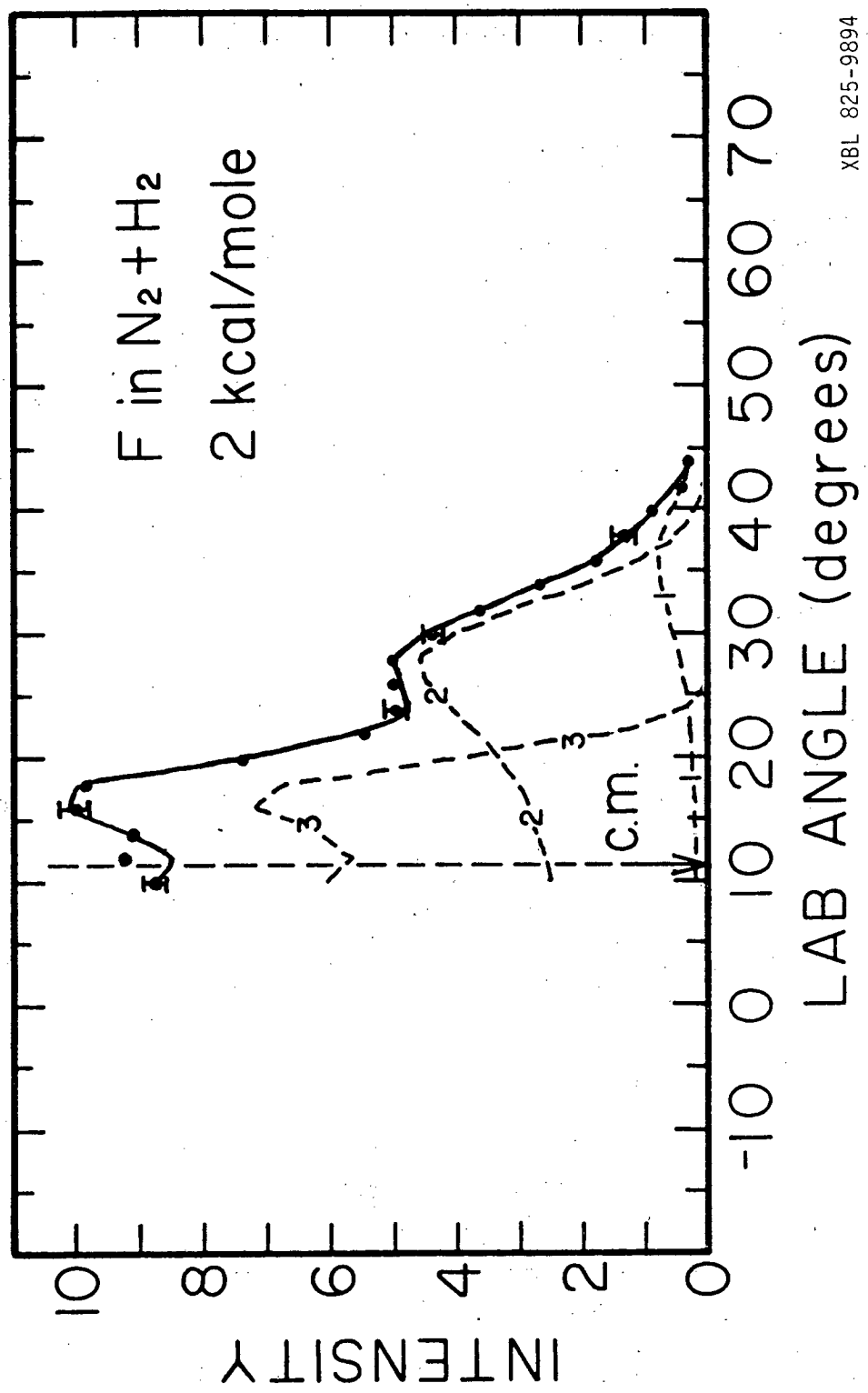
F in N2+H2
2 kcal/mole
INTENSITY
LAB ANGLE (degrees)
c.m.
XBL 825-9894

Fig. 5.

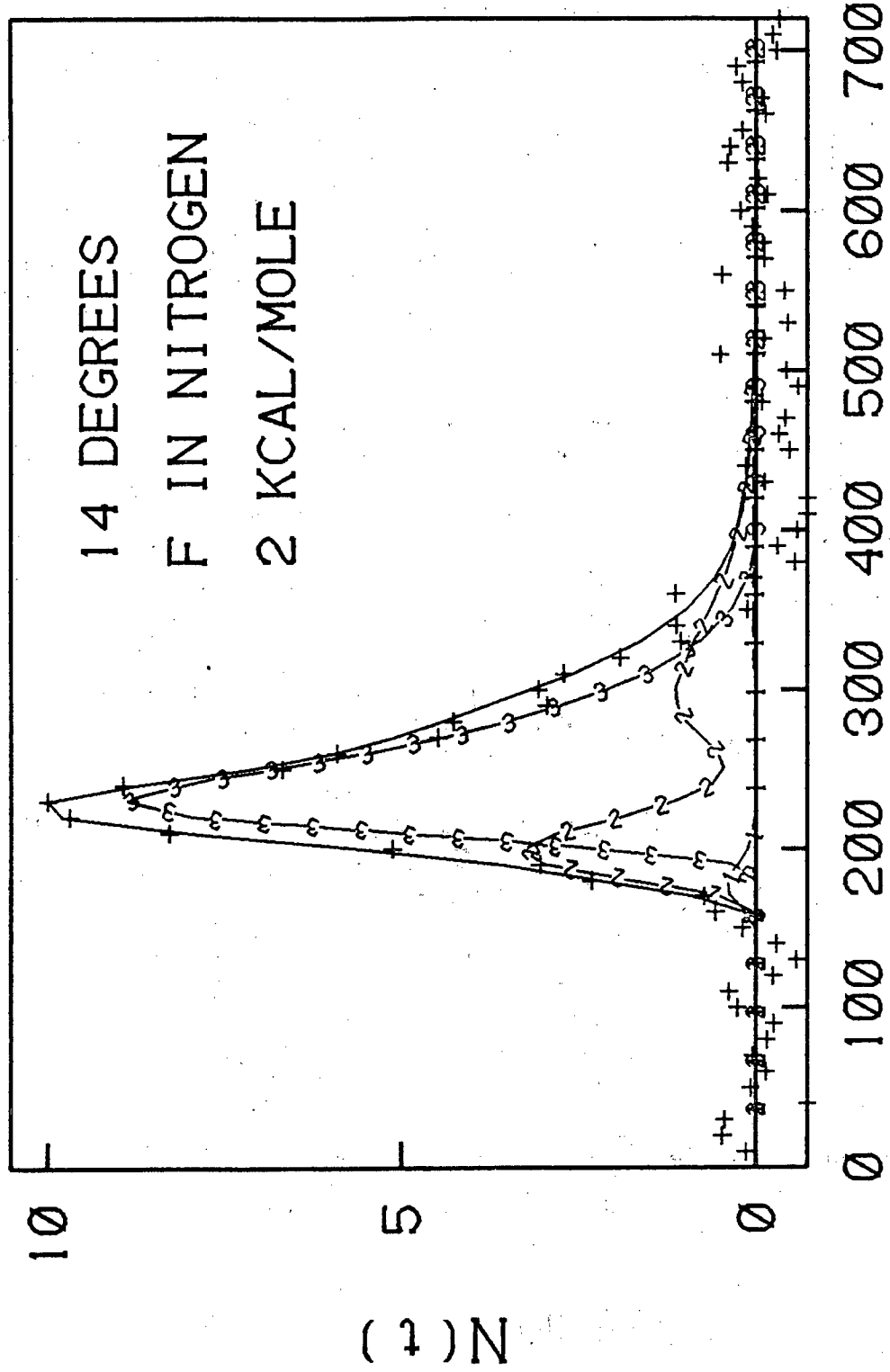

XBL 825-9922

Fig. 6.

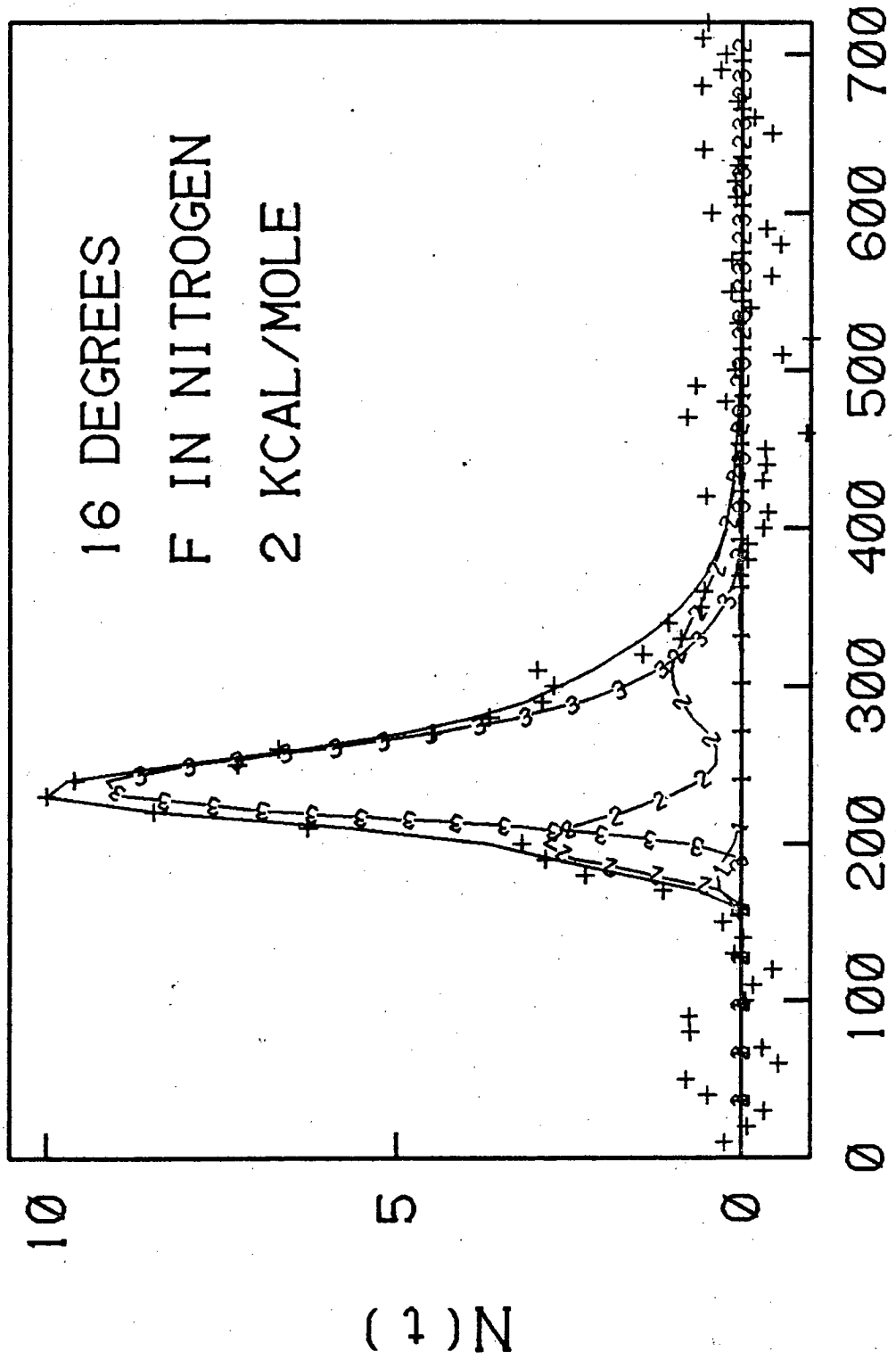

XBL 825-9923

Fig. 7.

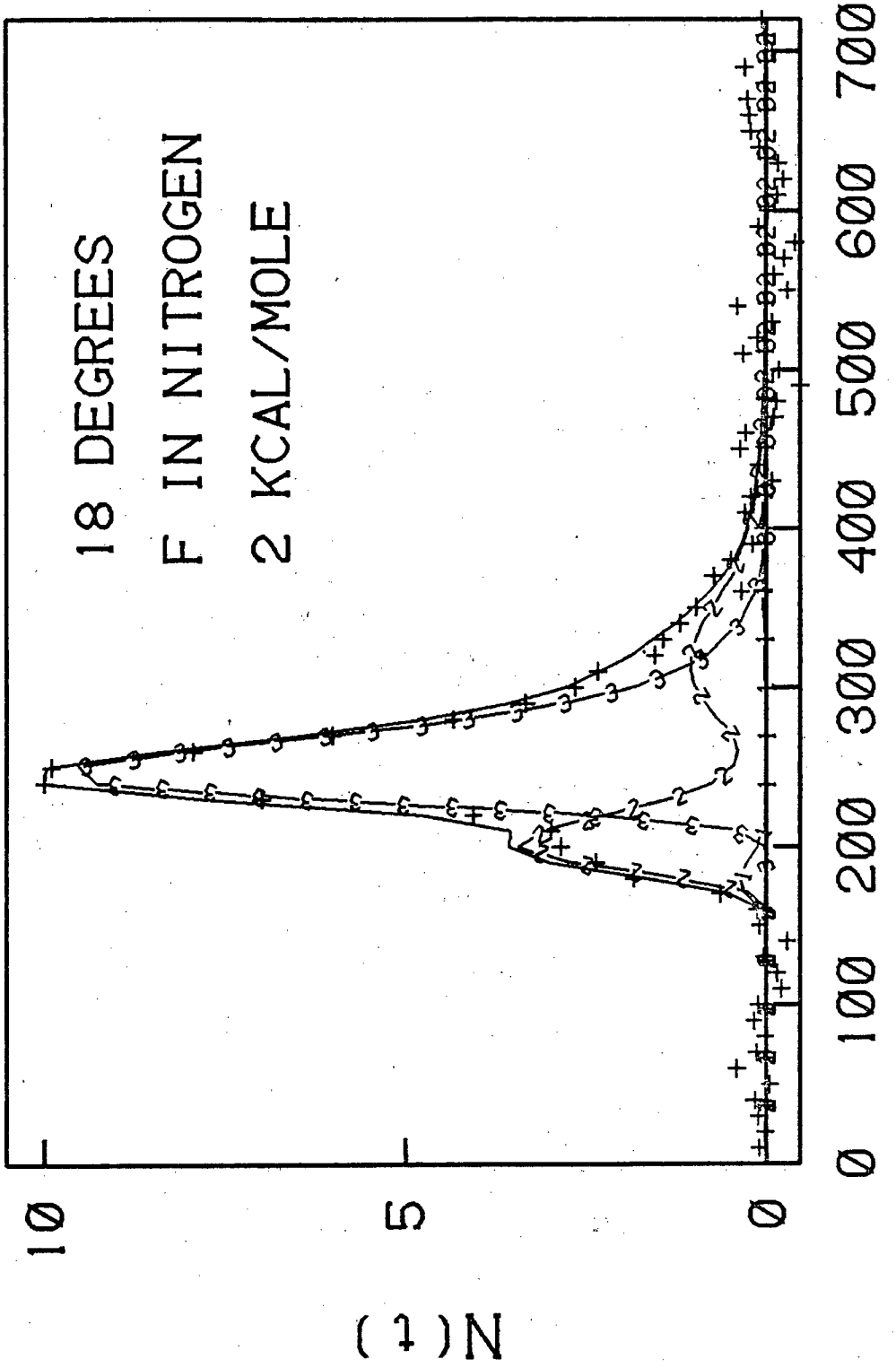

XBL 825-9924

Fig. 8.

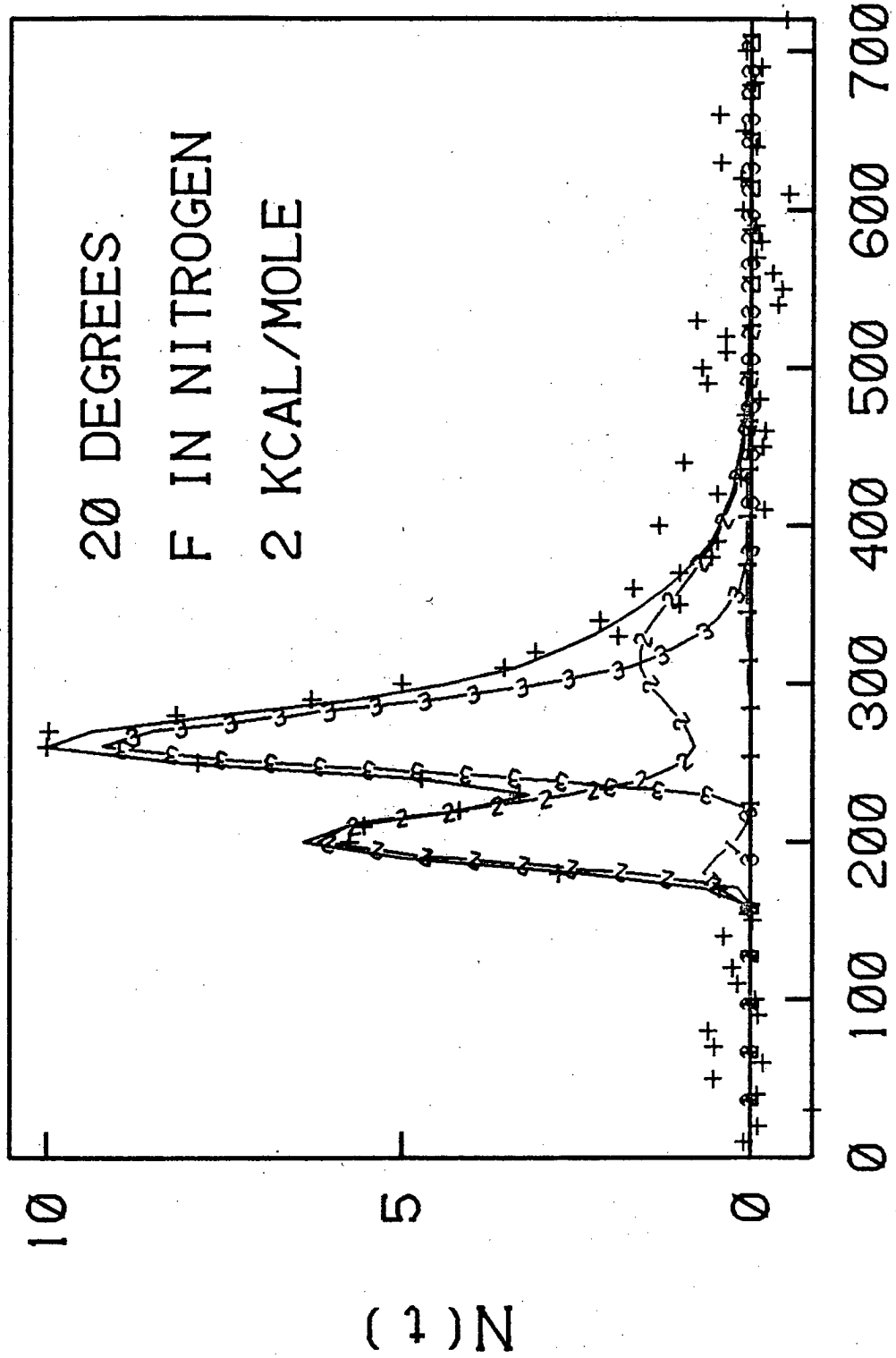

XBL 825-9925

Fig. 9.

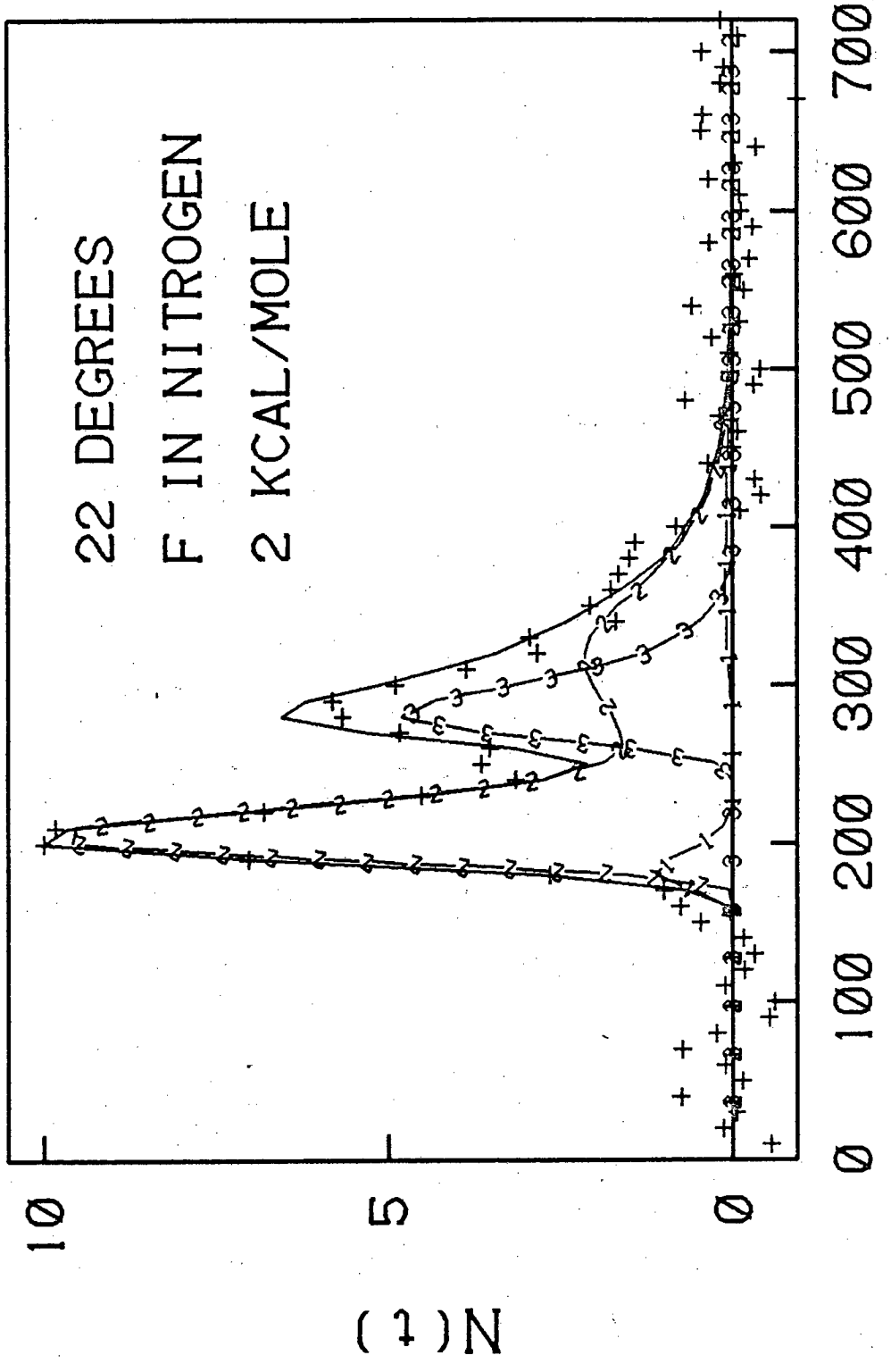

XBL 825-9926

Fig. 10.

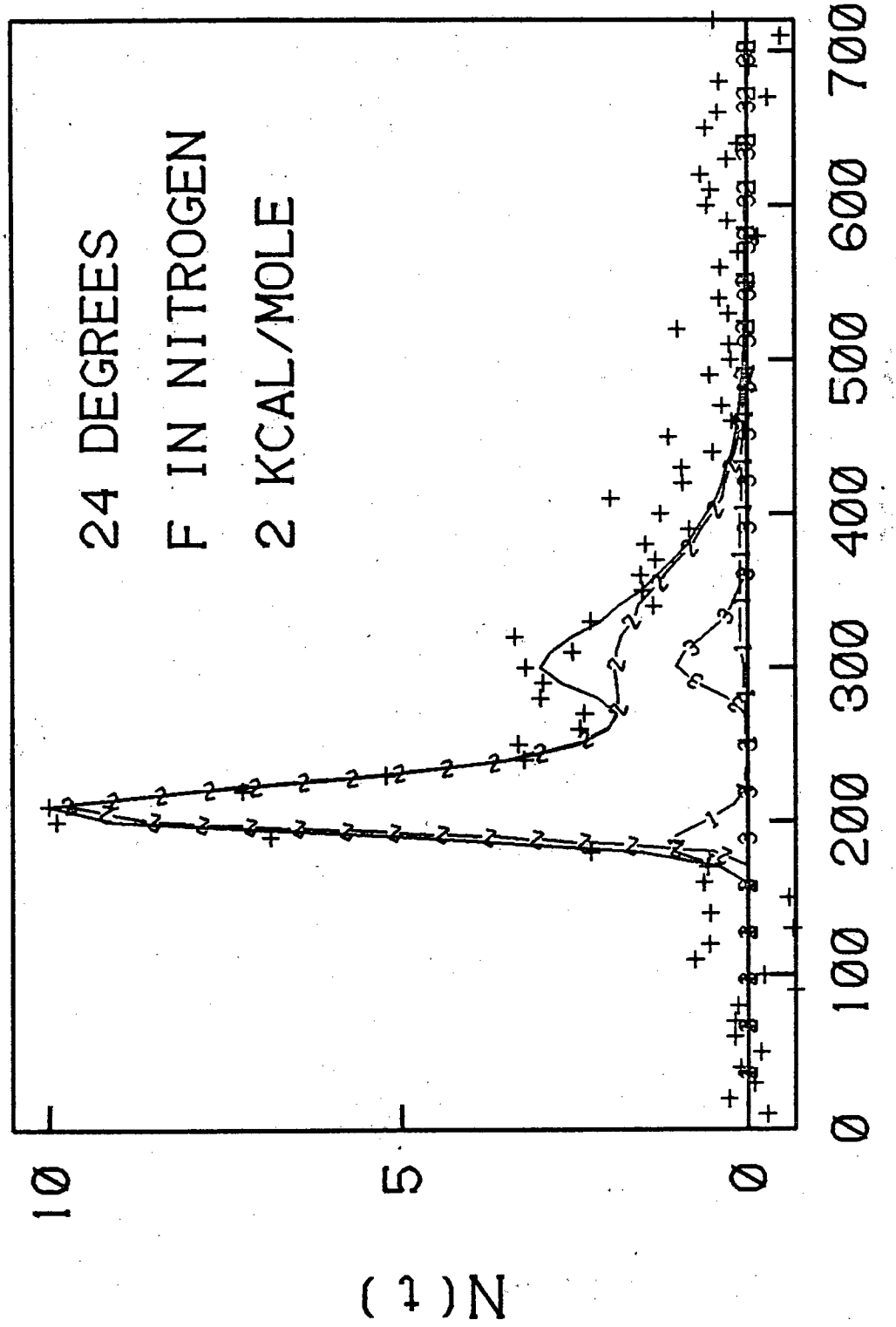

XBL 825-9927

Fig. 11.

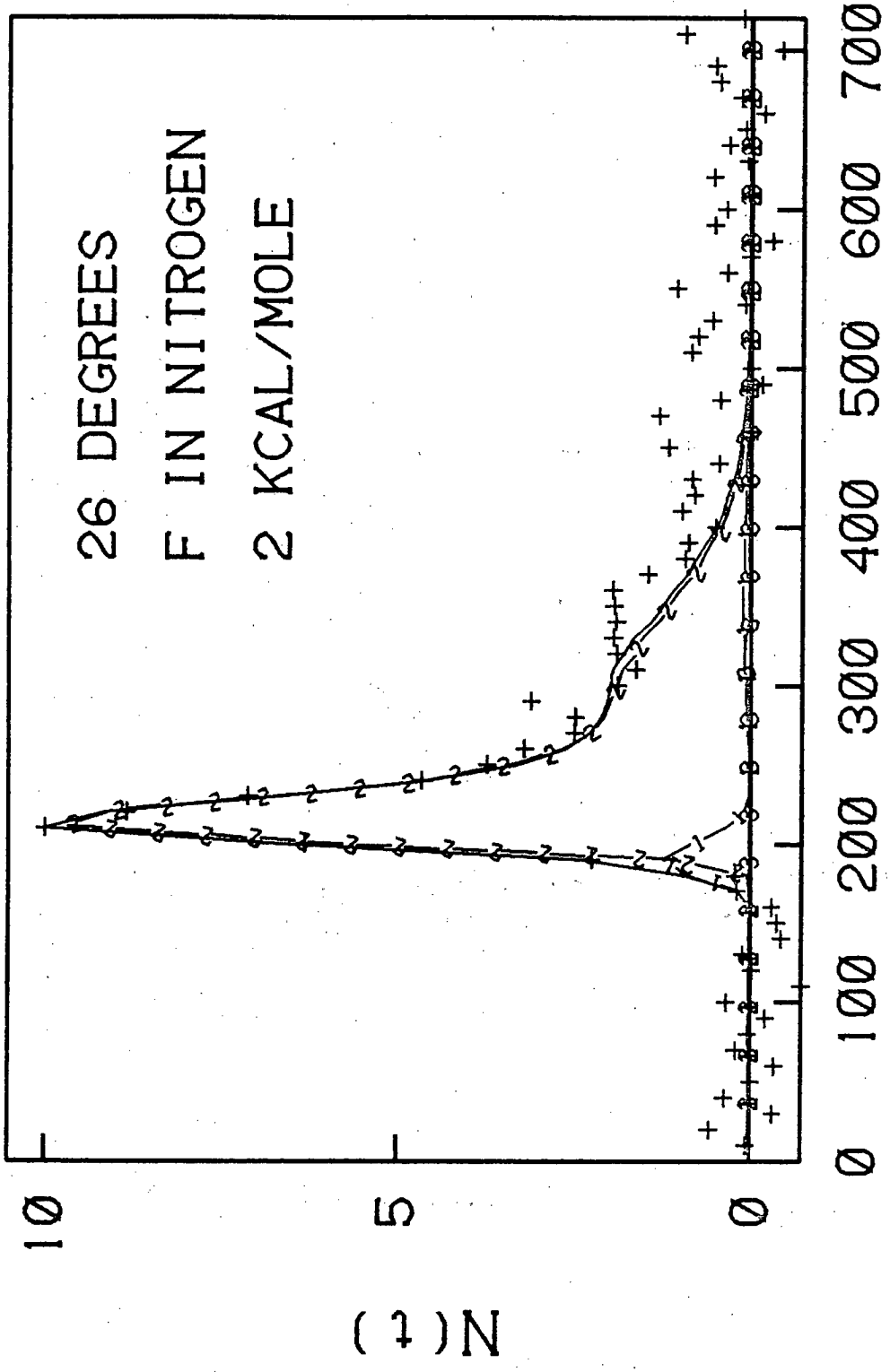

XBL 825-9928

Fig. 12.

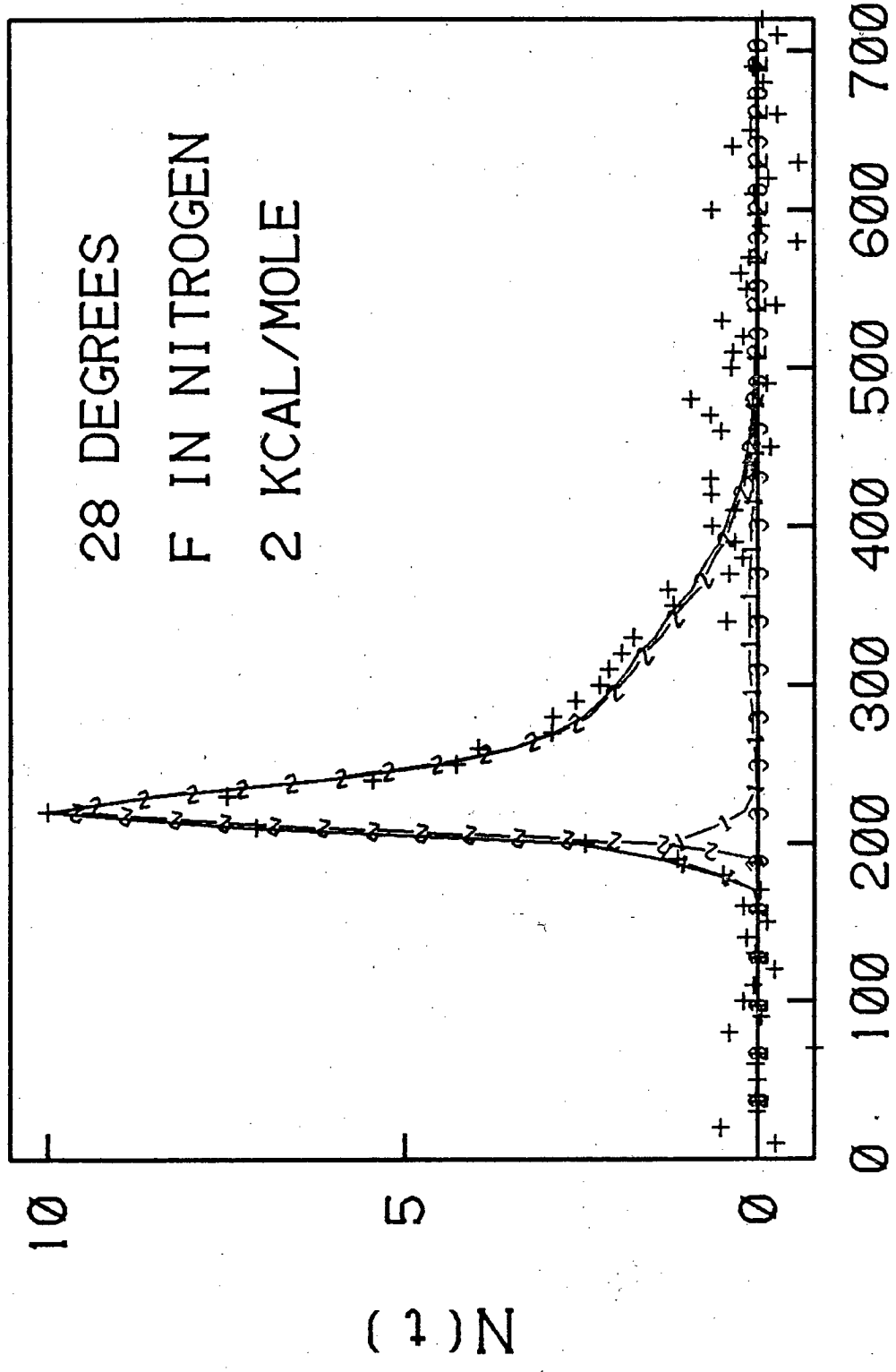

XBL 825-9929

Fig. 13.

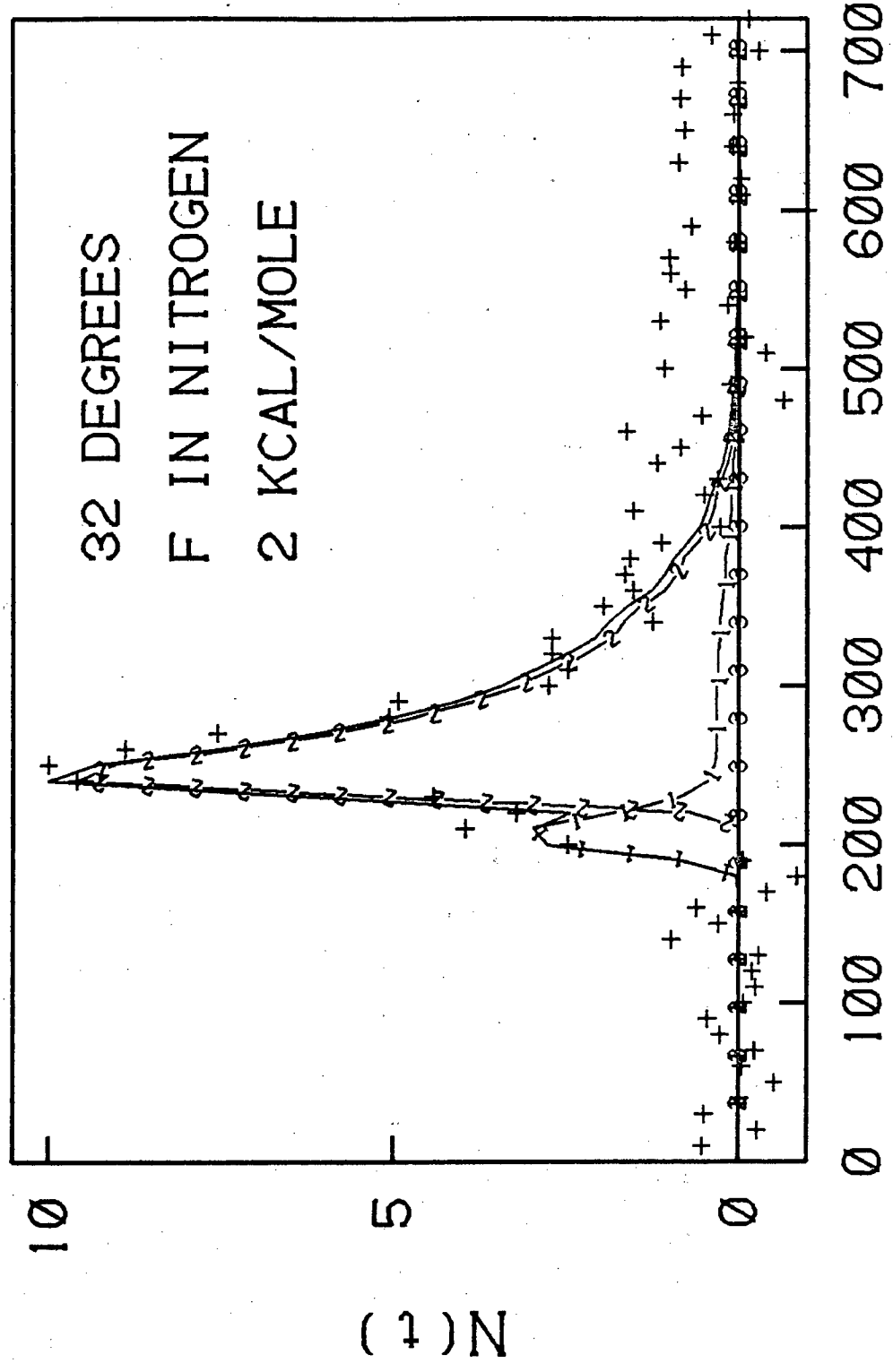

XBL 825-9930

Fig. 14.

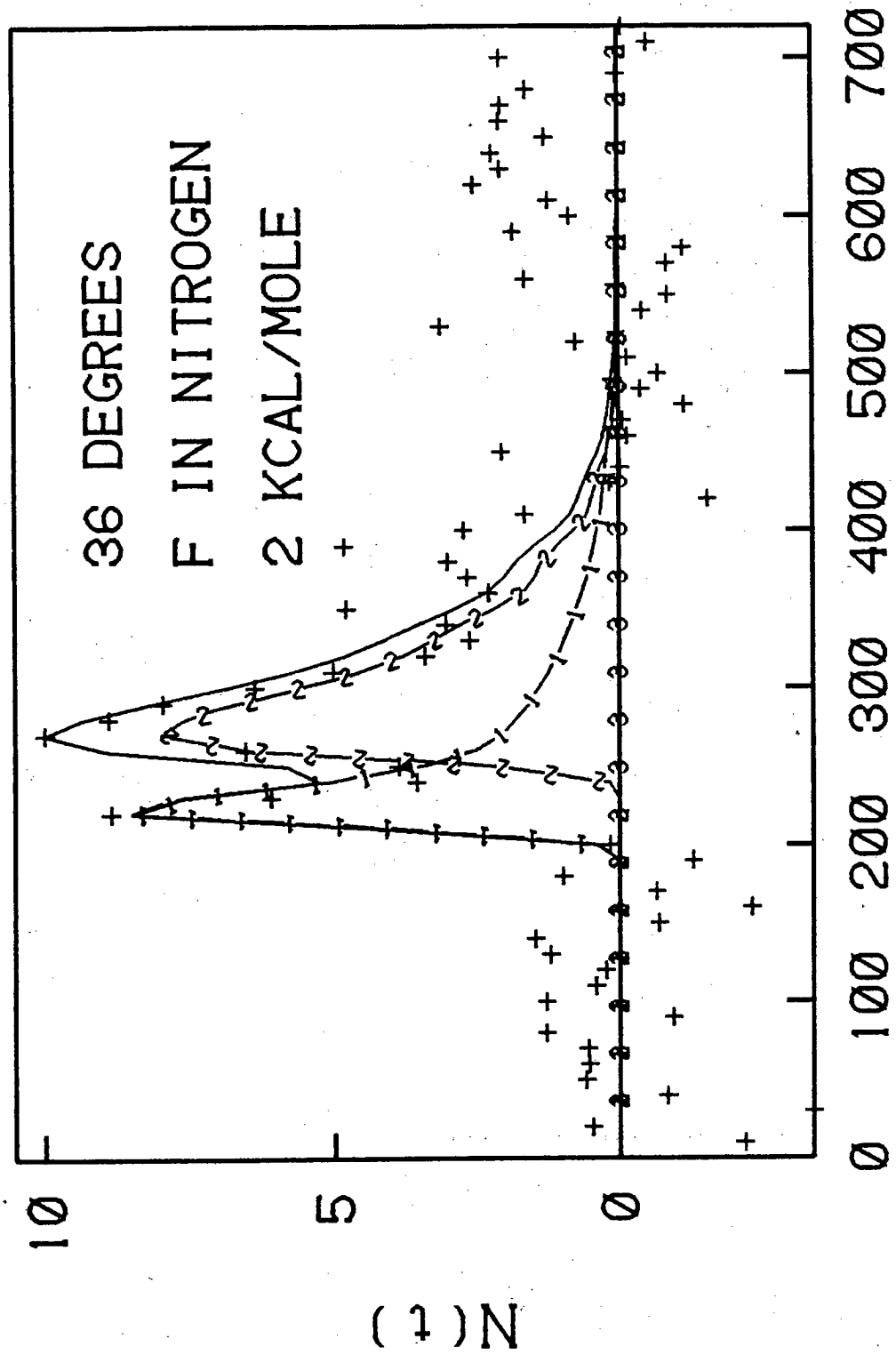

XBL 825-9931

Fig. 15.

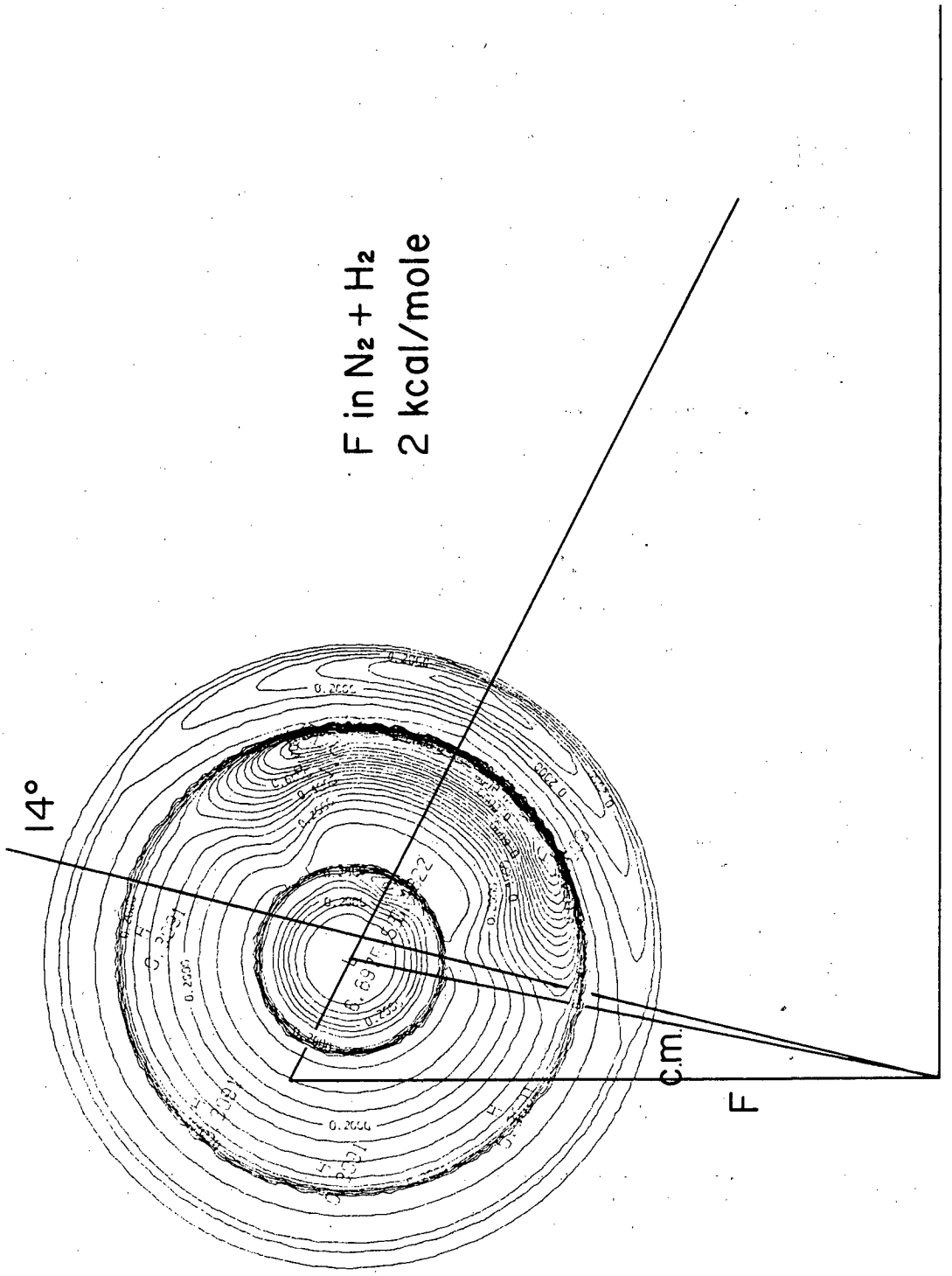

XBL 825-9937

Fig. 16.

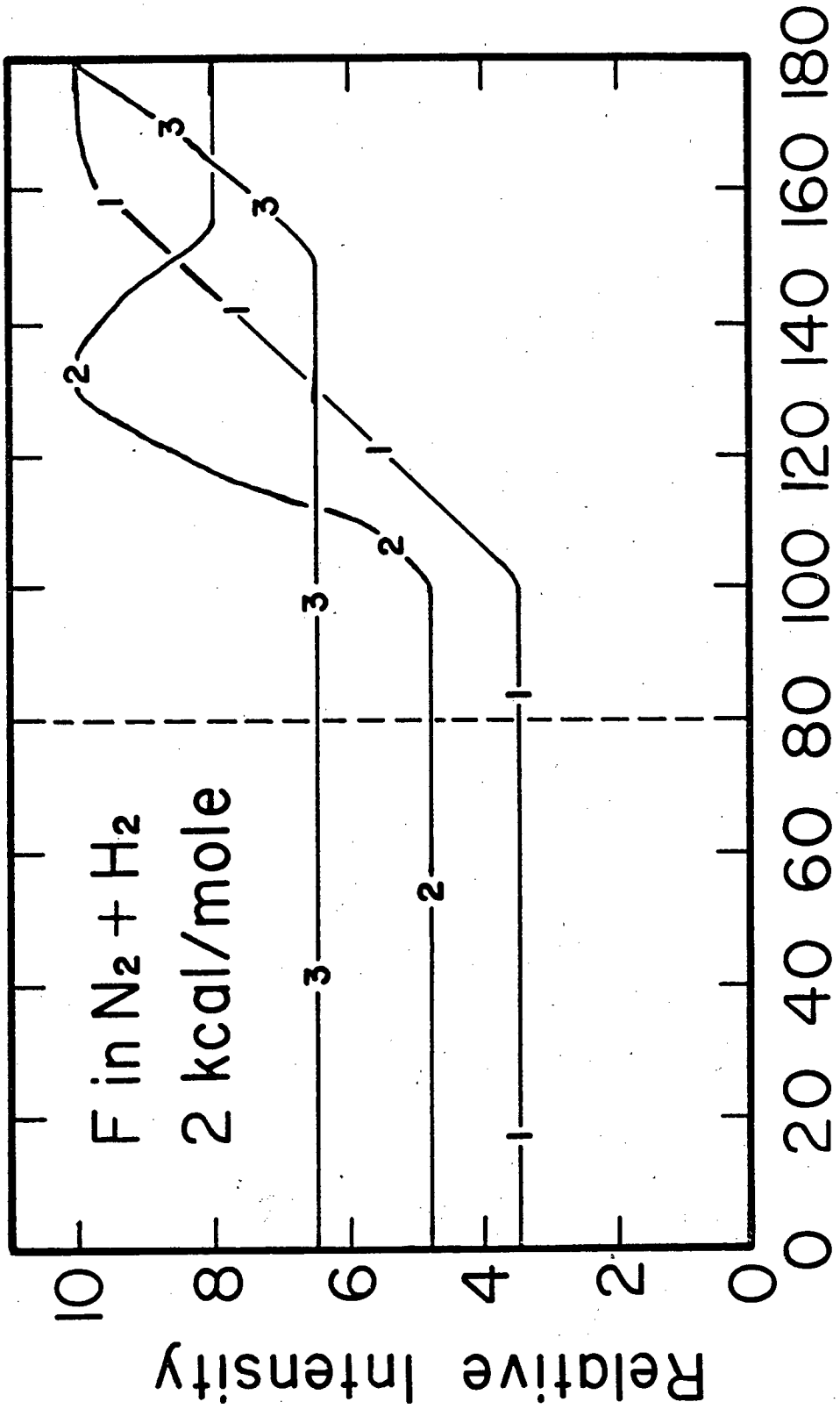

XBL 825-9932

Fig. 17.

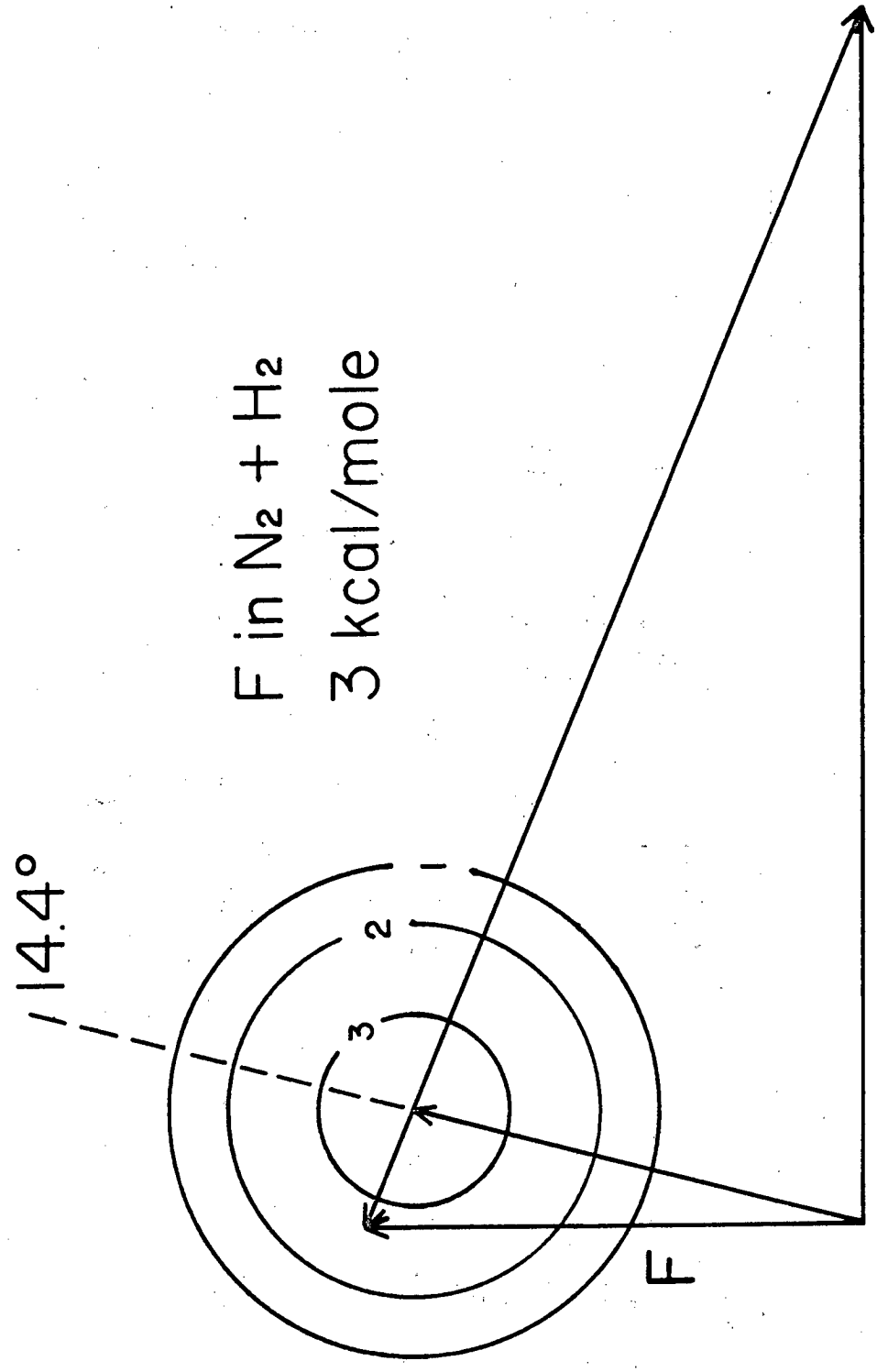

XBL 825-9942

Fig. 18.

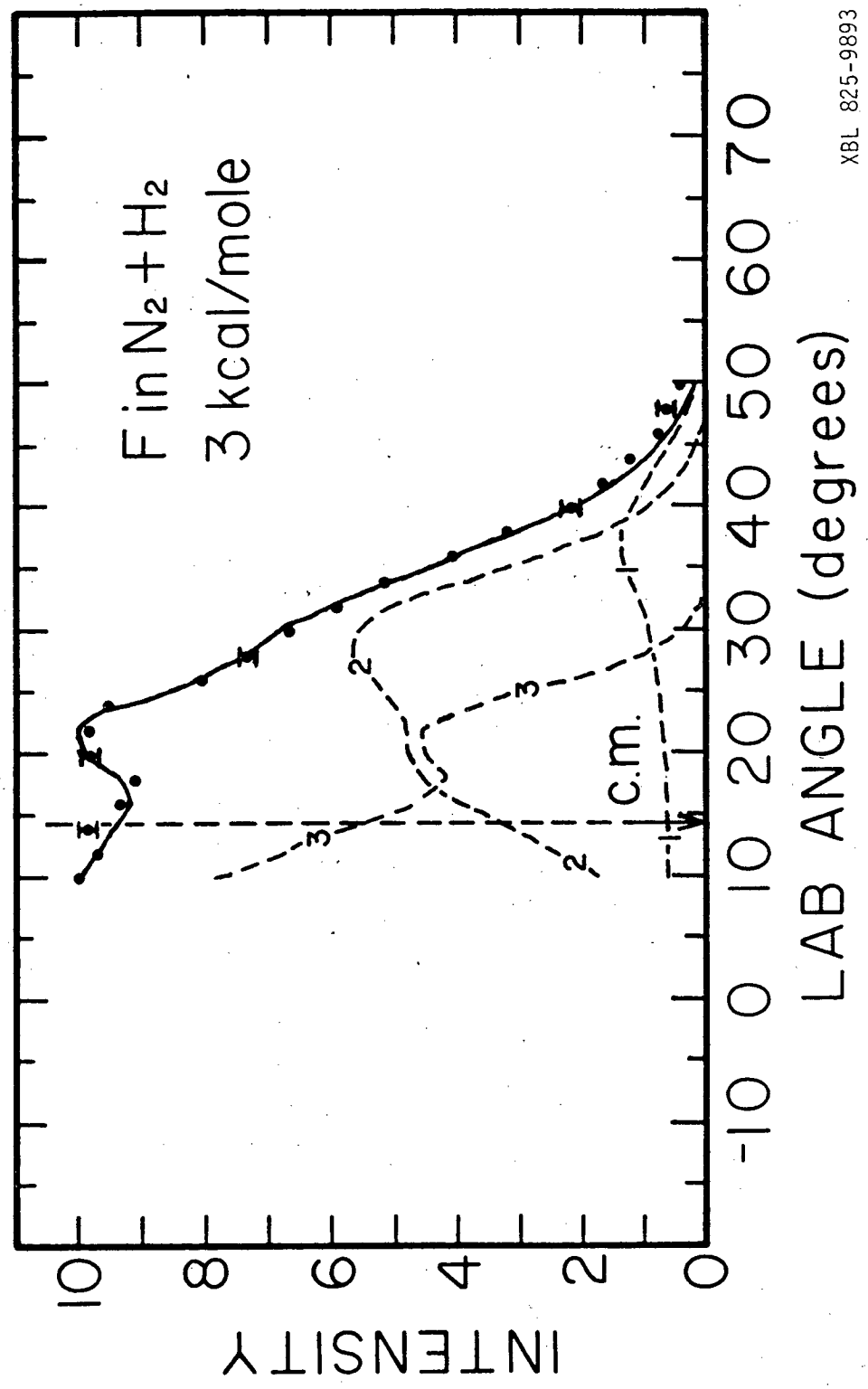

XBL 825-9893

Fig. 19.

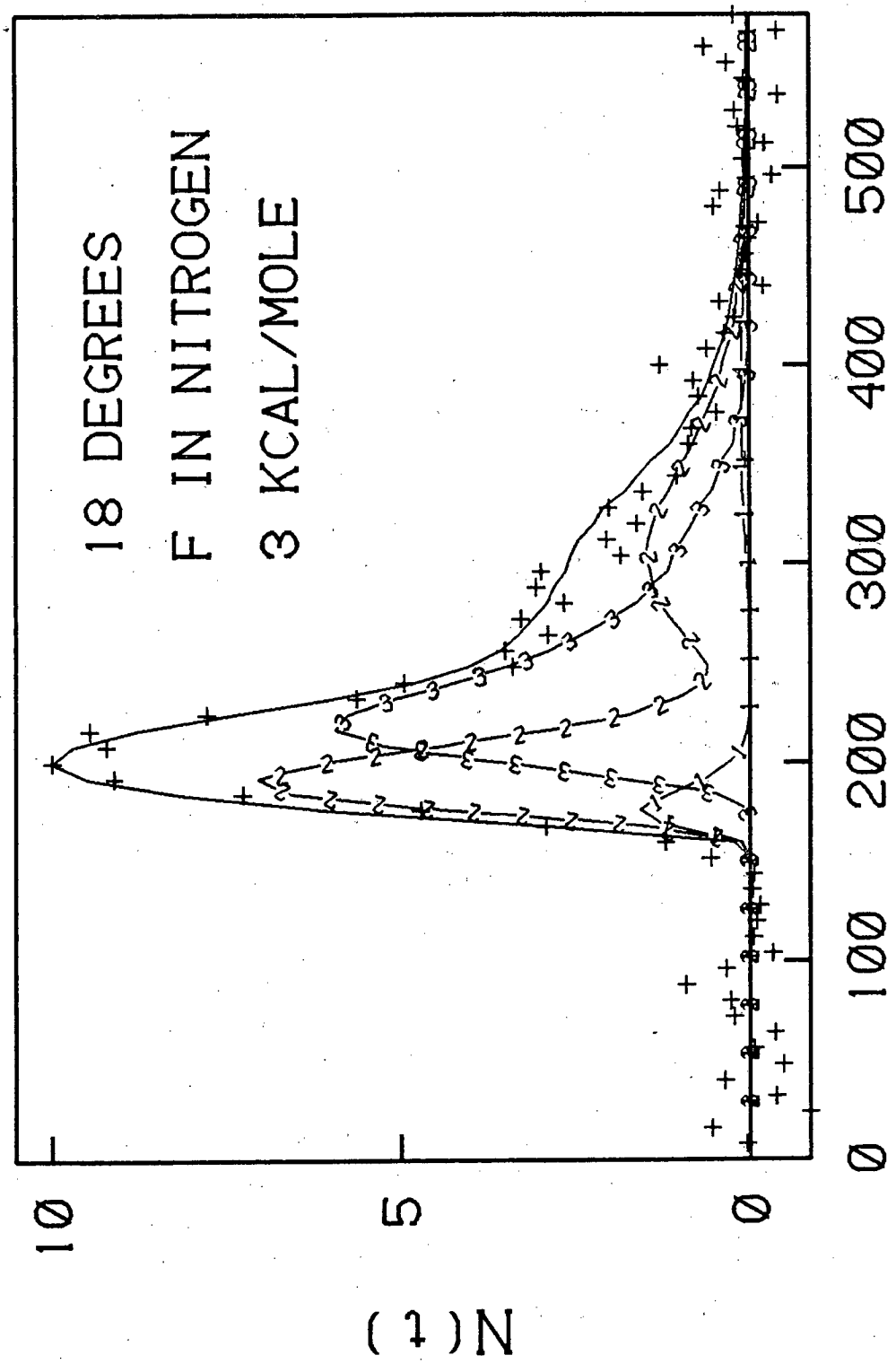

XBL 825-9921

Fig. 20.

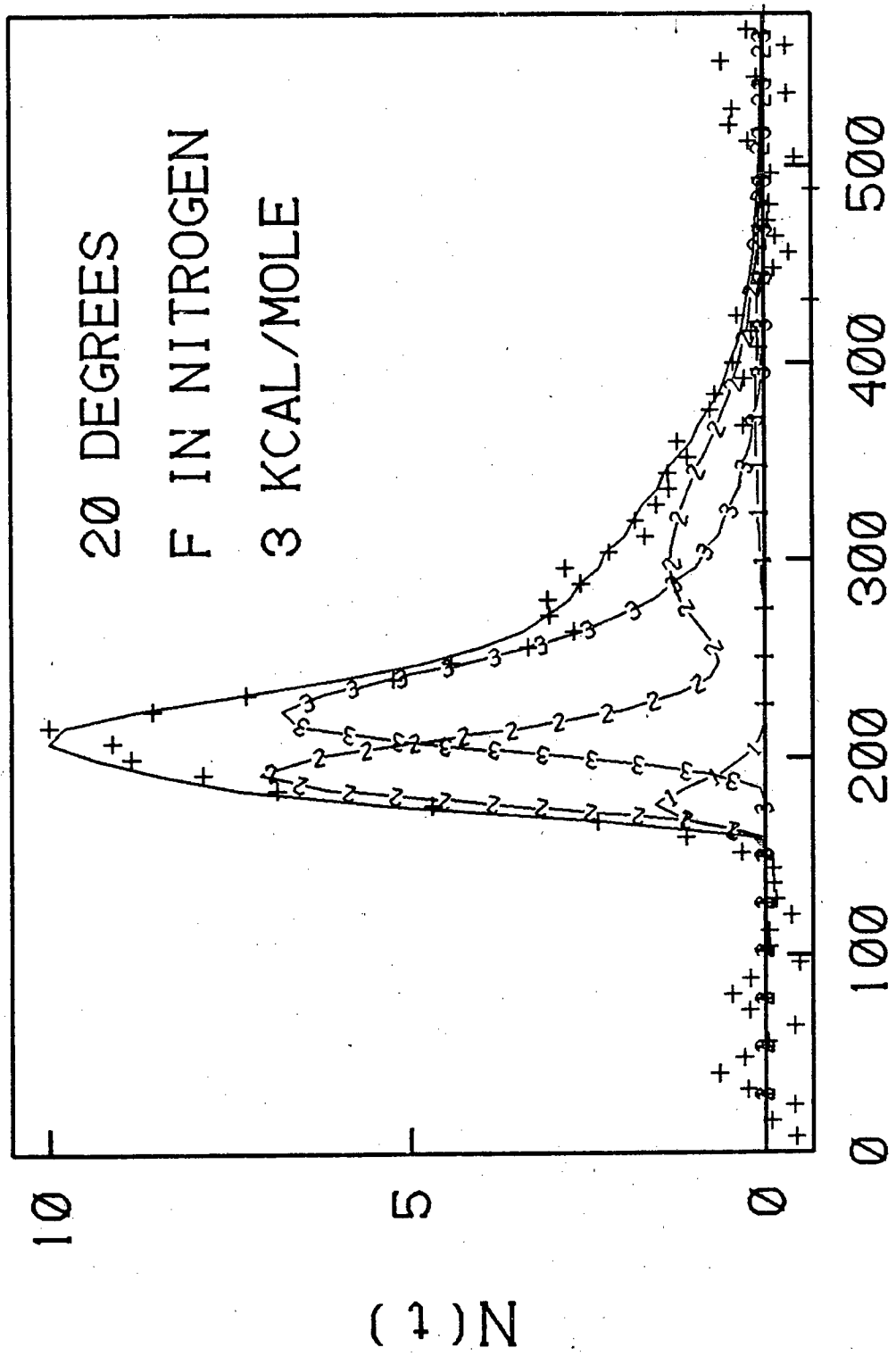

XBL 825-9920

Fig. 21.

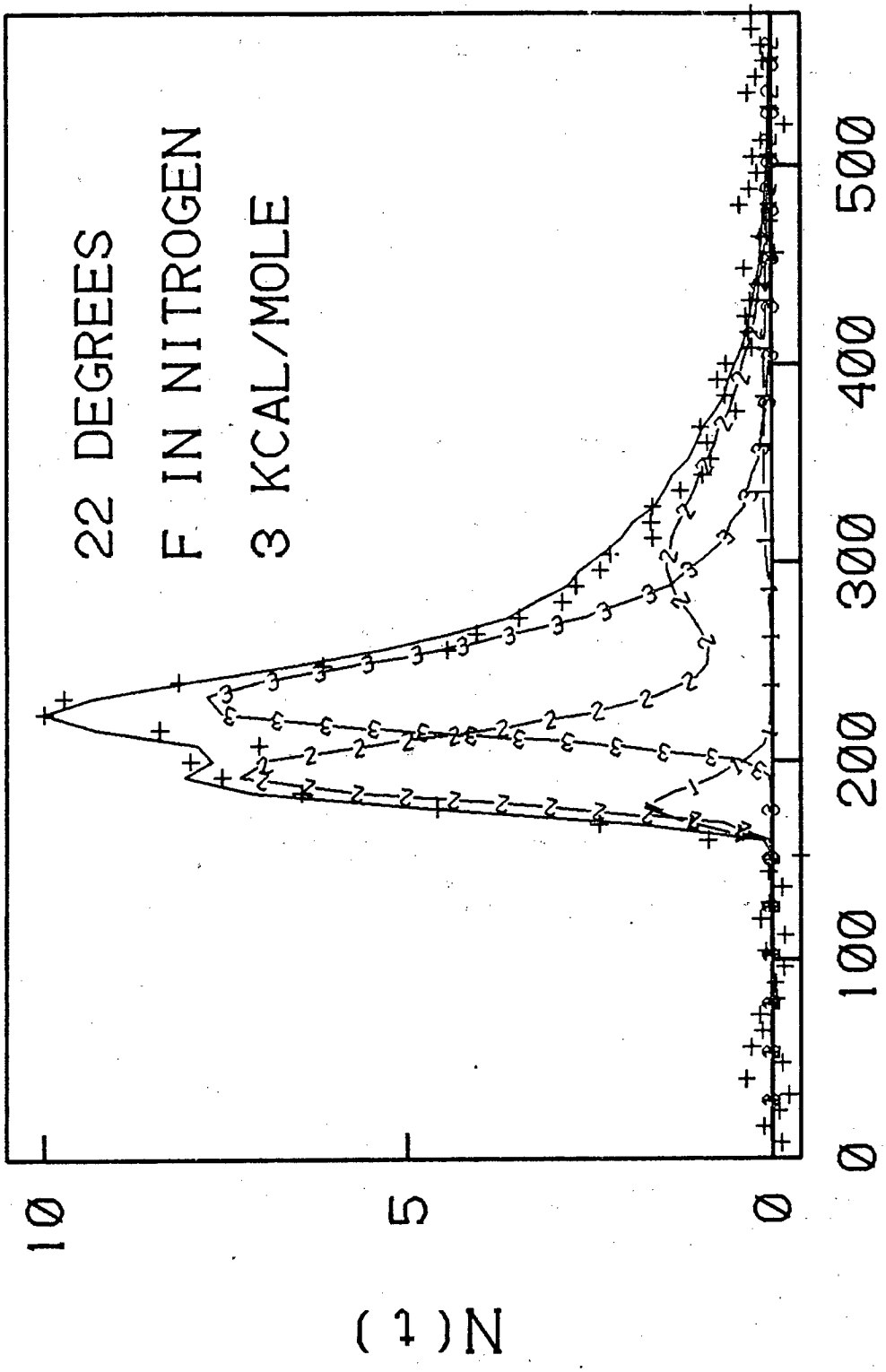

XBL 825-9919

Fig. 22.

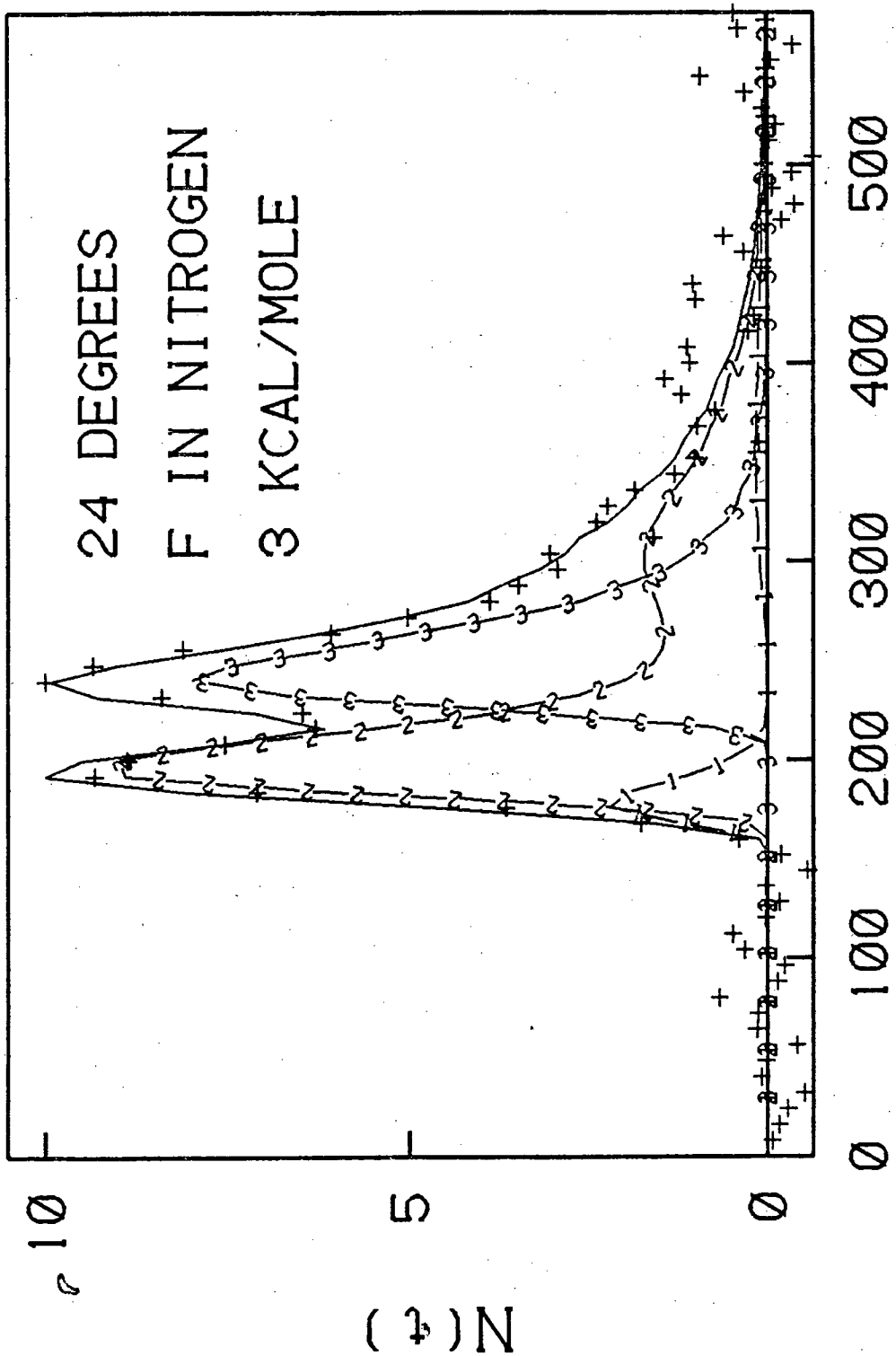

XBL 825-9918

Fig. 23.

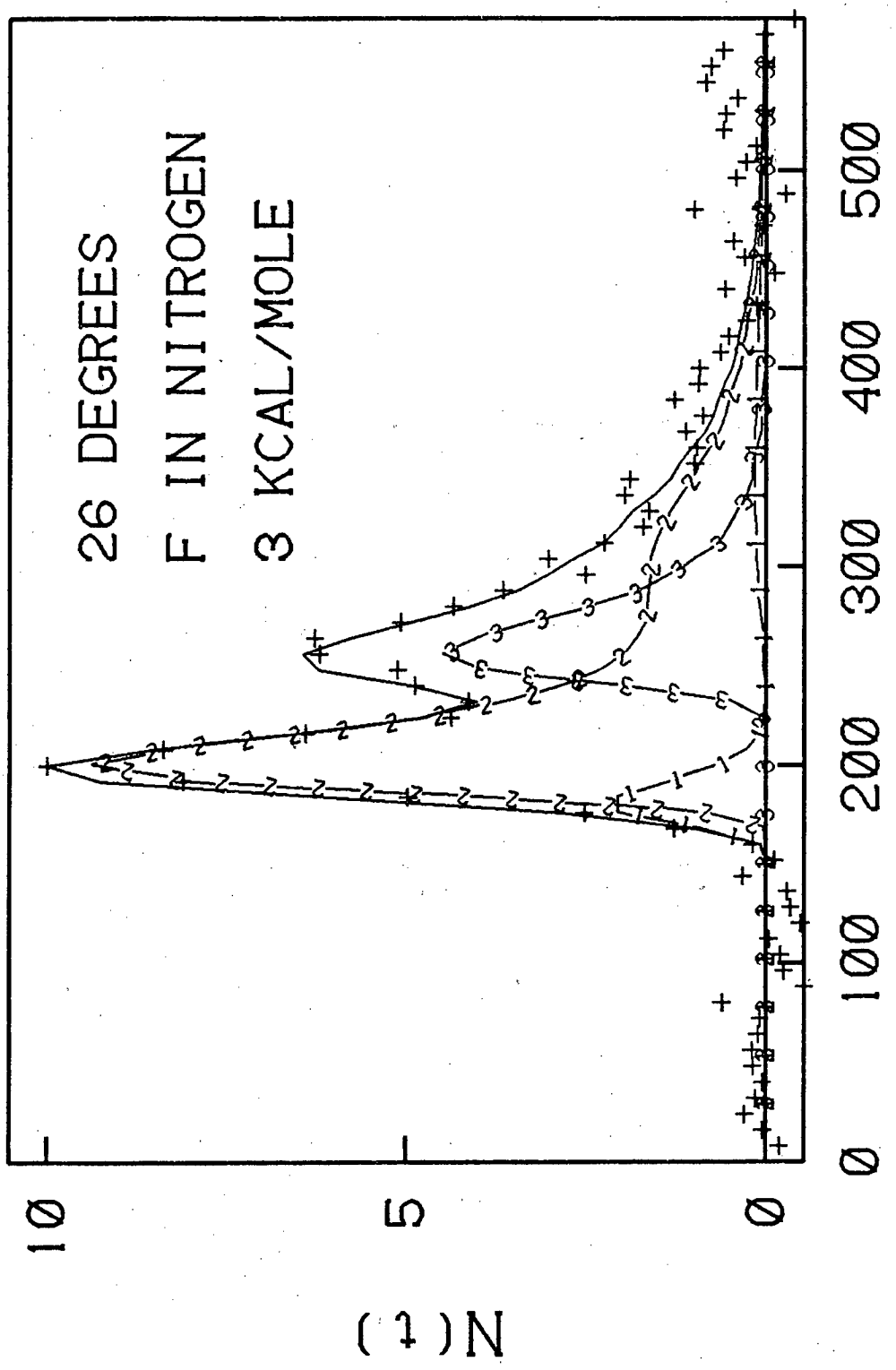

XBL 825-9917

Fig. 24.

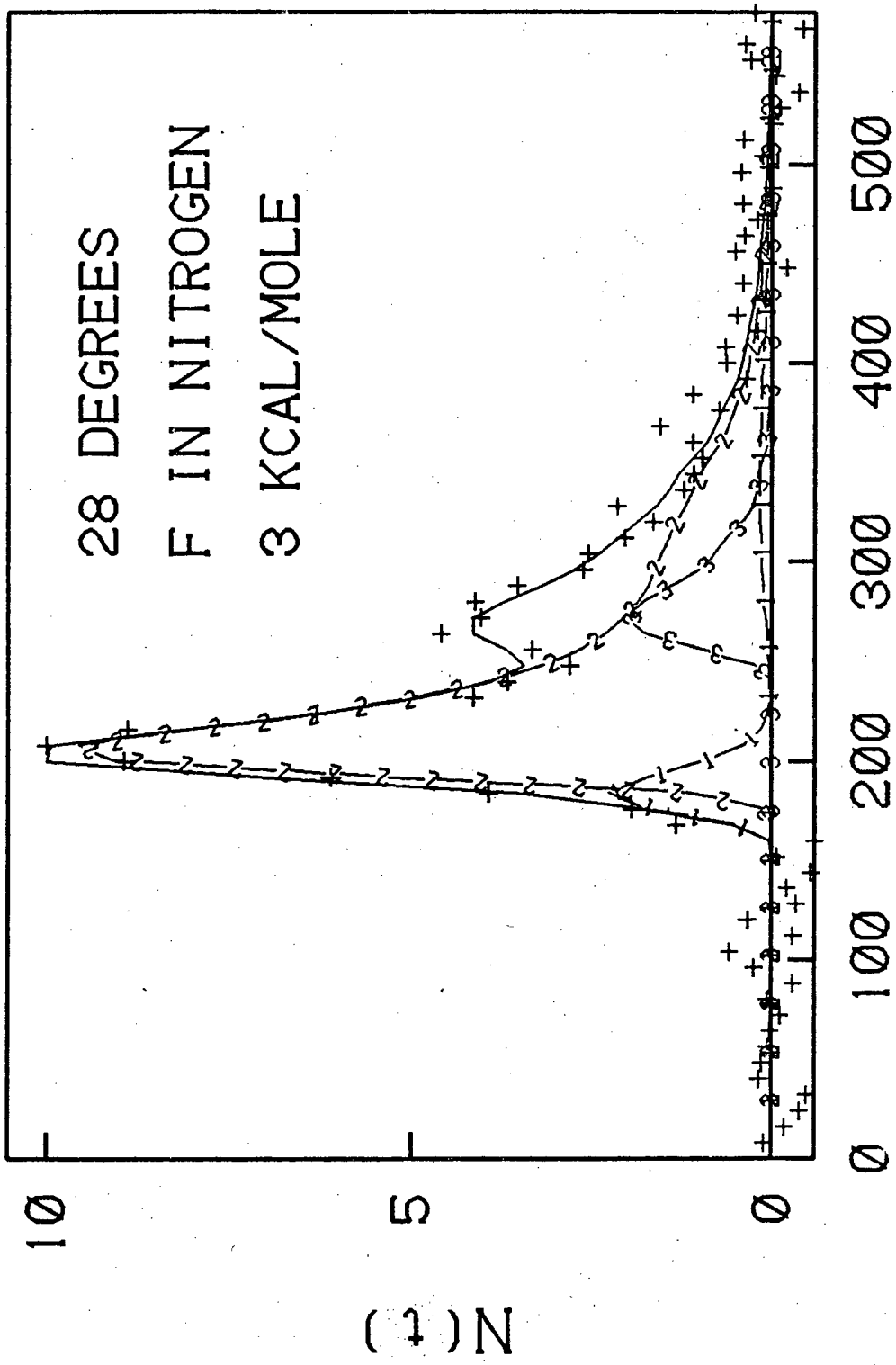

XBL 825-9916

Fig. 25.

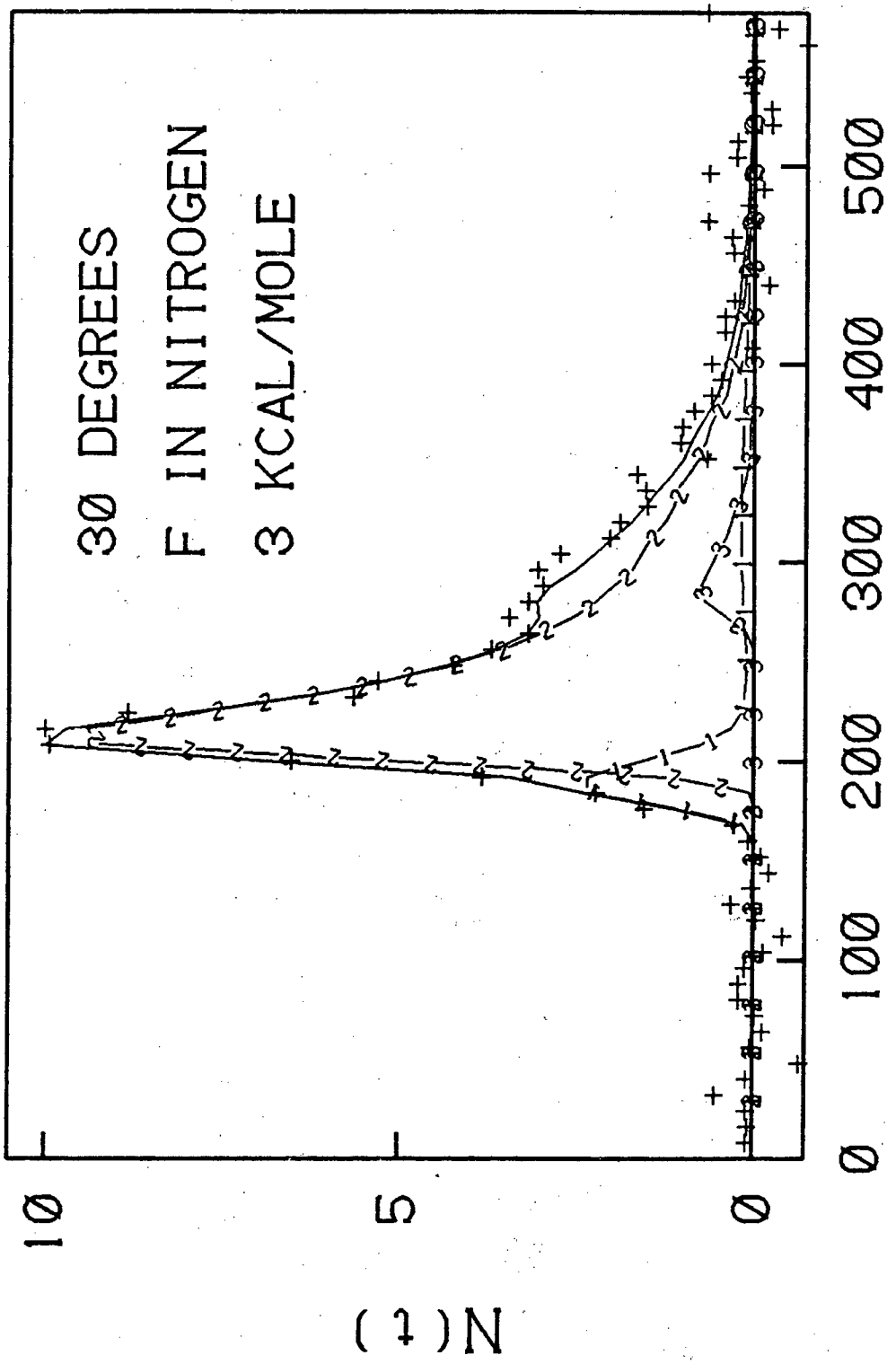

XBL 825-9915

Fig. 26.

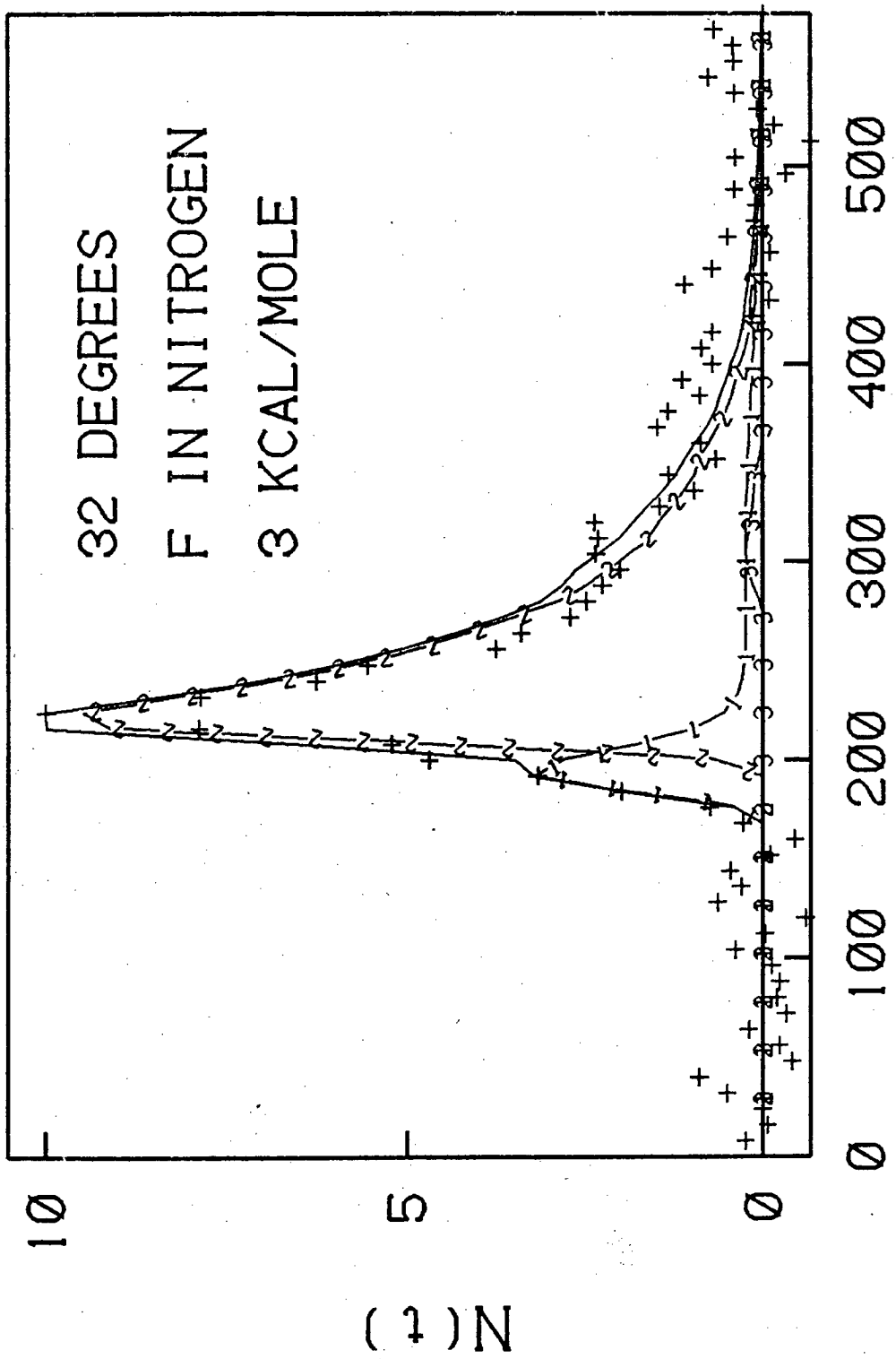

XBL 825-9914

Fig. 27.

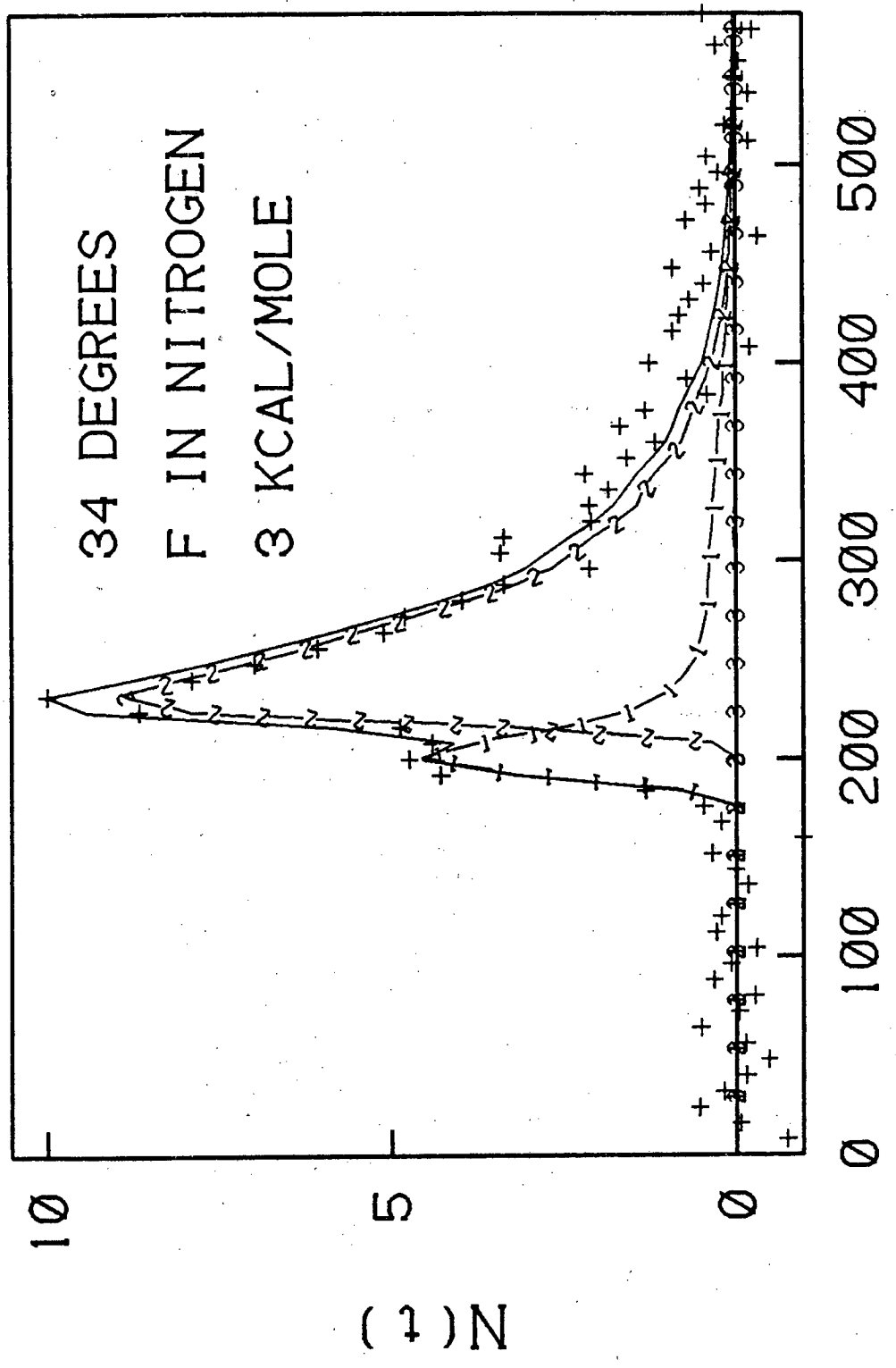

XBL 825-9913

Fig. 28.

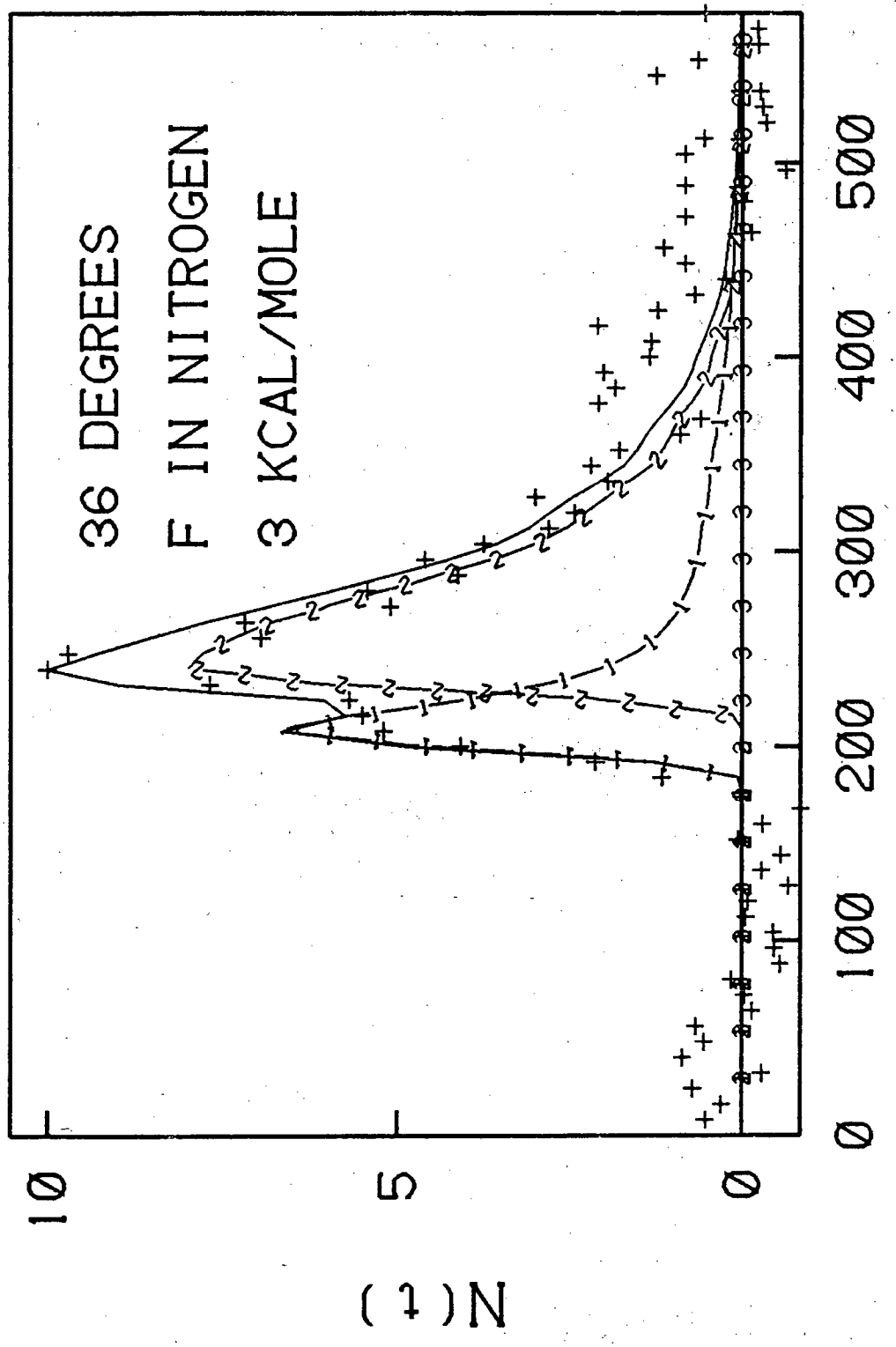

XBL 825-9912

Fig. 29.

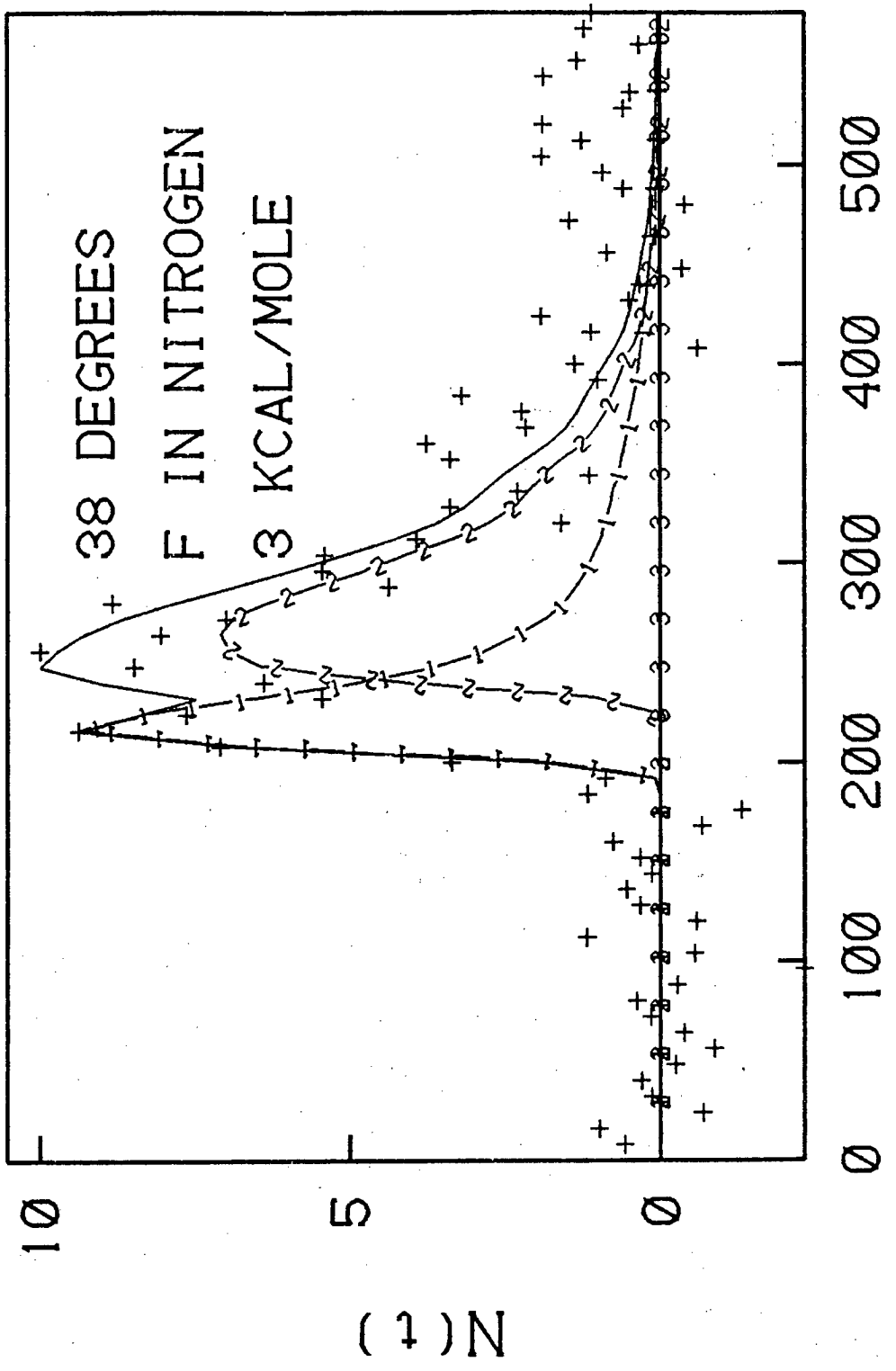

XBL 825-9911

Fig. 30.

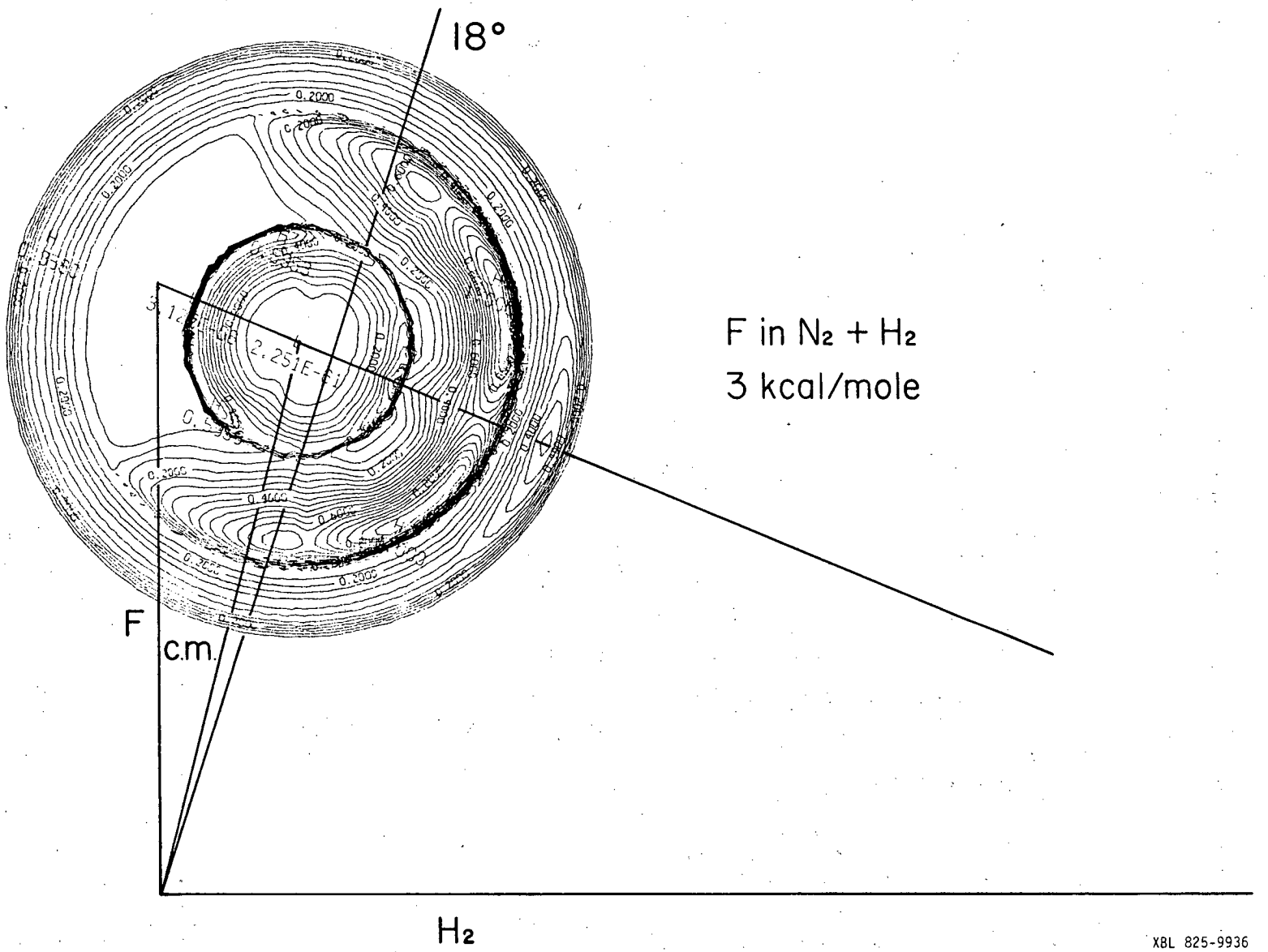

Fig. 31.

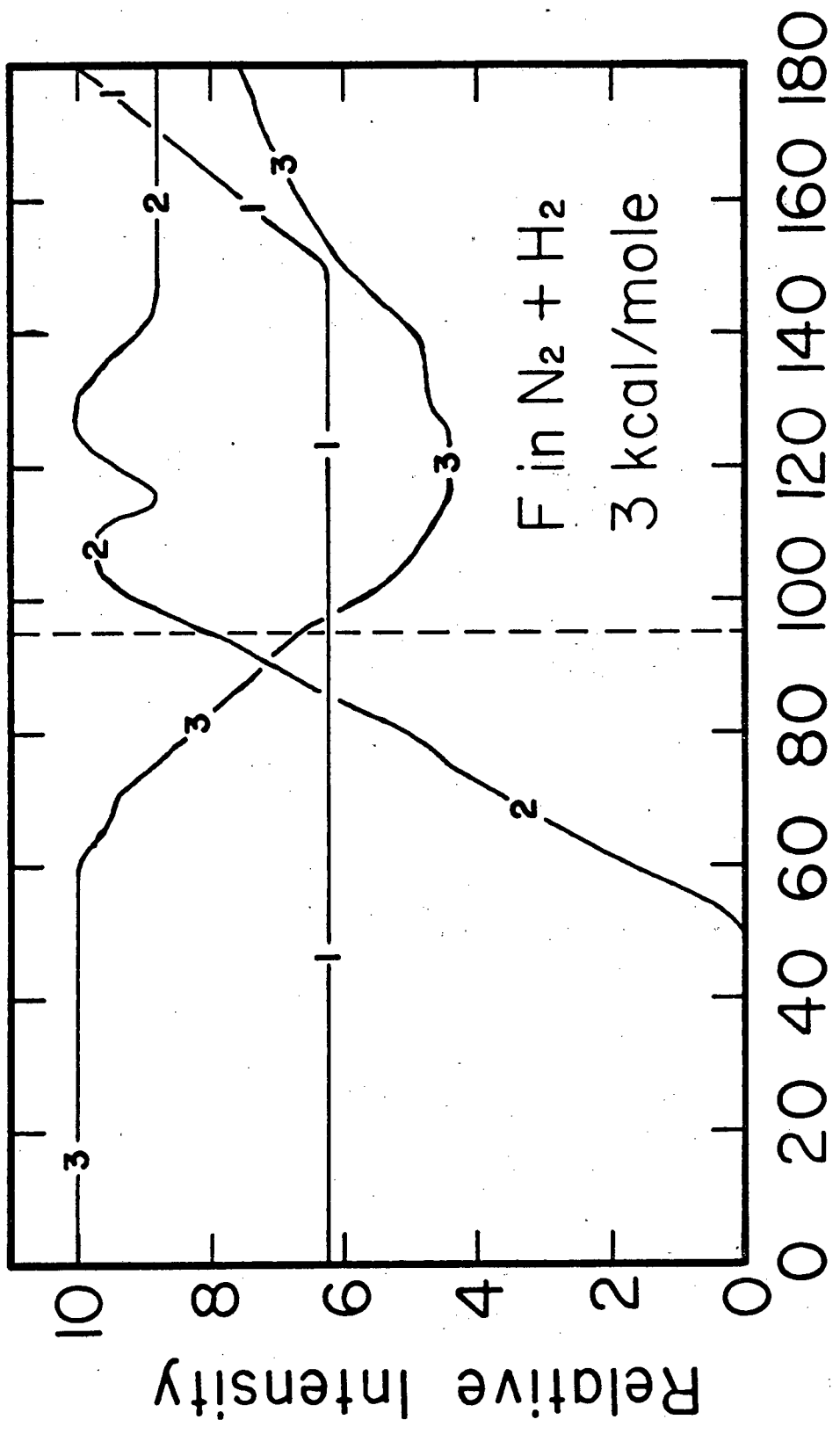

XBL 825-9933

Fig. 32.

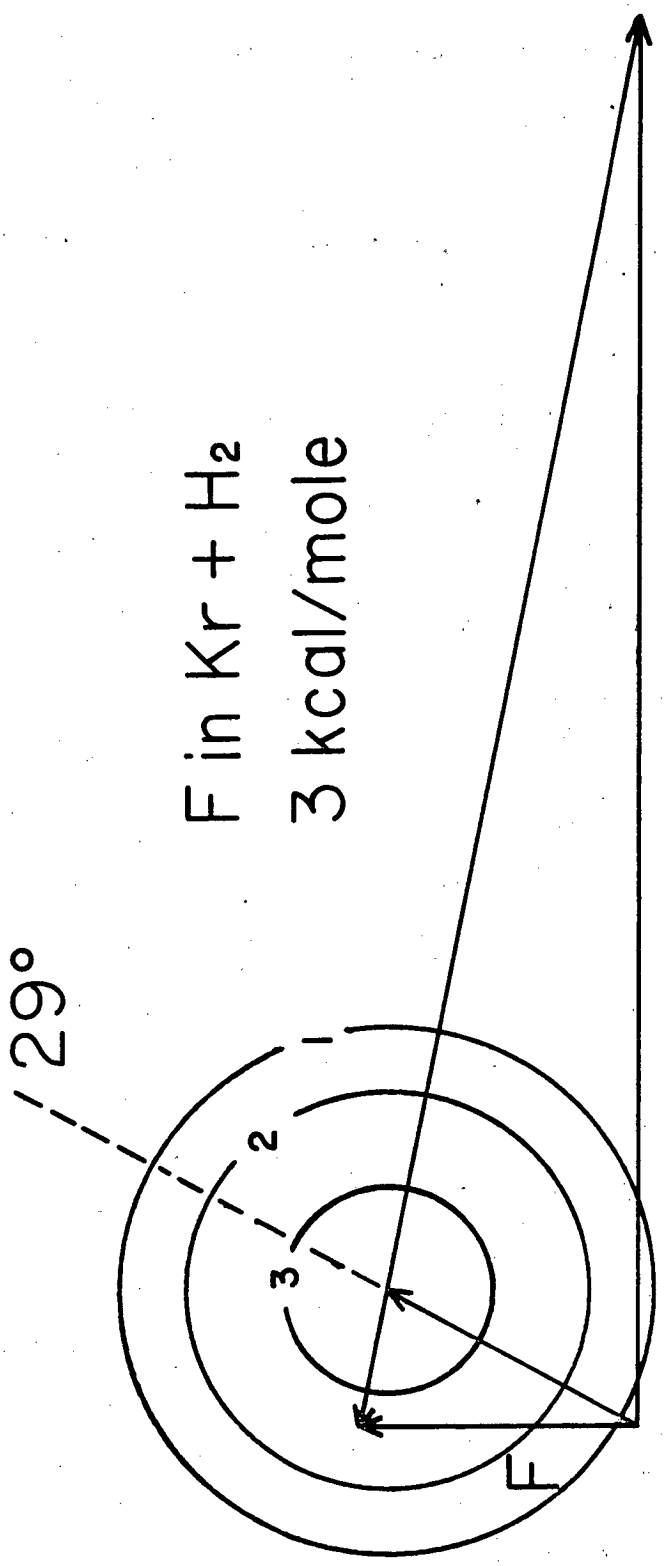

XBL 825-9943

Fig. 33.

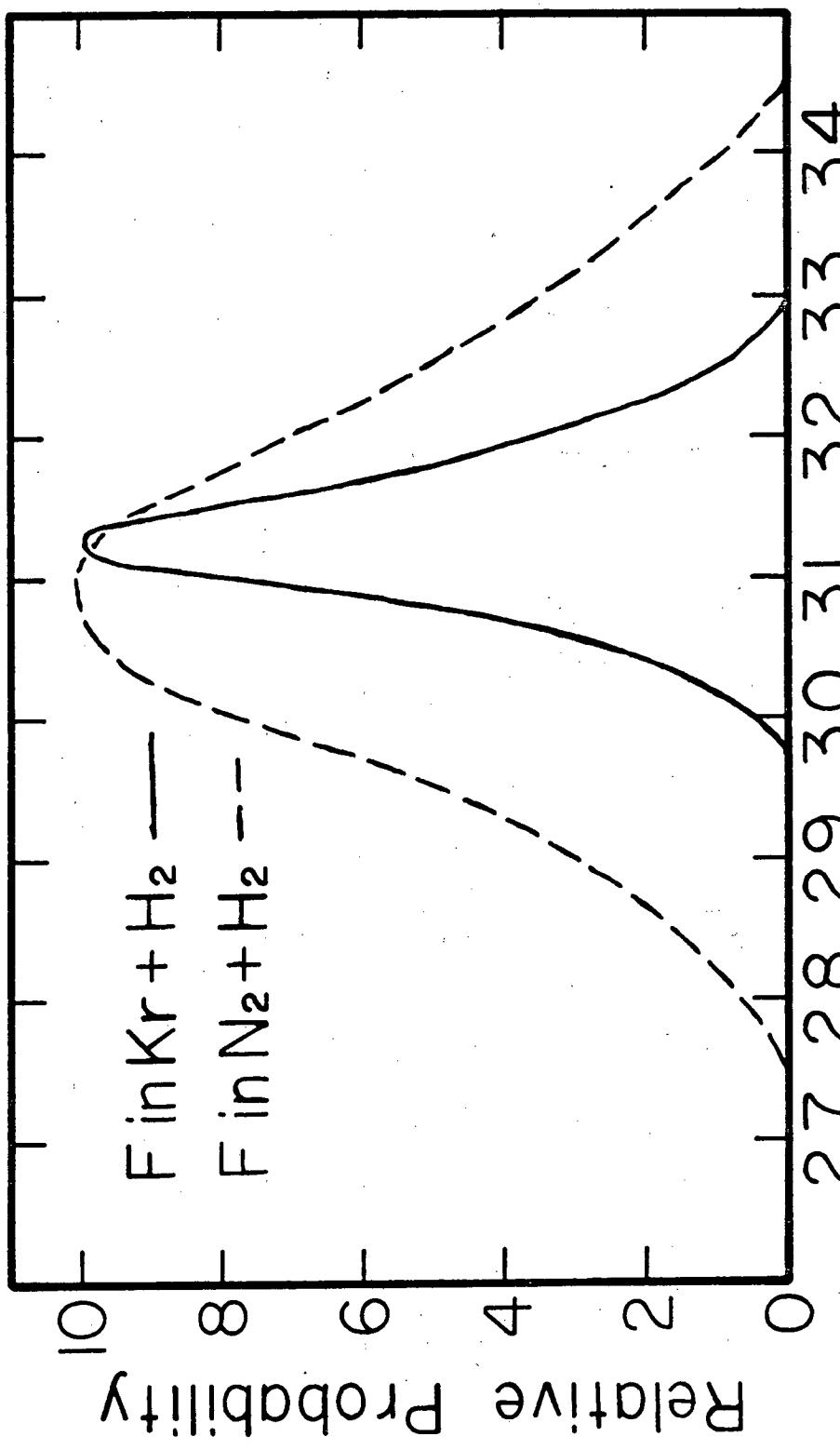

XBL 825-9944

Fig. 34.

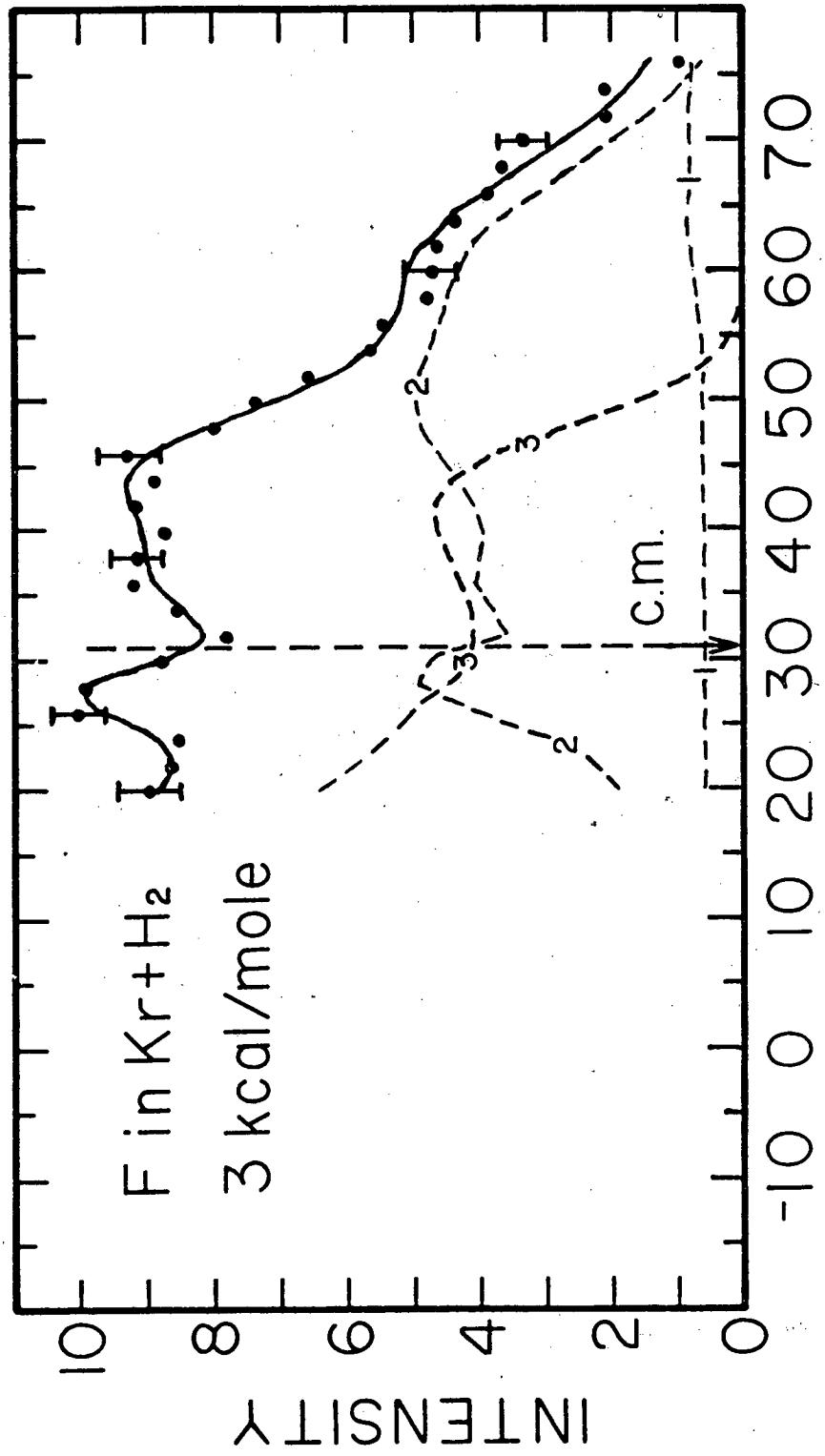

XBL 825-9896

Fig. 35.

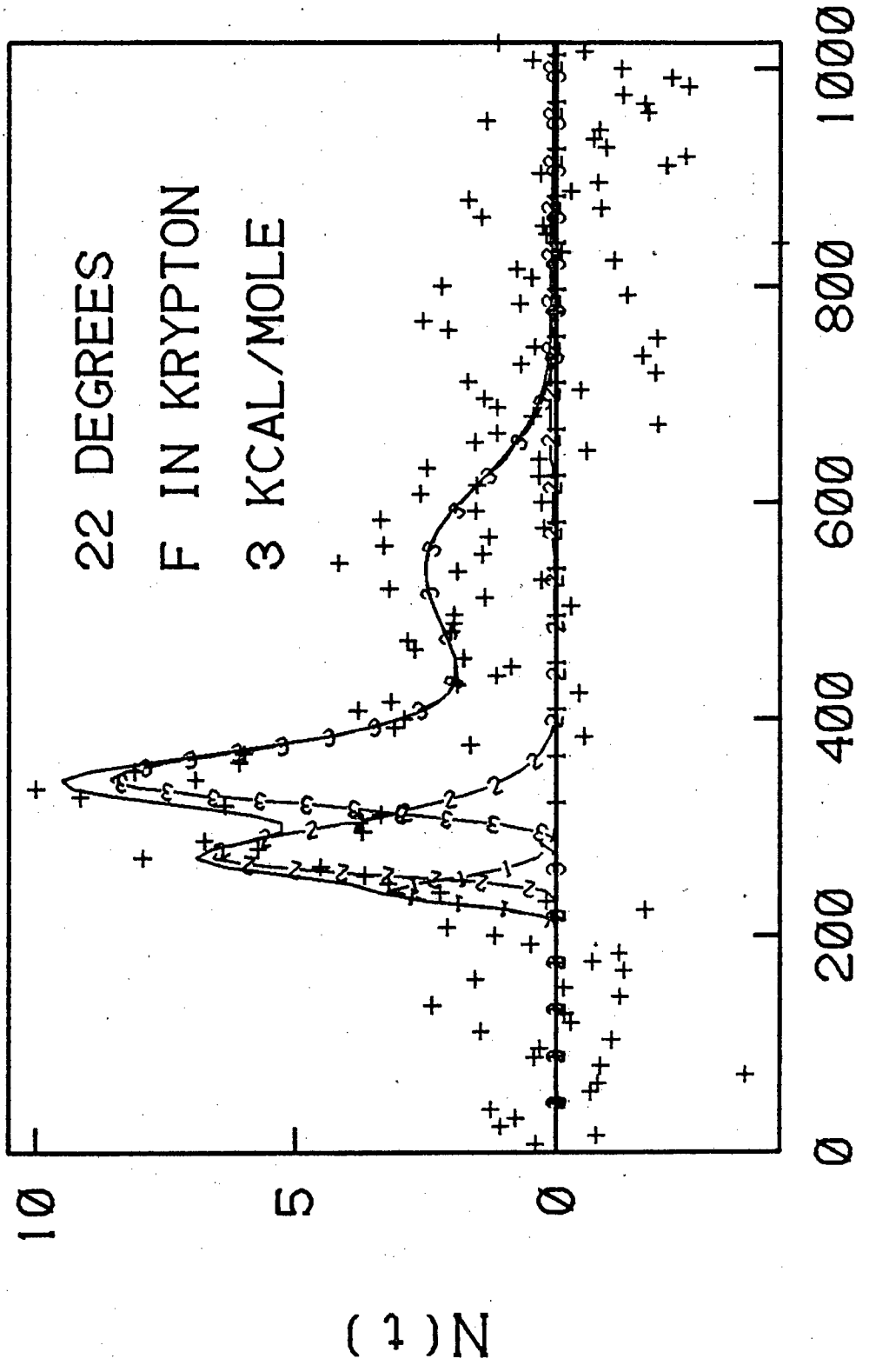

XBL 825-9904

Fig. 36.

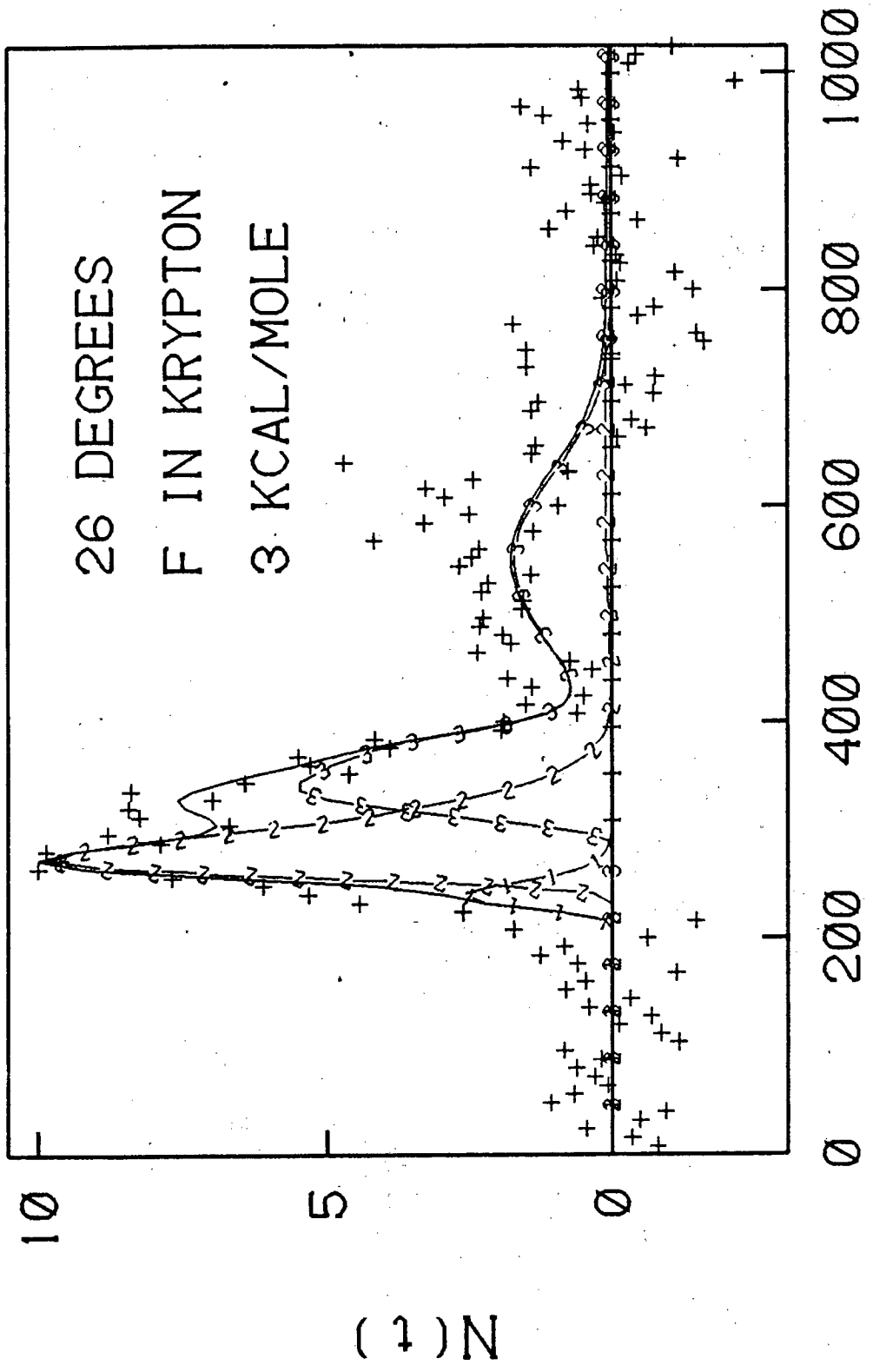

XBL 825-9905

Fig. 37.

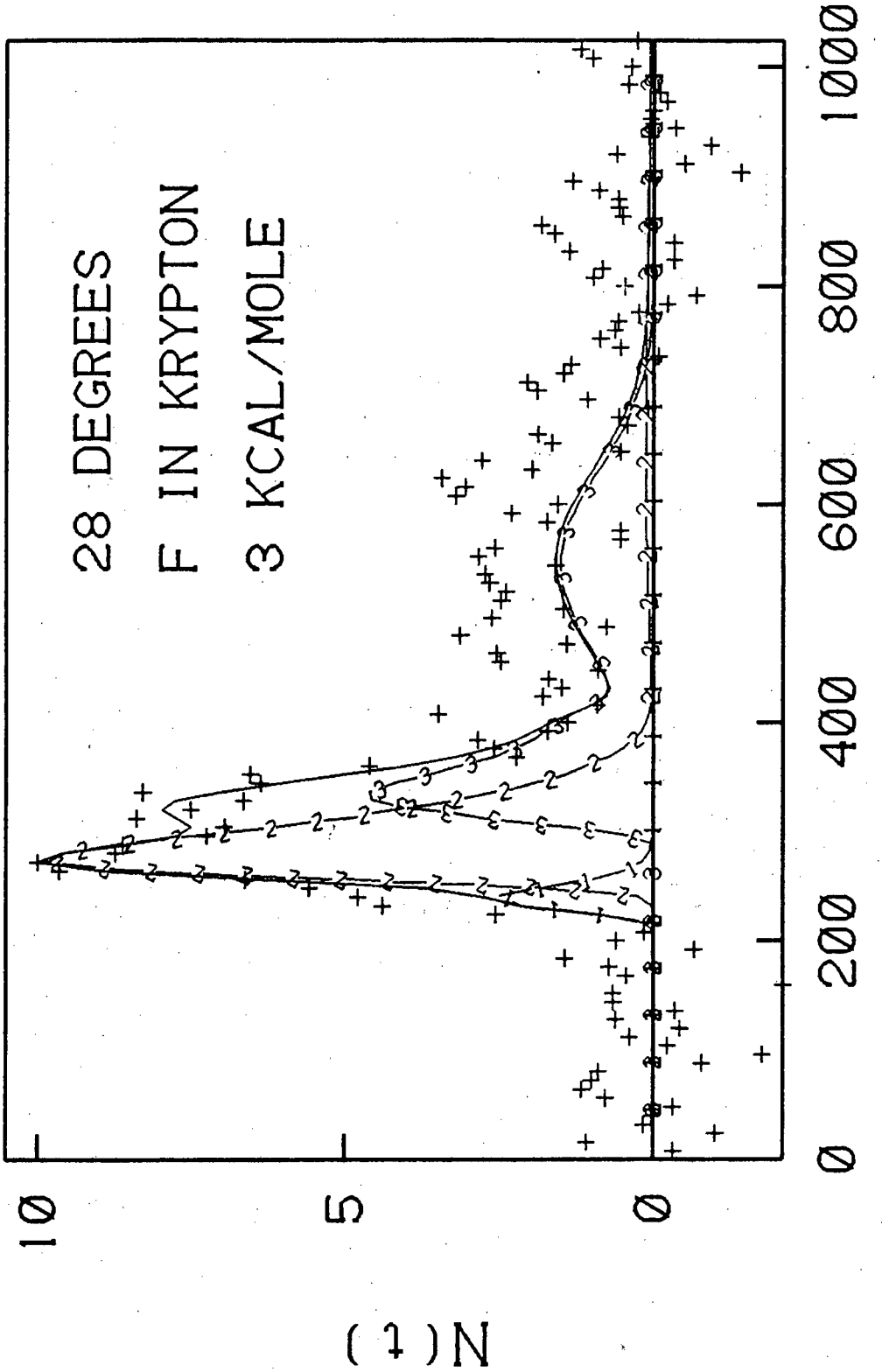

XBL 825-9906

Fig. 38.

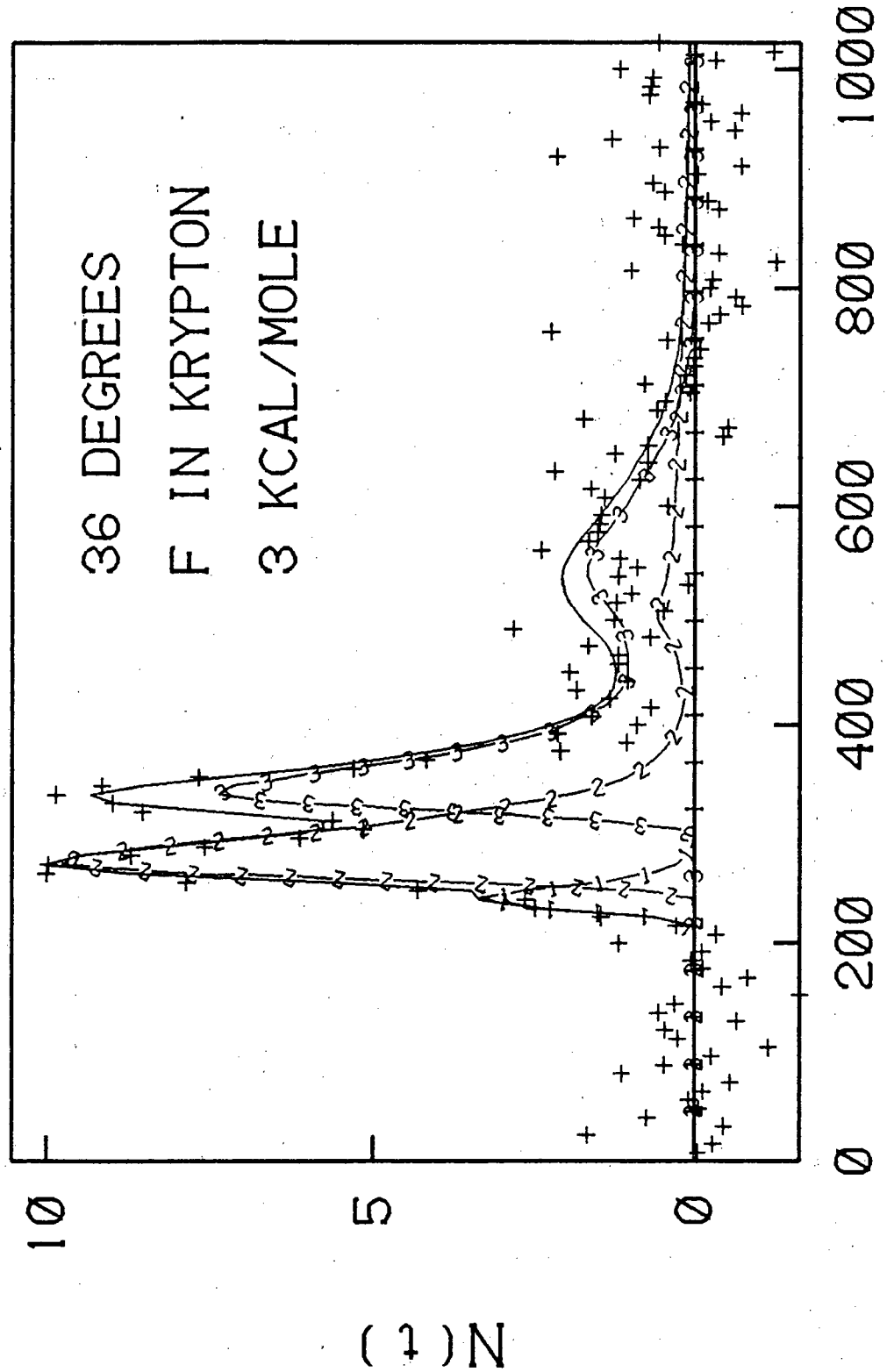

XBL 825-9907

Fig. 39.

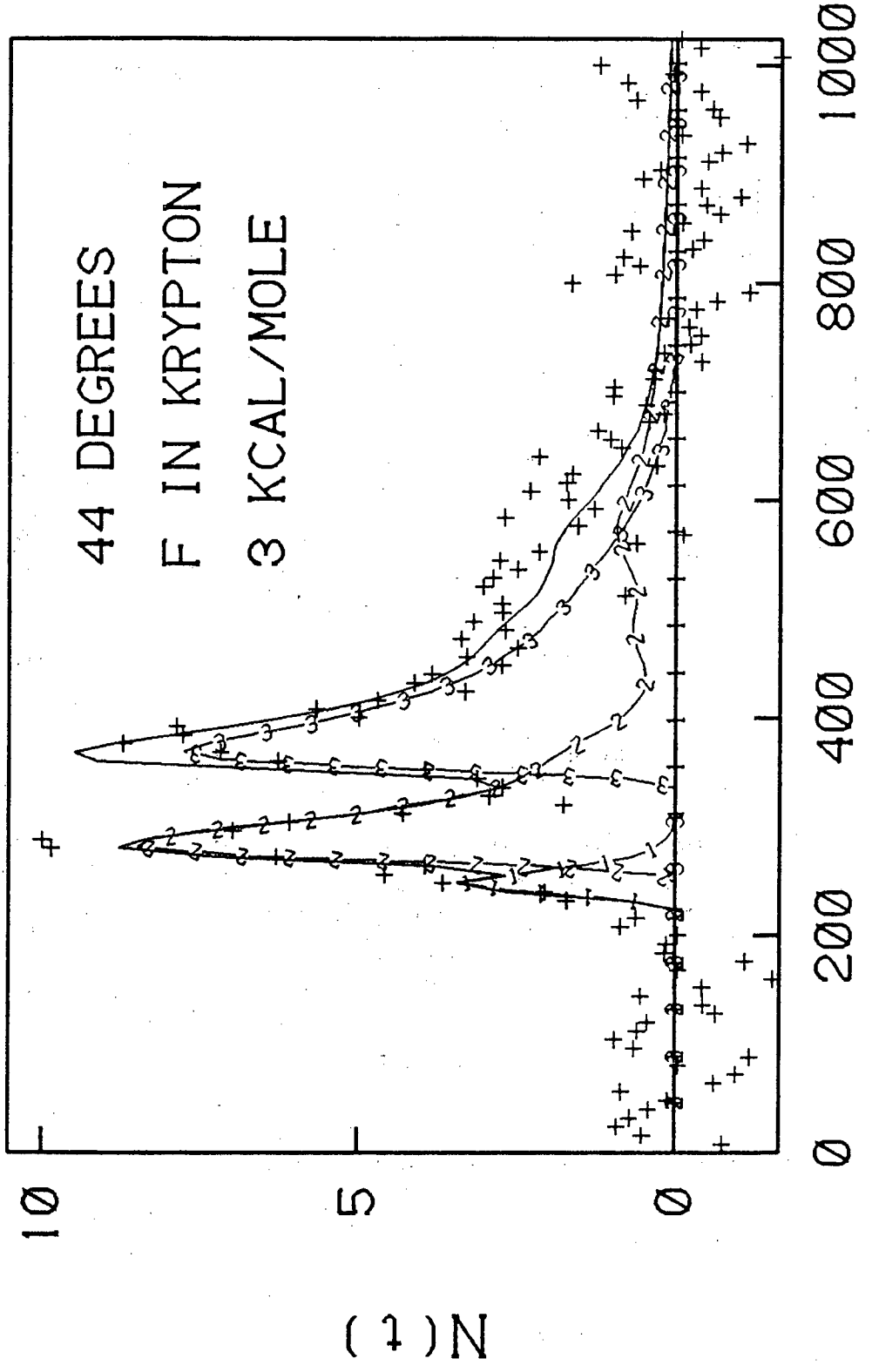

XBL 825-9908

Fig. 40.

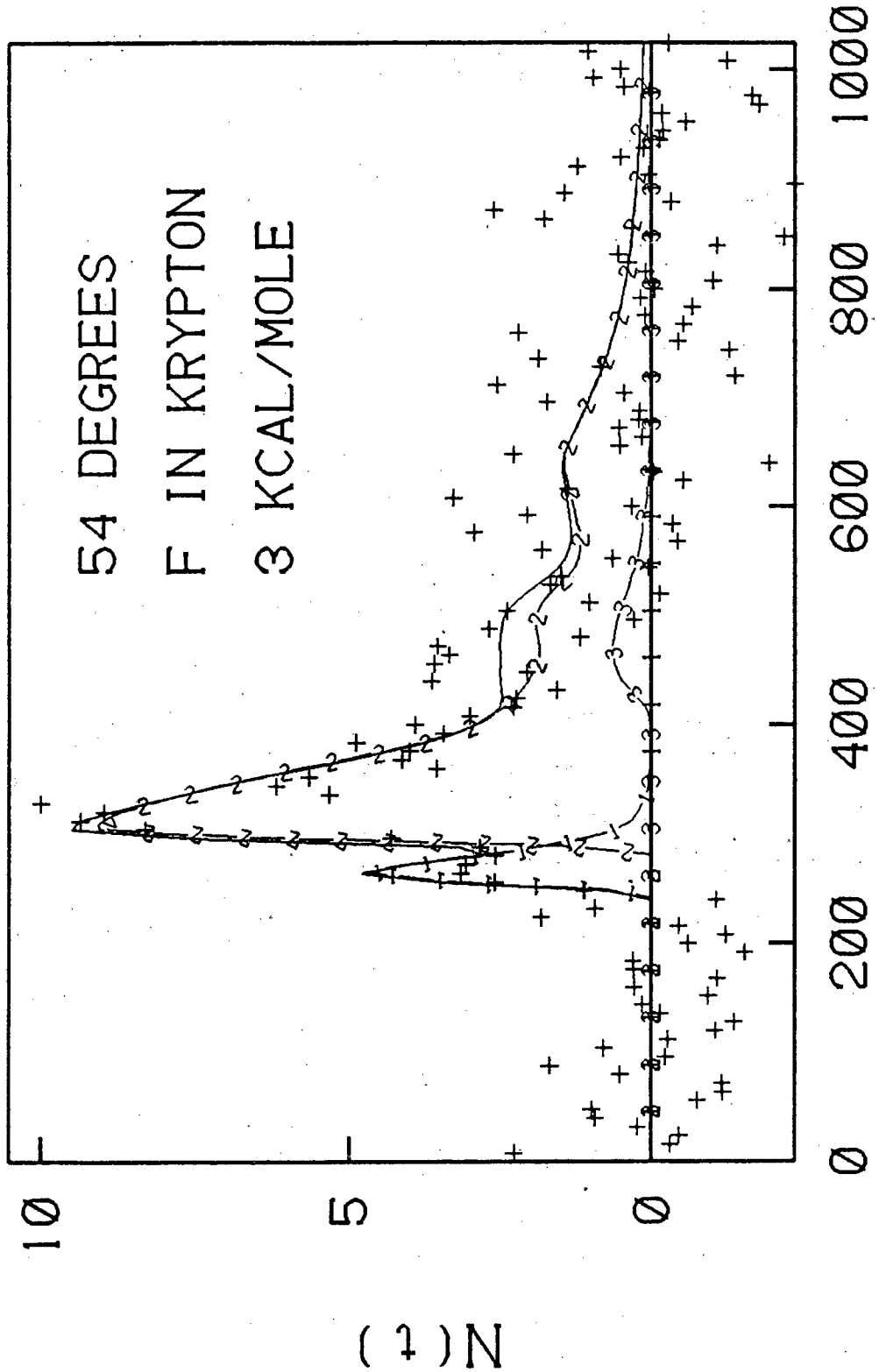

XBL 825-9909

Fig. 41.

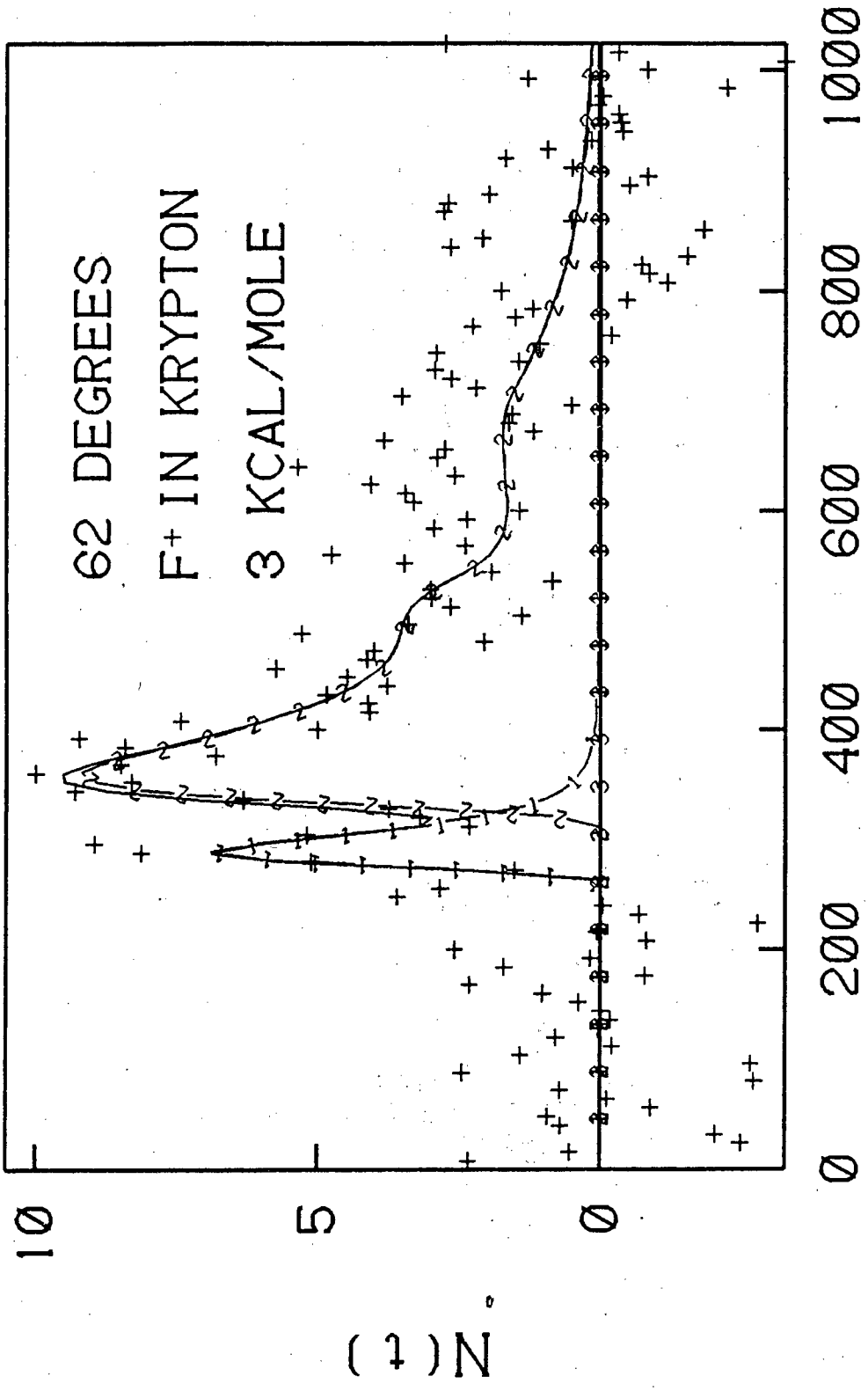

XBL 825-9910

Fig. 42.

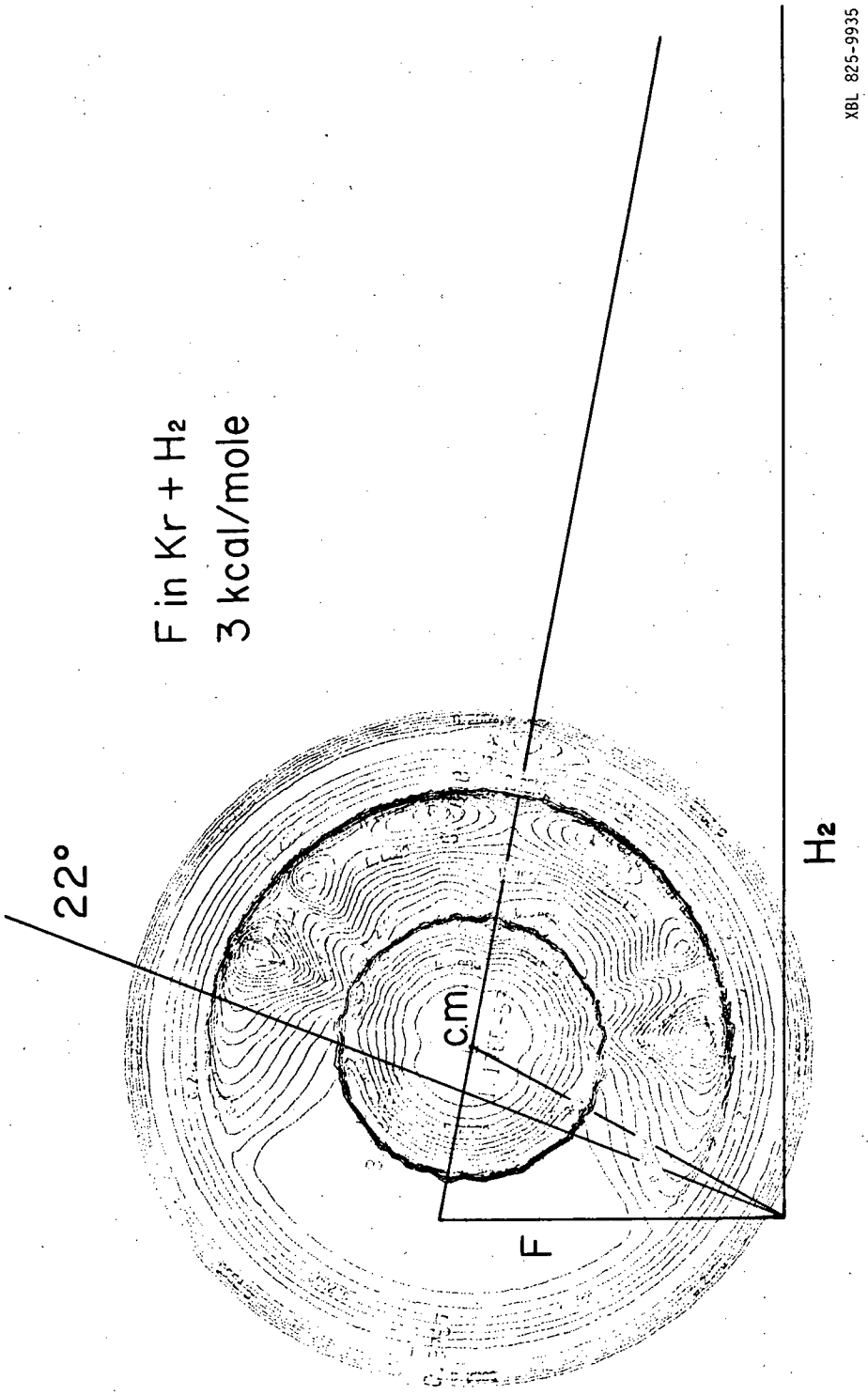

Fig. 43.

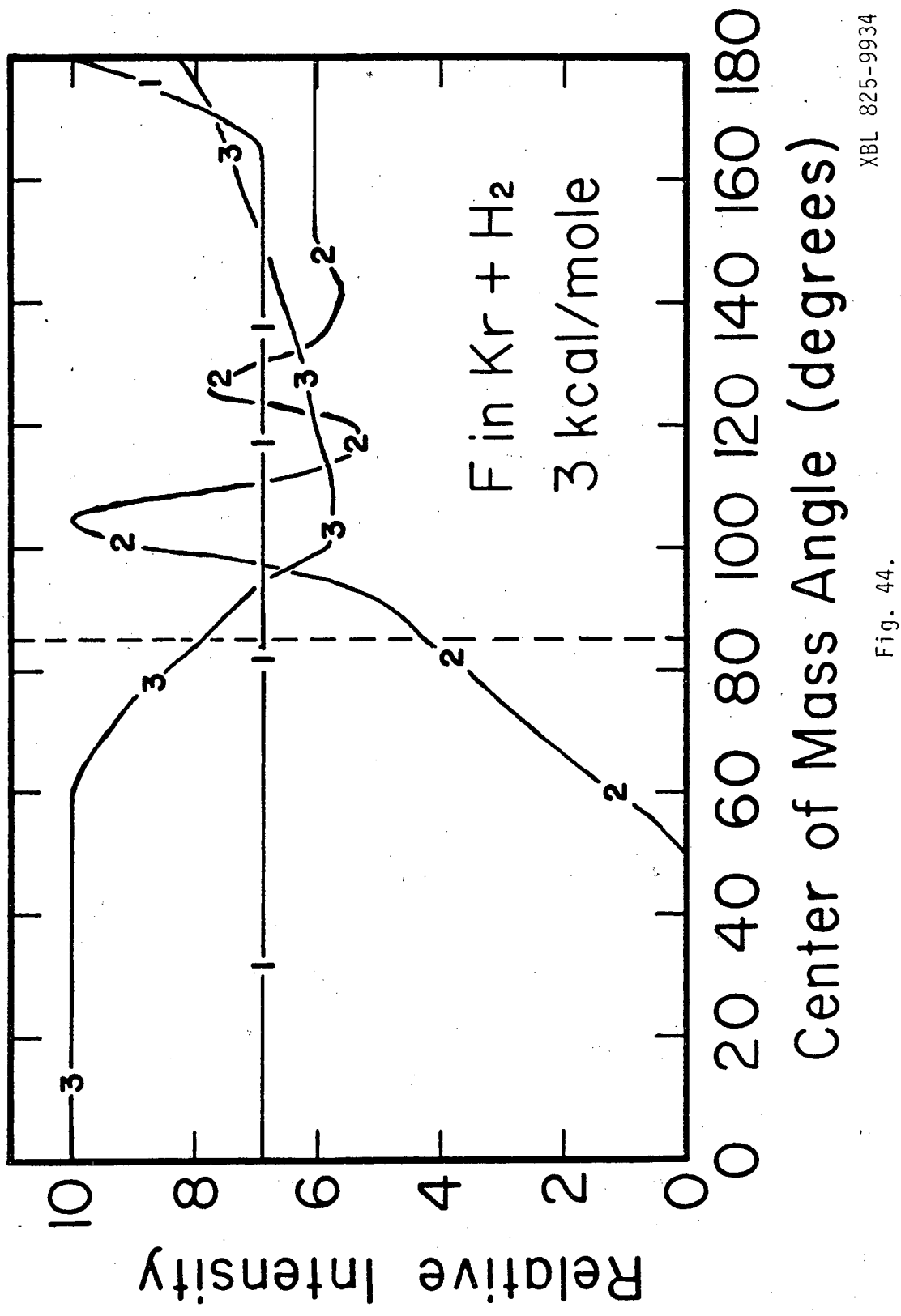

XBL 825-9934

Fig. 44.

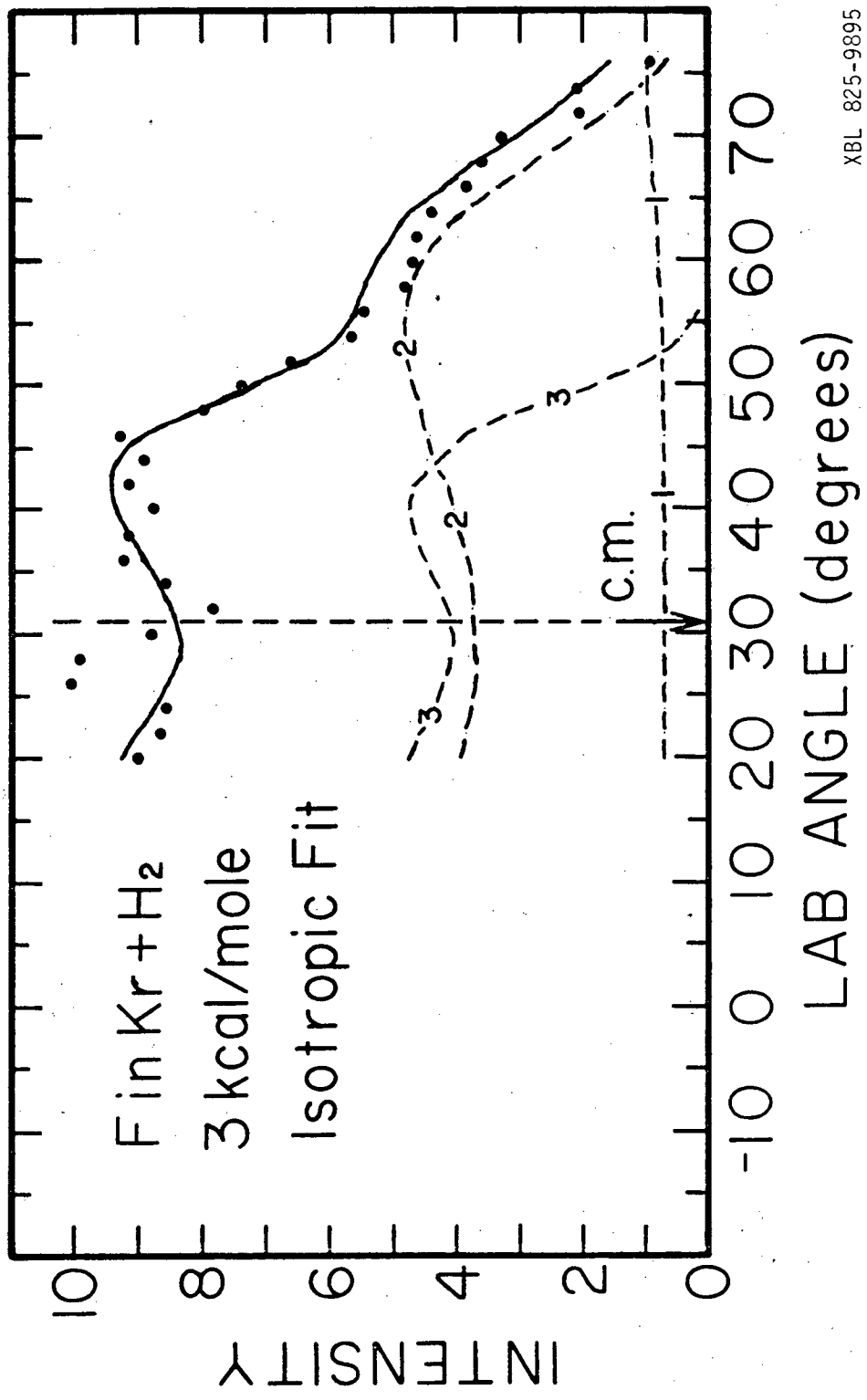

XBL 825-9895

Fig. 45.

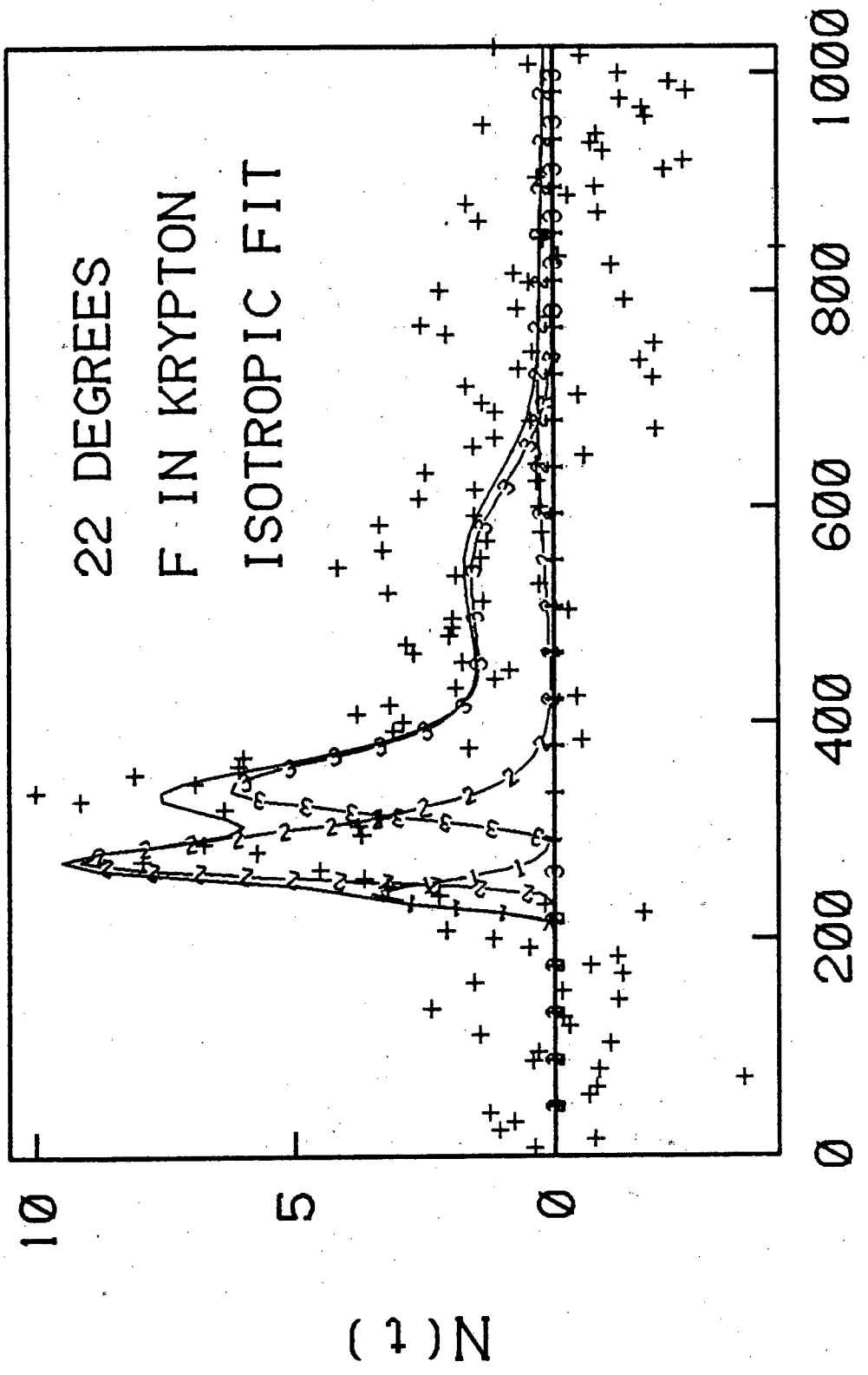

XBL 825-9897

Fig. 46.

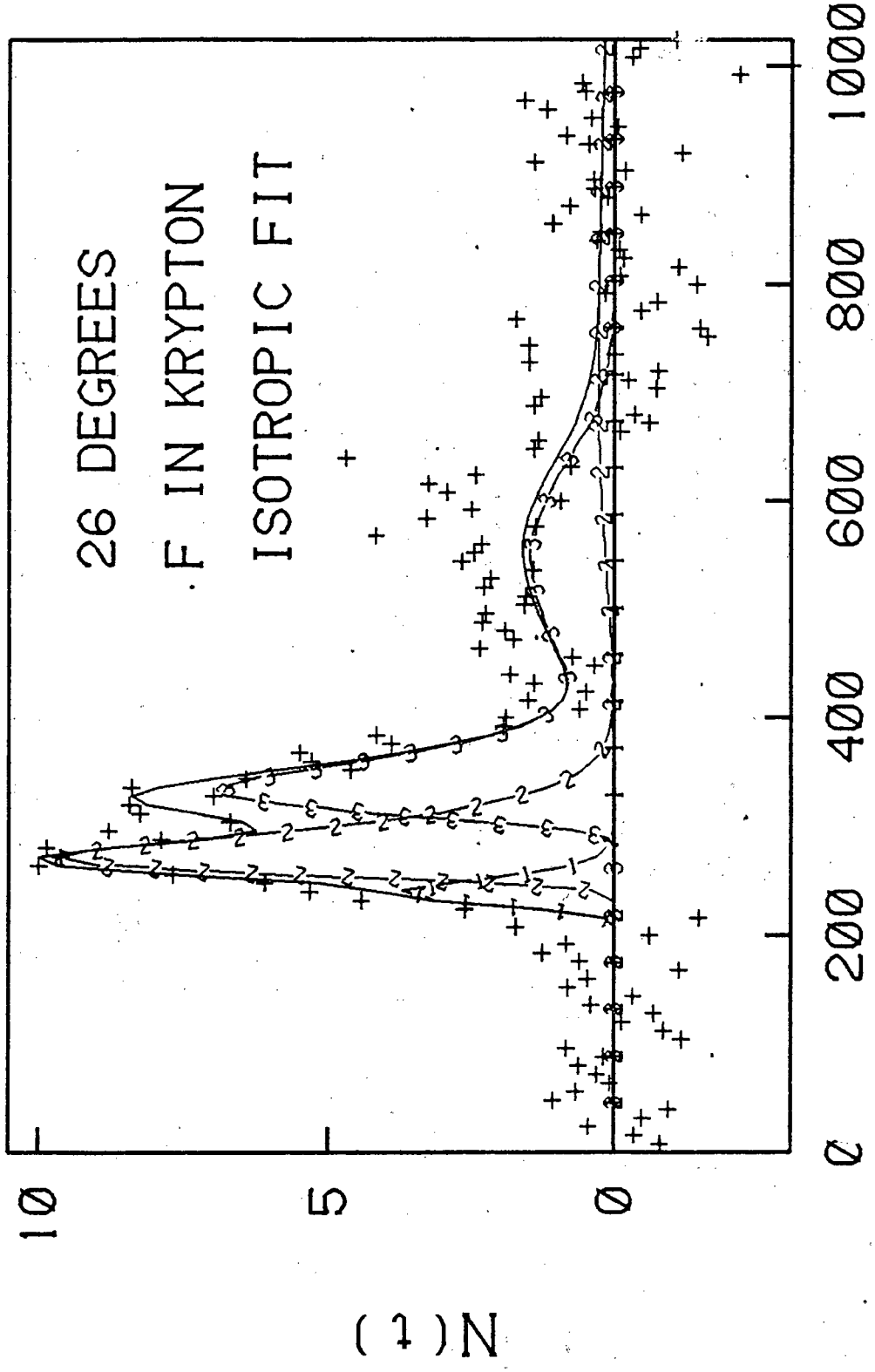

XBL 825-9898

Fig. 47.

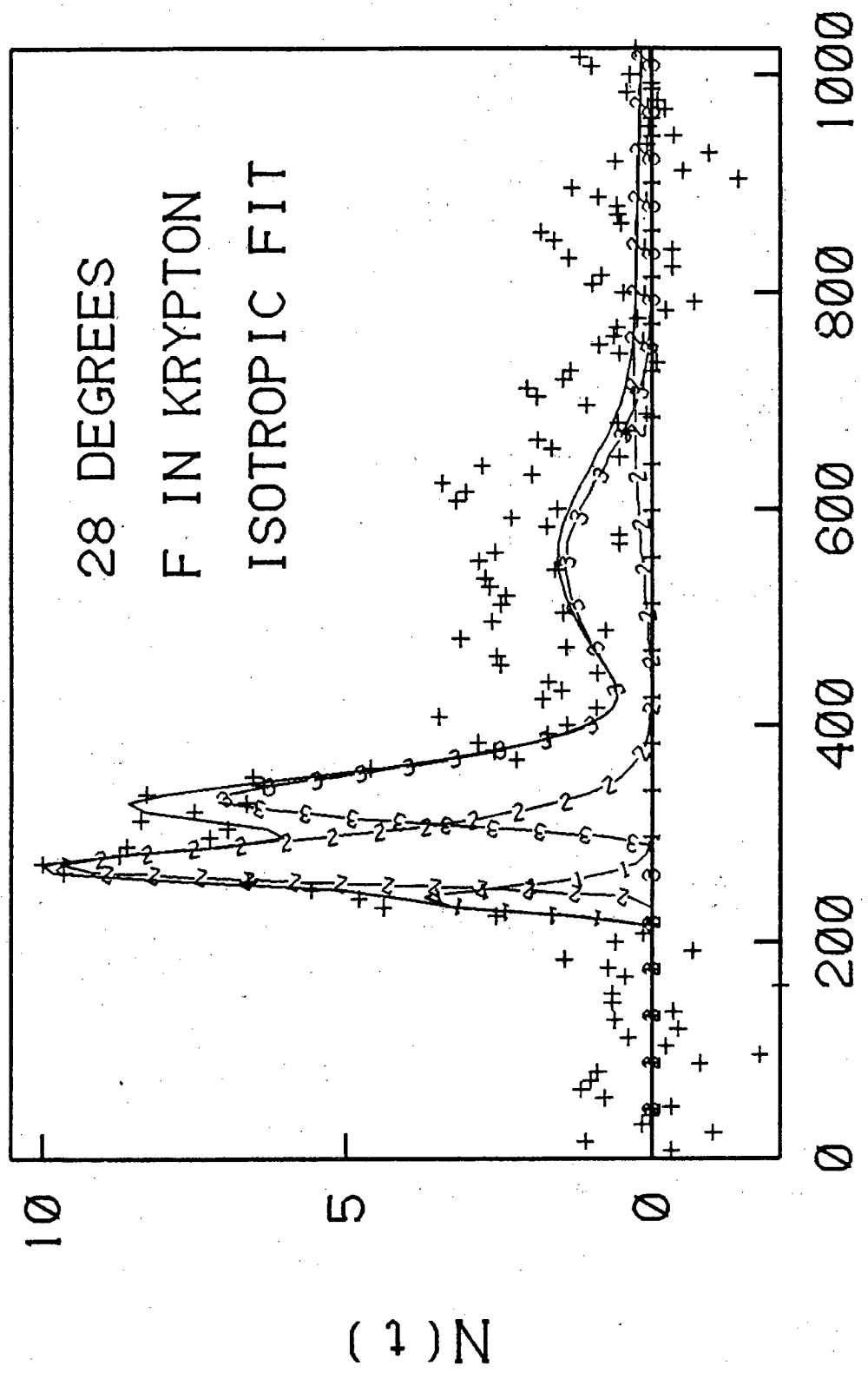

XBL 825-9899

Fig. 48.

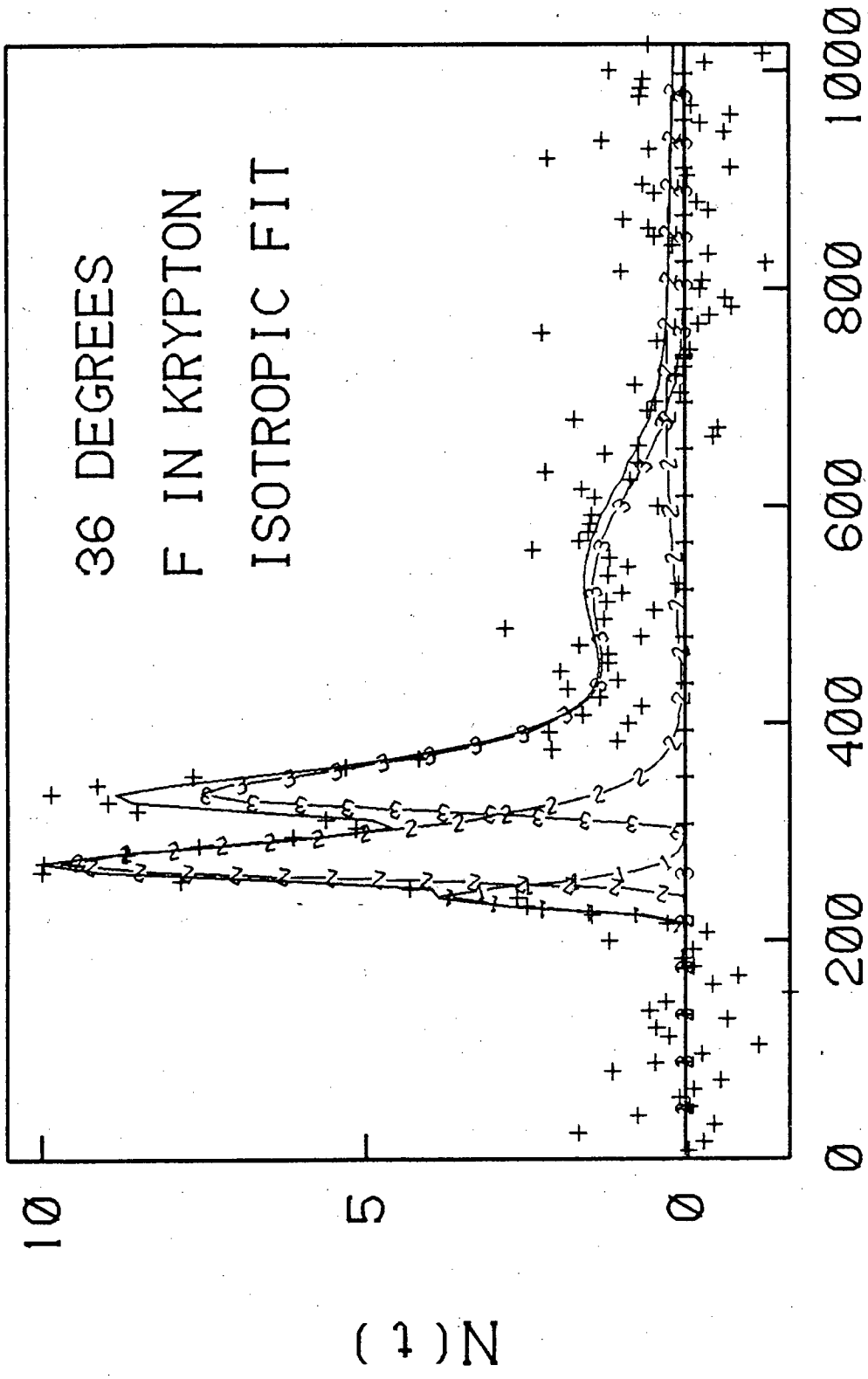

XBL 825-9900

Fig. 49.

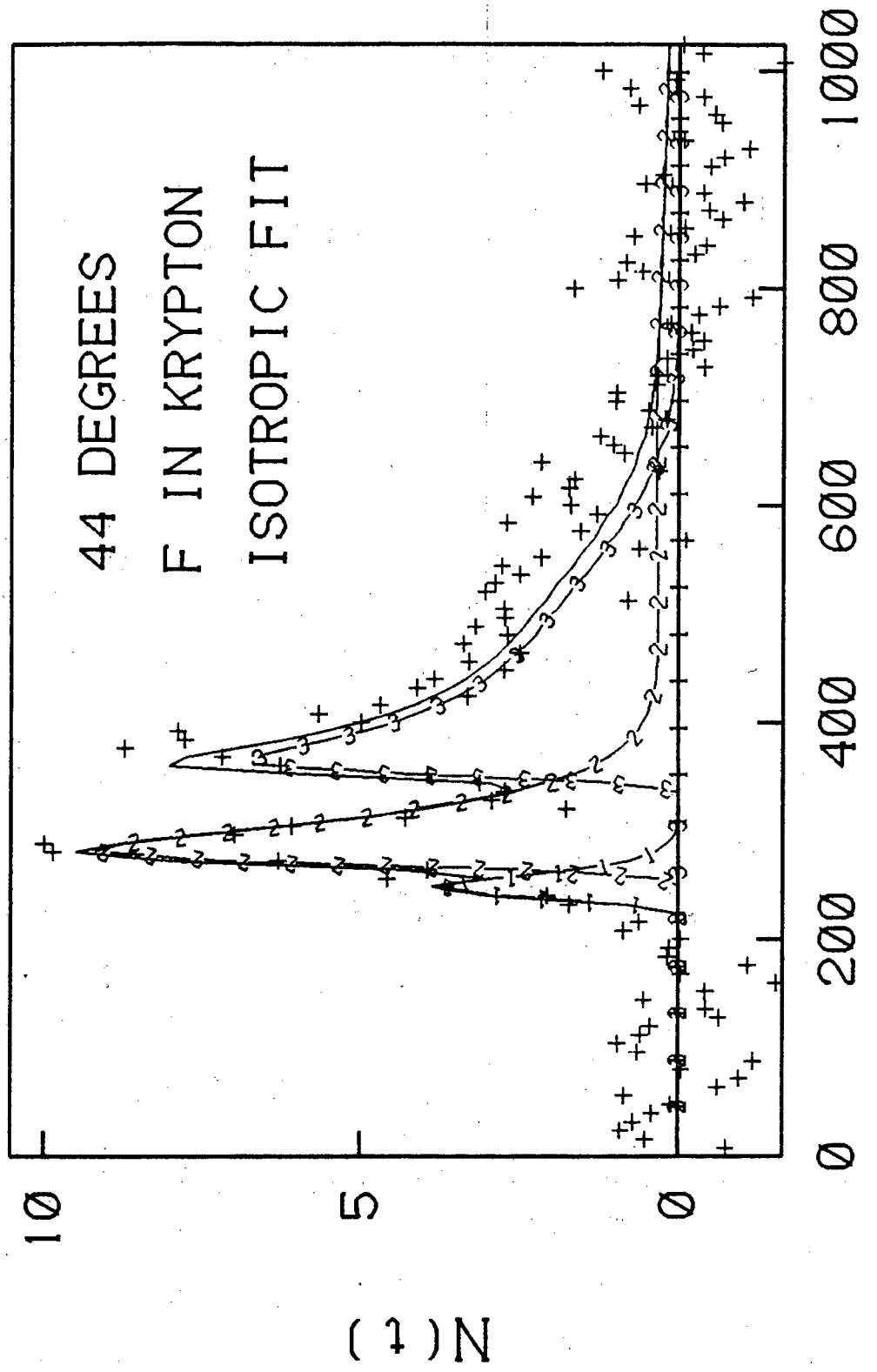

XBL 825-9901

Fig. 50.

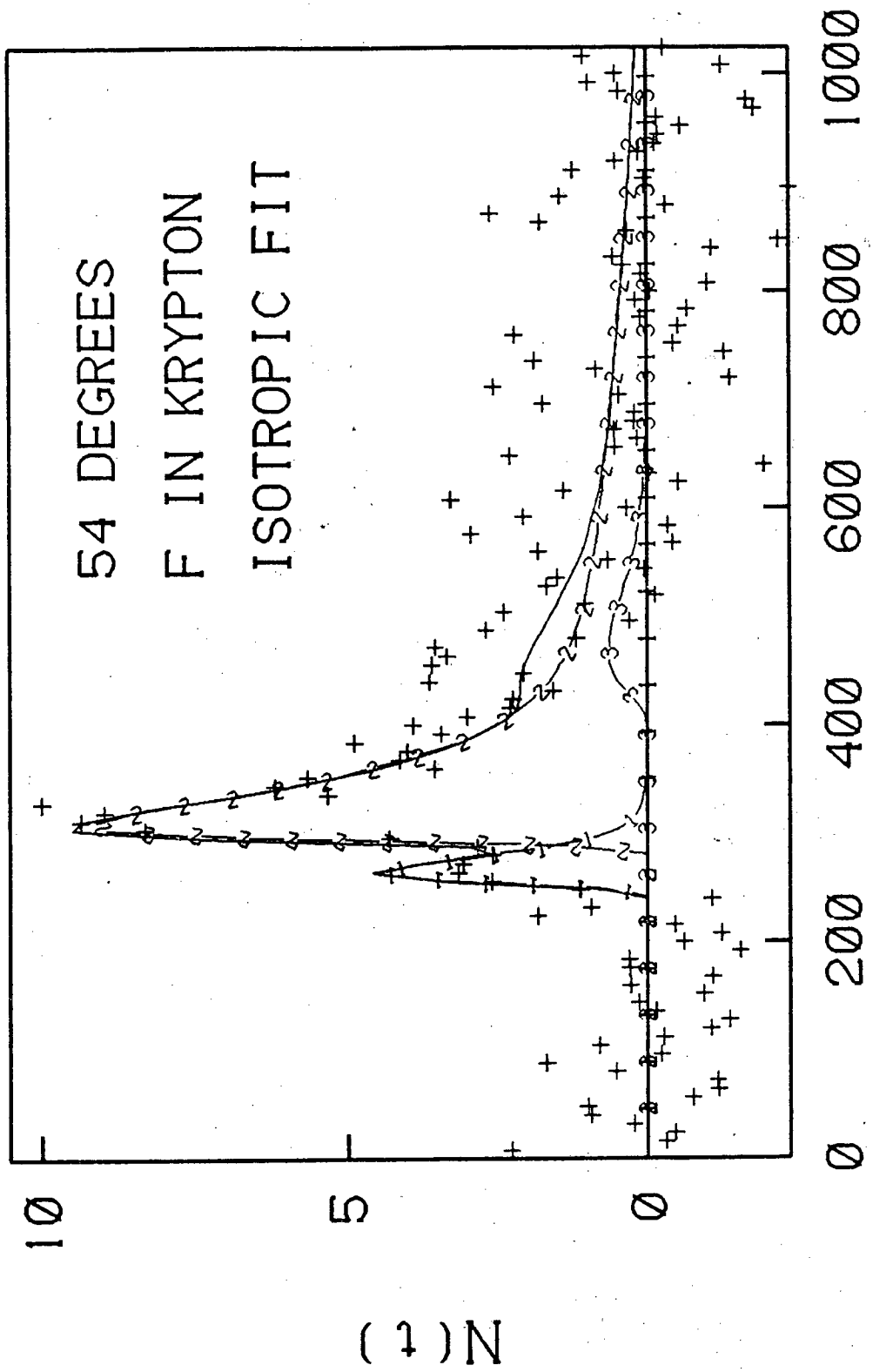

XBL 825-9902

Fig. 51.

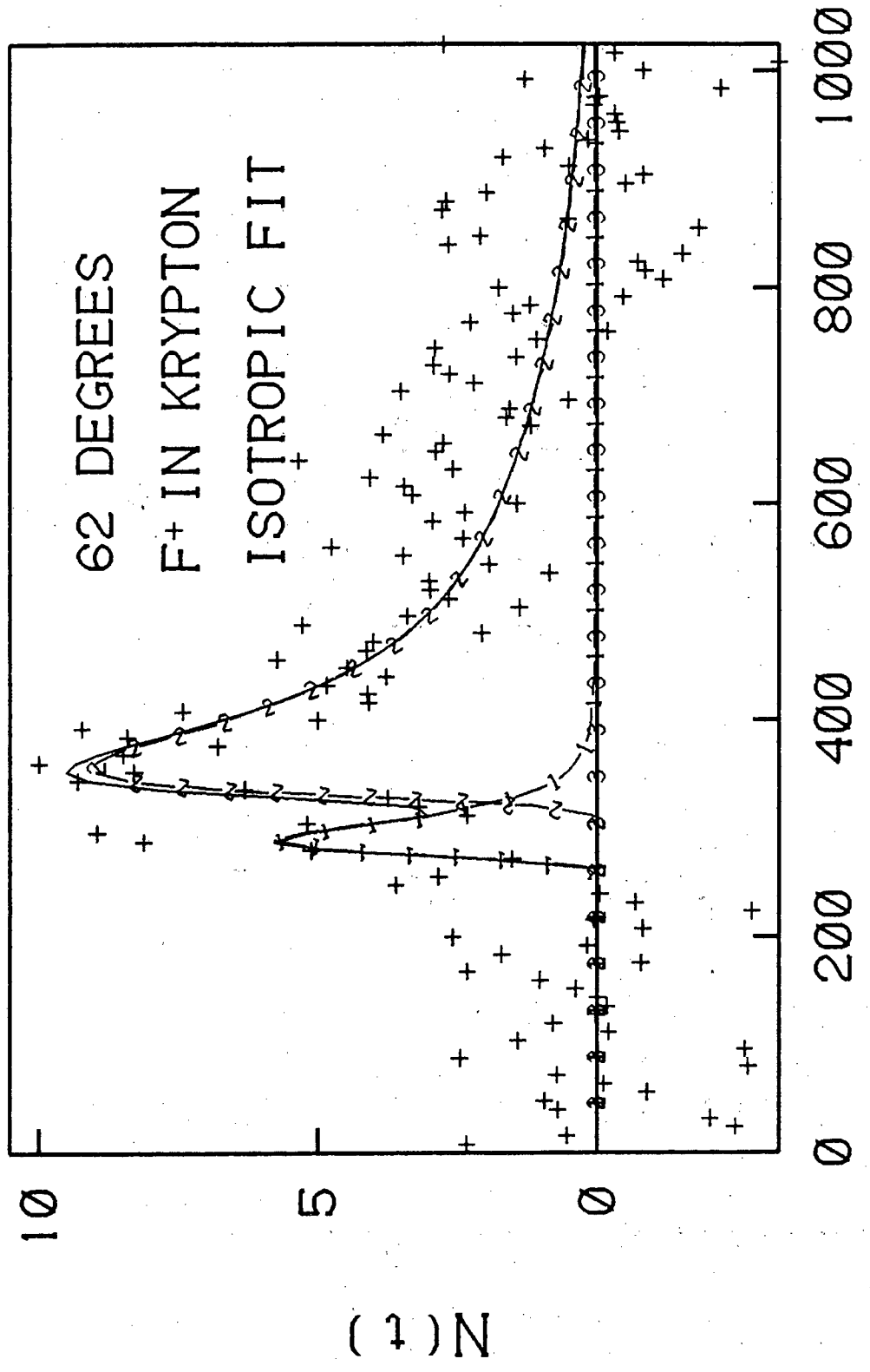

XBL 825-9903

Fig. 52.

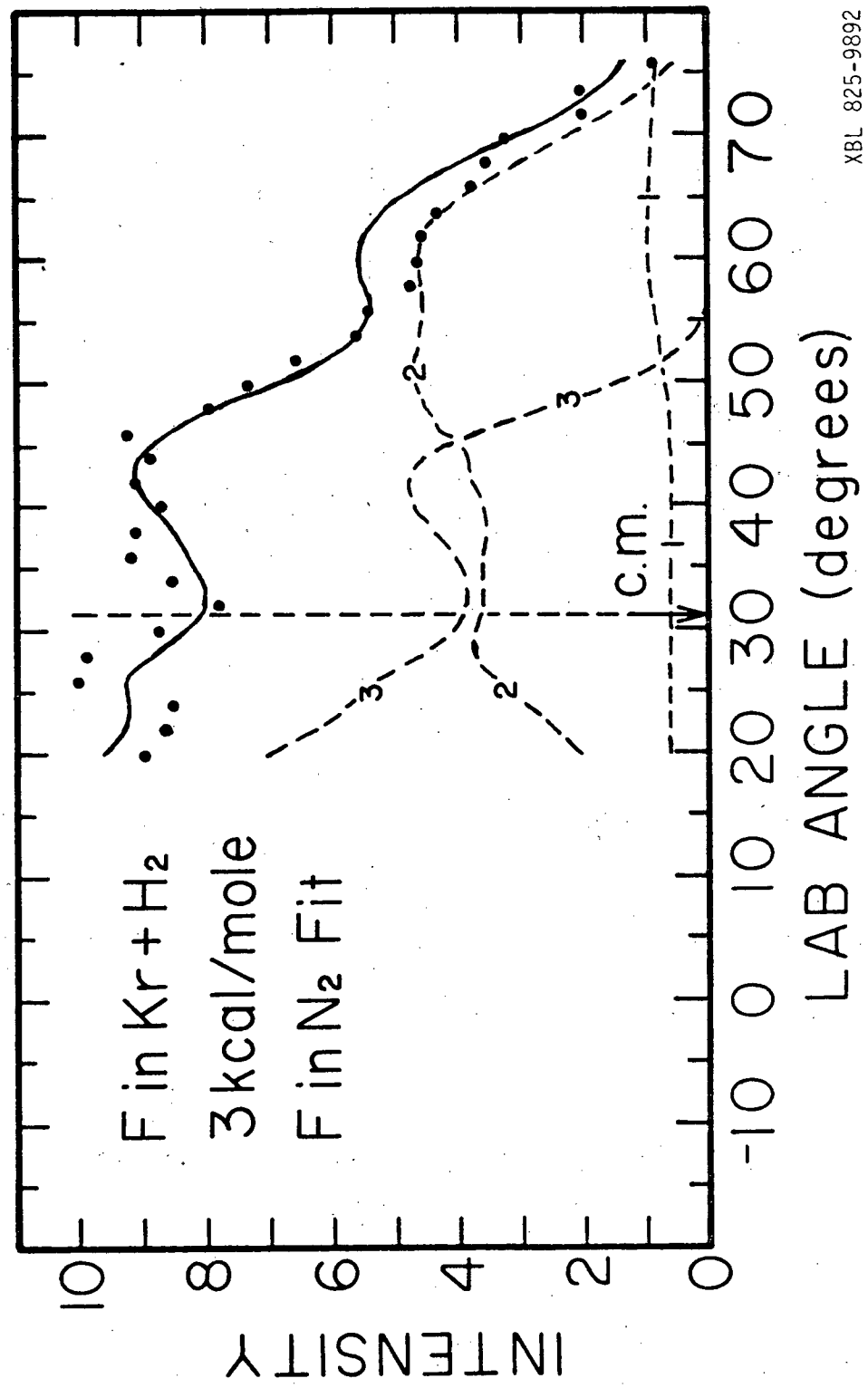

XBL 825-9892

Fig. 53.

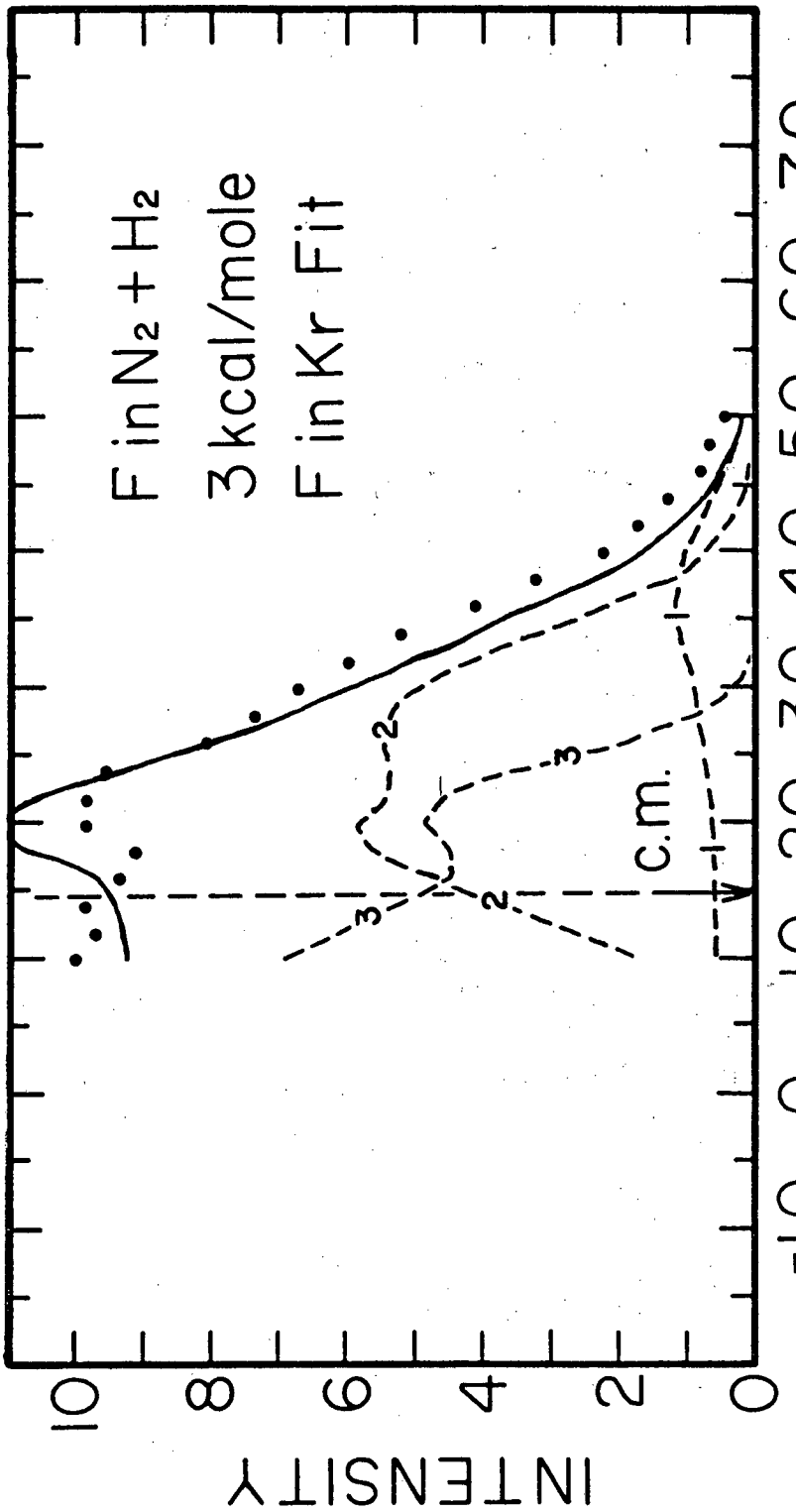

XBL 825-9891

Fig. 54.

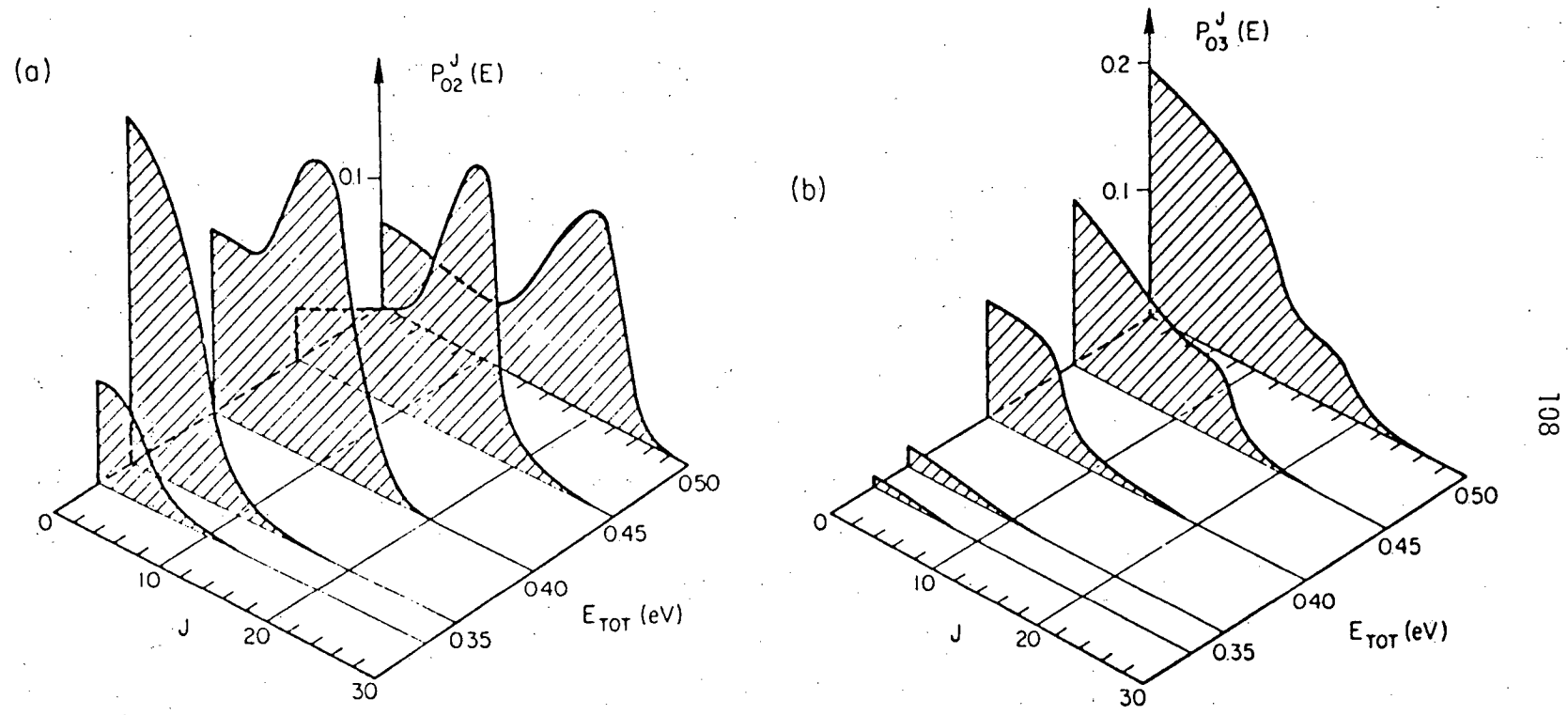

XBL 825-9890

Fig. 55.

APPENDIX

The values of the parameters used to specify the center-of-mass distributions are tabulated here. At each center-of-mass angle the energy distribution for each product vibrational state is given by

$$p(E) = E^{\alpha} (T_{max} - E)^{\beta}$$

where T_{max} is the maximum translational energy of the product. The actual input parameters are β and E_p, which is the energy of the peak of the probability distribution. The parameter α is given by

$$\alpha = \frac{\beta E_p}{T_{max} - E_p}$$

The area of the probability distribution is normalized, then the distribution is multiplied by an intensity factor for each center-of-mass angle. An overall factor also scales the relative intensities of the vibrational states. A value for the reaction exothermicity, including any internal energy of the reactants which can appear as translational energy of the products must also be chosen.

Parameters for the Best Fit to the Data from F in $N_2 + H_2$ at 2 kcal/mole

Exothermicity 32.5 kcal/mole

HF Vibrational State	β	Overall Intensity Scale Factor
1	2.0	0.3
2	0.45	0.8
3	0.55	0.25

C.M. Angle (degrees)	V = 1 Intensity	E_p	V = 2 Intensity	E_p	V = 3 Intensity	E_p
0 through 100	0.35	0.8	0.6	0.75	0.75	0.75
105	0.4	0.8	0.65	0.75	0.75	0.75
110	0.45	0.8	0.73	0.75	0.75	0.75
115	0.5	0.8	0.9	0.75	0.75	0.75
120	0.55	0.8	1.05	0.75	0.75	0.75
125	0.6	0.8	1.15	0.78	0.75	0.75
130	0.65	0.8	1.25	0.81	0.75	0.75
135	0.7	0.8	1.25	0.84	0.75	0.75
140	0.75	0.81	1.2	0.87	0.75	0.75
145	0.8	0.81	1.15	0.88	0.75	0.75
150	0.85	0.82	1.05	0.88	0.75	0.75
155	0.91	0.82	1.0	0.88	0.8	0.76
160	0.98	0.83	1.0	0.88	0.86	0.75
165	0.99	0.83	1.0	0.88	0.93	0.75
170	0.995	0.84	1.0	0.88	1.0	0.75
175	1.0	0.84	1.0	0.88	1.08	0.75
180	1.0	0.85	1.0	0.88	1.15	0.75

Parameters for the Best Fit to the Data from F in N_2 + H_2 at 3 kcal/mole

Exothermicity 33.0

HF Vibrational State	β	Overall Intensity Scale Factor
1	2.0	0.5
2	0.7	0.9
3	0.3	0.6

C.M. Angle (degrees)	V = 1 Intensity	E_p	V = 2 Intensity	E_p	V = 3 Intensity	E_p
0 through 50	1.0	0.8	0.0	0.75	0.9	0.85
55	1.0	0.8	0.1	0.75	0.9	0.85
60	1.0	0.8	0.3	0.75	0.9	0.85
65	1.0	0.8	0.45	0.75	0.87	0.85
70	1.0	0.8	0.6	0.75	0.85	0.83
75	1.0	0.8	0.75	0.75	0.8	0.8
80	1.0	0.8	0.85	0.745	0.75	0.77
85	1.0	0.8	1.05	0.74	0.7	0.76
90	1.0	0.8	1.2	0.735	0.65	0.77
95	1.0	0.8	1.35	0.73	0.6	0.81
100	1.0	0.8	1.55	0.725	0.52	0.83
105	1.0	0.8	1.65	0.72	0.46	0.85
110	1.0	0.8	1.65	0.725	0.43	0.85
115	1.0	0.8	1.5	0.73	0.4	0.85
120	1.0	0.8	1.6	0.74	0.4	0.85
125	1.0	0.8	1.7	0.76	0.4	0.85
130	1.0	0.8	1.7	0.78	0.43	0.85
135	1.0	0.8	1.63	0.81	0.43	0.85
140	1.0	0.8	1.55	0.83	0.44	0.85
145	1.0	0.8	1.5	0.83	0.49	0.85
150	1.0	0.8	1.5	0.83	0.54	0.85
155	1.1	0.8	1.5	0.83	0.57	0.85
160	1.2	0.8	1.5	0.83	0.6	0.85
165	1.3	0.8	1.5	0.83	0.62	0.85
170	1.4	0.8	1.5	0.8	0.64	0.85
175	1.5	0.8	1.5	0.76	0.66	0.85
180	1.6	0.8	1.5	0.72	0.68	0.85

Parameters for the Best Fit to the Data from F in $Kr + H_2$ at 3 kcal/mole

Exothermicity 33.0

HF Vibrational State	β	Overall Intensity Scale Factor
1	2.0	0.5
2	0.5	0.9
3	0.25	0.55

C.M. Angle (degrees)	V = 1 Intensity	E_p	V = 2 Intensity	E_p	V = 3 Intensity	E_p
0 through 50	1.0	0.8	0.0	0.75	0.9	0.85
55	1.0	0.8	0.1	0.75	0.9	0.85
60	1.0	0.8	0.3	0.75	0.9	0.85
65	1.0	0.8	0.45	0.75	0.87	0.85
70	1.0	0.8	0.6	0.75	0.85	0.83
75	1.0	0.8	0.75	0.75	0.82	0.8
80	1.0	0.8	0.85	0.745	0.75	0.77
85	1.0	0.8	1.05	0.74	0.7	0.76
90	1.0	0.8	1.15	0.735	0.66	0.77
95	1.0	0.8	1.45	0.73	0.62	0.81
100	1.0	0.8	2.1	0.725	0.52	0.83
105	1.0	0.8	2.45	0.72	0.52	0.85
110	1.0	0.8	1.8	0.725	0.52	0.85
115	1.0	0.8	1.35	0.73	0.53	0.85
120	1.0	0.8	1.3	0.735	0.54	0.85
125	1.0	0.8	1.9	0.74	0.55	0.85
130	1.0	0.8	1.7	0.75	0.56	0.85
135	1.0	0.8	1.45	0.76	0.575	0.85
140	1.0	0.8	1.4	0.77	0.59	0.85
145	1.0	0.8	1.4	0.78	0.605	0.85
150	1.0	0.8	1.5	0.79	0.62	0.85
155	1.0	0.8	1.5	0.8	0.635	0.85
160	1.0	0.8	1.5	0.82	0.65	0.85
165	1.0	0.8	1.5	0.8	0.67	0.85
170	1.1	0.8	1.5	0.77	0.69	0.85
175	1.25	0.8	1.5	0.73	0.715	0.85
180	1.45	0.8	1.5	0.69	0.74	0.85

Parameters for the Best Fit to the Data from F in $Kr + H_2$ at 3.0 kcal/mole

Exothermicity 33.0 kcal/mole

HF Vibrational State	β	Overall Intensity Scale Factor
1	2.0	0.5
2	0.5	1.0
3	0.06	0.6

C.M. Angle (degrees)	V = 1 Intensity	E_p	V = 2 Intensity	E_p	V = 3 Intensity	E_p
0 through 180	1.0	0.8	1.2	0.8	0.5	0.95

II. DETERMINATION OF METHYLENE SINGLET-TRIPLET SPLITTING FROM MOLECULAR BEAM PHOTODISSOCIATIN OF KETENE

INTRODUCTION

The unique chemistry of the methylene radical, CH_2, is primarily due to the substantially different chemical behavior of two low lying electronic states, the ground ($^3B_1$) state and the lowest excited ($^1A_1$) state. The photochemical processes commonly used to produce CH_2 can yield both states, and the nature of subsequent reactions depends on whether triplet or singlet methylene is involved. In spite of a large number of experimental and theoretical studies, questions about the energies of these states still remain.

Several different experimental approaches have been used to obtain information on these energies. Most of the results are consistent with a singlet-triplet splitting of about 8.5 ± 1 kcal/mole, but the most direct measurement, the photoelectron spectrum of photodetachment from CH_2^-, gives 19.5 kcal/mole.[1] In addition, the best calculations show the energy difference to be around 10.5 kcal/mole, supporting the lower experimental value. The molecular beam photofragmentation translational spectroscopy on ketene described in this chapter provides another microscopic experiment which eliminates many of the problems associated with other methods, and thus should help resolve the differences among the experimental results.

Measurements of the temperature and pressure dependence of product ratios from CH_2 ($^1A_1$) and CH_2 ($^3B_1$) reactions have been used to estimate the singlet-triplet energy difference assuming that collision induced transitions

$$CH_2\ (^3B_1) + M \rightleftharpoons CH_2\ (^1A_1) + M$$

maintain equilibrium concentrations of the two species. Values of 7.5 ± 0.7 kcal/mole[2] and 8.7 ± 0.8 kcal/mole[3] were then obtained. To determine the heat of formation of CH_2 ($^3B_1$), the threshold for production of CH_2^+ from dissociative photoionization has been measured using several different precursors. From known enthalpies of formation for the dissociating molecules, and the ionization potential of CH_2, an upper limit has been placed on $\Delta H^o_{fo}\ CH_2(^3B_1)$. This will be the correct value if no excess energy is released in the dissociative photoionization at threshold. The enthalpy of formation of methylene ($^3B_1$) from this procedure ranges from 91.9 to 95.5 kcal/mole with the best values being 93.8 ± 0.4 and 93.4 ± 0.4 kcal/mole from photoionization of methane and ketene respectively[4] and 94.6 ± 0.5 kcal/mole from methane.[5] The spread in these numbers can be accounted for by the difficulty in determining the thresholds and estimating the contributions of internal energy to the process. Recent work has also placed an upper limit on $\Delta H^o_{fo}\ CH_2\ (^1A_1)$. The internal excitation of methylene ($^1A_1$) produced from photodissociation of ketene with a nitrogen laser was determined by laser induced fluorescence. The temperature dependence of the fluorescence intensity from CH_2 was measured to estimate the amount of internal excitation that must be present in ketene for dissociation to occur at the nitrogen laser wavelength (337.1 nm). Then from the heats of formation of CH_2CO and CO, $\Delta H^o_{fo}\ CH_2\ (^1A_1)$ has been calculated, with the result[6]

$$\Delta H^o_{fo}\ CH_2(^1A_1) = 101.7 \pm 0.5 \text{ kcal/mole.}$$

This upper limit should be close to the correct value if the internal energy in the CO fragment and the kinetic energy release are negligible.

In similar experiments the threshold for CH_2 ($^1A_1$) production from ketene was measured by monitoring methylene laser induced fluorescence as a function of photolysis laser wavelength. Independent determinations of the threshold gave 85.0 ± 0.3 kcal/mole[6] and 85.4 ± 0.3 kcal/mole[7] corresponding to

$$\Delta H^o_{fo}\ CH_2\ (^1A_1) = 101.5 \pm 0.5 \text{ kcal/mole}$$

and

$$101.9 \pm 0.5 \text{ kcal/mole}$$

respectively.

The wavelength threshold for ketene photolysis at 298K yielding CH_2 ($^3B_1$) and CO has also been determined from the appearance of CO product.[8] In the same experiment the threshold for ketene photolysis to give CH_2 ($^1A_1$) was measured by detecting products of the singlet reacting with cis-2-butene. Thus enthalpies for the reactions

$$CH_2CO \xrightarrow{h\nu} CH_2\ (^3B_1) + CO$$

$$CH_2CO \xrightarrow{h\nu} CH_2\ (^1A_1) + CO$$

were determined at 298°K. The difference in the threshold energies then gave a value of 8.3 ± 1 kcal/mole for the singlet-triplet energy splitting.

The studies mentioned above and other similar experiments are all consistent with a CH_2 ($^3B_1$) - CH_2 ($^1A_1$) splitting of 8.5 ± 1 kcal/mole, but the most direct observation of the splitting, the photoelectron spectrum from the photodetachment of CH_2^- to produce CH_2 ($^1A_1$) and CH_2 ($^3B_1$) has been interpreted to show a splitting of either 19.5 or 23.2 kcal/mole.[1] There are several possible explanations for this apparent contradiction. If the singlet-triplet splitting is indeed about 8.5 kcal/mole, then the photoelectron spectrum is not correctly assigned, and perhaps hot bands of CH_2^- are being observed.[9,10] Franck-Condon factors for the photodetachment of an electron from CH_2^- have been calculated from ab initio potential curves and fit the observed spectra well if it is assumed that hot bands are present.[9] This assignment predicts a $^1A_1$ - $^3B_1$ splitting of 9 ± 1 kcal/mole, but extensive experimental work attempting to confirm the presence of hot bands has tended to show that the observed features are not due to vibrationally excited CH_2^-.[1] If the methylene singlet-triplet splitting is actually around 20 kcal/mole, then it is difficult to explain the photochemical and photoionization results. An upper bound for ΔH^o_{fo} CH_2 ($^1A_1$) is firmly established, within the accuracy of the corrections for the effects of reactant internal excitation to photodissociation (±1 kcal/mole). Thus for the splitting to be as large as 20 kcal/mole the apparent thresholds in the photolysis and dissociative photoionization experiments used to determine ΔH_f CH_2 ($^3B_1$) must be 11.5 kcal/mole higher than the actual thermodynamic limit and this amount of excess energy must be released at the threshold. The reduc-

tion of the heat of formation of CH_2 ($^3B_1$) by as much as 10 kcal/mole is also not compatible with the results of many chemical activation studies of unimolecular decomposition.[11]

Many theoretical studies of methylene energy levels have been performed, and the most extensive ab initio calculations have given the values 10.4 ± 2,[12] 10.5,[13,14] 10.6,[15] and 11.0 kcal/mole[10] for the singlet-triplet splitting. There is still a question of the exact correction to these calculations necessary to account for the differences in zero point energy of the two states. Harding and Goddard[9] calculated total zero point energies using the harmonic approximation and found a very small (0.16 kcal/mole) difference between the singlet and triplet. The result (10.4 kcal/mole) was corrected for this effect. Thus the theoretical results tend to support the lower (~8.5 kcal/mole) experimental value for the splitting but do not accurately agree with it.

By detecting the products of the photofragmentation of ketene in a molecular beam experiment, many of the uncertainties in other measurements of the methylene singlet-triplet splitting can be avoided. In particular the velocity of the fragments can be directly measured and the translational energy distribution determined. The maximum translational energy released in the dissociation should correspond to the production of ground state CH_2 and CO, and even if there is a barrier for dissociation, the potential energy will be transformed into product translational and internal energy. A further advantage is that the expansion which produces the molecular beam cools the ketene sufficiently so that its internal energy can be neglected.

EXPERIMENTAL

The experiments were performed in a crossed molecular beams machine, with a laser replacing one of the molecular beam sources. The laser and molecular beams cross at 90° in an interaction chamber, where the pressure is maintained at about 1×10^{-7} torr. The detector is a quadrupole mass spectrometer which can be rotated around the crossing point in the plane determined by the two beams. Photofragments which pass through the detector entrance slit and two stages of differential pumping enter the ionization chamber where they are ionized by electron impact. The slits used were chosen to give a laboratory angular resolution of 2.5°. The neutral products travel a distance of 34.1 cm to the ionizer after dissociation. The ions pass through the quadrupole mass selector to a Daly detector. The time interval between the laser pulse and the detection of the products is recorded in a multichannel scaler, allowing the fragment's recoil velocity to be determined.

Ketene was prepared by pyrolysis of acetic anhydride and trapped at 77°K. A portion was purified for use each day by trap to trap distillation. A supersonic beam of ketene seeded in helium was produced by bubbling helium through liquid ketene in a dry ice–ethanol bath, and expanding the resulting mixture at 300 torr through a 0.22 mm nozzle. After passing through two stages of differential pumping and collimation, the beam, with a spread of 2.5°, entered the interaction chamber. The beam of ketene had a peak velocity of 1.12×10^5 cm/sec and a full width at half maximum velocity spread of about 10%. The

density of ketene in the interaction region was about 10^{11} molecules/cc.

A Lumonics Model TE-861 rare gas halide excimer laser was used at 351 nm (XeF) and 308 nm (XeCl) for the photodissociation. The laser beam was focused to a spot of about 0.5 cm diameter where it crossed the molecular beam and was operated at 70 Hz with a measured average power of about 2.5 watts at both wavelengths.

RESULTS AND ANALYSIS

The data obtained in this experiment consist of time-of-flight distributions which are proportional to the number density of the detected product present in the mass spectrometer ionizer as a function of time after the laser pulse. To determine the thermochemical quantities of interest the data must be converted to energy distributions in the center-of-mass coordinate system of the dissociating molecule. Figure 1 shows a velocity vector diagram for the process. The origin of the lab coordinate system is the base of the beam velocity vector and lab angles are measured from the direction of the beam. The tip of this vector defines the origin of the center-of-mass coordinate system and the circles show CO fragment velocities corresponding to various product translational energies.

It was found necessary to make a small background correction to the raw data, as a result of the large detector apertures used to enhance the signal to noise ratio in this experiment. These large apertures allow some product molecules to strike surfaces of the ionizer and raise the background for a short time after each laser pulse. The background then decays exponentially with a time constant determined by the pumping speed for that molecule. Correction for this minor effect was made by requiring the background for times where signal cannot appear due to kinematic constraints to be equal to the background before the first signal arrived. The behavior of the time dependent background was simulated with an amplitude proportional to the intensity of signal, and a decay constant roughly corresponding to the pumping speed, and then subtracted from the data. These two parameters

could be varied until the proper background level was obtained. An example of original and corrected data is shown in Fig. 2. All further CO data shown in Figs. 3 and 5 have been corrected in this manner. The problem does not appear for CH_2, apparently because it is rapidly destroyed by wall collisions.

The determination of the center-of-mass energy distribution is done by an iterative process. A trial energy and angular distribution is used as the input to a computer simulation program. The energy distribution is converted to center-of-mass velocity flux according to the relation:

$$I_{c.m.}\ (u,\theta_{cm}) \propto u\ I_{cm}\ (E_{cm},\ \theta_{cm})$$

This is then transformed to laboratory time-of-flight.

$$N_{LAB}\ (t,\theta_{LAB}) \propto \frac{v^3}{lu^2}\ I_{cm}(u,\theta_{cm})$$

where l is the flight path, and v and u are lab and c.m. velocities respectively. The beam velocity and angular spreads are accounted for by summing the contributions due to different initial speeds and angles. The detector resolution is included in a similar fashion. The result for a given center-of-mass energy distribution was compared to the data, and the input changed until the agreement was satisfactory. The center-of-mass distributions used had the form

$$I_{cm}(E_{cm},\ \theta_{cm}) = P(E_{cm})\ D\ (\theta_{cm}).$$

The energy distribution itself was

$$P(E) = C(E - E_1)^{\alpha}\ (E_T - E)^{\beta}.$$

For convenience in fitting the data the actual parameters used in the computer simulation were E_p, the energy at which the distribution peaks; $E_p - E_1$, the difference between the peak and the low energy at which the probability goes to zero; and $E_T - E_p$, the difference between the high energy where the probability goes to zero and the peak. The parameter α can then be calculated given, β, E_p, E_1 and E_T, as

$$\alpha = \frac{\beta(E_p - E_1)}{E_T - E_p} \quad .$$

Several distributions could be added together to produce the best fit to the data.

For each laser frequency an energy and angular distribution was chosen which most closely fits all the data taken at different angles. The results for the XeF laser at 351 nm are shown in Fig. 3. The fit (solid line) is superimposed on the data (solid dots). An angular distribution of $1 + \sin^2\theta$ produced the best agreement with the data. The time-of-flight for CO products could be fit with the same energy distribution at the two angles, but for the CH_2 product the entire distribution had to be shifted 0.5 kcal/mole to higher energy. For determining the thermodynamic quantities discussed later, the center-of-mass energies consistent with the data from the CO fragment were used since the signal to noise ratio is much better than for the CH_2 fragment. The energy distribution is shown in Fig. 4, and the actual values used for the parameters are shown in Table 1. Figure 3 also shows the result of calculations of the laboratory time-of-flight at 14° if the center-of-mass energies are shifted up and down by 1 kcal/mole without changing the

shape of the energy distribution. This gives an idea of the sensitivity of the experiment. The results for the CO fragment when ketene is dissociated with the 308 nm light from the XeCl laser are shown in Fig. 5. All angles are fit with the same energy distribution as shown in Table 1, and an angular distribution $1 + \cos^2\theta$ was used. The energy distribution is shown in Fig. 6. Again the sensitivity to energy shifts of ±1 kcal/mole are shown (Fig. 5) for a lab angle of 14°. Because of the larger product translational energy released at this frequency the sensitivity to the threshold of the energy distribution is less than that at 351 nm.

From the energy distributions determined in this experiment several thermochemical quantities related to ketene dissociation can be derived. The expansion producing the supersonic beam using He carrier gas cools the ketene sufficiently that it can be assumed the molecule starts essentially in its ground vibrational and rotational state. A photon of known energy is absorbed, and we then measure the translational energy of the fragments. Because the sum of the translational energy and internal energy is the excess energy available for dissociation, the fastest products detected should correspond to ground state CO and CH_2 formation. Several previous experiments[6,7,16] have shown that the threshold for CH_2 ($^1A_1$) production from ground state ketene is substantially above the energy supplied by a 351 nm photon, so the signal at this wavelength must be due entirely to CH_2 ($^3B_1$). From the distribution in Fig. 4 the highest translational energy observed in the products is 3.8 kcal/mole. When this is subtracted from the 81.4 kcal/mole supplied by the photon it gives a value of

77.6 kcal/mole for the bond dissociation energy of CH_2CO to CH_2 ($^3B_1$) and CO. Photons at 308 nm from the XeCl laser energetically could produce both singlet and triplet methylene, but we observed only singlet. If triplet products were produced they would be considerably faster than the fastest signal observed. Figure 7 shows a simulated time-of-flight spectrum from an energy distribution which is the same as that used to fit the data at 308 nm, except for the addition of a second distribution at an energy corresponding to that expected for the triplet, as determined from the result at longer wavelength. The second distribution has a peak 10% as high as the peak of the singlet distribution. The actual data show no similar features in the corresponding position. Thus the highest translational energy products are assumed to be ground vibrational and rotational state CH_2 ($^1A_1$) and CO. Subtracting the translational energy (6.7 kcal/mole) of these products from the laser photon energy of 92.8 kcal/mole results in 86.1 kcal/mole for the bond dissociation of ketene to produce CH_2 ($^1A_1$) and CO. Thus the energy difference between the singlet ($^1A_1$) and triplet ($^3B_1$) states of CH_2 is 8.5 kcal/mole, with an uncertainty of approximately 0.8 kcal/mole, mainly from the experimental determination of the maximum translational energy release. These results are summarized in Fig. 8.

From the known heats of formation of CH_2CO (ΔH^o_{fo} = - 10.7 kcal/mole)[17] and CO (ΔH^o_{fo} = - 27.199 kcal/mole),[18] the heat of formation of CH_2 can be calculated from the measured bond dissociation energies of CH_2CO.

$$\Delta H^o_{fo}\ (CH_2\ {}^3B_1) = 77.6\ \text{kcal/mole} + \Delta H^o_{fo}\ (CH_2CO) - \Delta H^o_{fo}\ (CO) = 94.1\ \text{kcal/mole}$$

$$\Delta H^o_{fo}\ (CH_2\ {}^1A_1) = 86.1\ \text{kcal/mole} + \Delta H^o_{fo}\ (CH_2CO) - \Delta H^o_{fo}\ (CO) = 102.6\ \text{kcal/mole}$$

DISCUSSION

The value for the singlet-triplet splitting obtained from this work (8.5 kcal/mole) agrees very well with the lower value from previous experiments. The actual heats of formation derived from our results also compare favorably with those previously determined. The very close agreement of the photoionization value for ΔH^{o}_{fo} CH_2 $(^3B_1)$[4,5] with the number from our experiments, where translational energy release is observed directly, strongly supports the assumption that there is no excess energy release at the threshold of ionization. It also tends to confirm that the fastest products we observed from dissociation with 351 nm photons do correspond to ground vibrational state CO and CH_2.

The threshold for the process

$$CH_2CO \xrightarrow{h\nu} CH_2\ (^1A_1) + CO$$

measured in several experiments are in fairly close agreement. In the work of Lengel and Zare the value 85.2 ± 0.3 kcal/mole was obtained.[6] The similar experiments of reference 7 yielded 85.4 ± 0.3. Simons and Curry found 84.4 ± 0.6 kcal/mole, for the process at 298K.[8] All of these determinations rely on the translational energy release being negligible at the threshold. Again the assumption seems to be valid as our value of 86.1 ± 0.5 kcal/mole agrees fairly well if the uncertainty in corrections of previous results for reactant internal energy is considered.

A large discrepancy exists between the results of this work, and the photodetachment results from CH_2^-, which support a large singlet-

triplet splitting (19.5 kcal/mole).[1] As previously discussed, an upper limit can be placed on the energy of the CH_2 ($^1A_1$) state from previous experiments as well as from this work, so possible errors resulting in too small a value for the splitting must arise from placing the energy of the ($^3B_1$) state too high. If the photodissociation of ketene at 351 nm produces no ground vibrational state products then the value of ΔH^o_{fo} CH_2 ($^3B_1$) determined in this experiment would be too high. This is very unlikely for several reasons. The heat of formation of triplet methylene we obtained agrees closely with previous measurements by completely different methods. It's difficult to imagine that identical errors appear in each case. In addition, if the splitting were as large as 19.5 kcal, then 15 kcal/mole are available to the products in the ketene dissociation at 351 nm. A maximum of 3.8 kcal/mole appears as translation in our experiments. If there were at least another 11.0 kcal/mole of energy in the internal excitation of products, the product vibrational states would be very highly inverted. This is not expected since the CO vibration and the CH_2 bending vibration both are strongly coupled to the reaction coordinate of the photodissociation of ketene, and the CO bond length in CH_2CO is quite close to that of CO.

There are several other interesting features of the center-of-mass energy distributions determined in this experiment. The shapes of the distribution of product energy at the two wavelengths are obviously very different. For the triplet (from 351 nm dissociation) the product is fairly sharply peaked near the maximum translational energy release. The second smaller peak in Fig. 4 is necessary to fit the small

feature in the time-of-flight data at 14°. The spacing between the two peaks is approximately equal to the energy of the bending vibration in ground state CH_2 (3.4 kcal/mole).[1] This suggests that a small fraction of the CH_2 is produced vibrationally excited. The translational energy distribution for singlet CH_2 production from 308 nm dissociation (Fig. 6) peaks at zero translational energy and is very broad. This shows that there is substantial internal excitation of the products. The drastic change in the dissociation dynamics between 351 nm and 308 nm and the exclusive production of CH_2 ($^1A_1$) at 308 nm might suggest that different electronic states of ketene are involved at these two frequencies. The difference between the angular dependence of the product intensity at the two wavelengths is further evidence that the dissociation process changes in this wavelength region, but due to the limited angular range covered in these measurements our data are not sufficient to provide precise information on the angular distribution.

There is still some disagreement between the results of ab initio calculations of the singlet-triplet splitting (~10.5) and the experimental determination (~8.5 kcal/mole), although considering the uncertainty of ±1 kcal/mole in each of these values they are not incompatible. A very recent, large scale CI calculation involving 60,000 configurations[13] has not brought the numbers any closer to agreement, but correction for the difference in zero point enegies was found to reduce the energy difference by 0.6 kcal/mole.[19] A small relativistic correction, at most 0.1 kcal/mole,[20,21] could reduce the calculated value of the splitting to 9.8 kcal/mole. It has also been sug-

gested,[15] based on comparison of extensive CI calculations with experimental measurements of excited state energies for carbon atoms and CH, that the value for the singlet-triplet splitting in CH_2 from CI calculations is still somewhat too high and the actual separation is less than 10 and perhaps as small as 9 kcal/mole.

CONCLUSION

This chapter has described the measurement of the energy splitting between the ground ($^3B_1$) and first excited ($^1A_1$) states of methylene. The experiment was especially designed to detect posssible barriers to photodissociation which potentially could have caused errors in previous results. No evidence for such barriers was observed, and our value of 8.5 kcal/mole agrees well with the majority of other experiments attempting to measure the singlet-triplet splitting.[2,3,6,7,8,22] It is also in reasonable agreement with recent ab initio quantum mechanical calculations,[10,12,13,14,15] but not with the larger value obtained from the photoelectron spectrum of photodetachment from CH_2^-.[1]

REFERENCES

1. P. C. Engelking, P. R. Corderman, J. J. Wendoloski, G. B. Ellison, S. V. O'Neil, and W. C. Lineberger, J. Chem. Phys. 74, 5460 (1981).
2. F. Lahmani, J. Phys. Chem. 80, 2623 (1976).
3. H. M. Frey and G. J. Kennedy, J. Chem. Soc. Faraday Trans. 1, 73, 164 (1977).
4. K. E. McCoulloh and V. H. Dibeler, J. Chem. Phys. 64, 4445 (1976).
5. W. A. Chupka and C. Liftshitz, J. Chem. Phys. 48, 1109 (1978).
6. R. K. Lengel and R. N. Zare, J. Am. Chem. Soc. 100, 7495 (1978).
7. D. Feldman, K. Meier, H. Zacharias, and K. H. Welge, Chem. Phys. Lett. 59, 171 (1978).
8. J. W. Simons and R. Curry, Chem. Phys. Lett. 38, 171 (1976).
9. L. B. Harding and W. A. Goddard III, Chem. Phys. Lett. 55, 217 (1978).
10. Shing-Kuo Shih, S. D. Peyerimhoff, R. J. Buenker, and M. Peric, Chem. Phys. Lett. 55, 206 (1978).
11. B. S. Rabinovich, private communication.
12. L. B. Harding and W. A. Goddard III, J. Chem. Phys. 67, 1777 (1977).
13. P. Saxe, H. F. Schaefer III, and N. C. Handy, J. Phys. Chem. 85, 745 (1981).
14. B. O. Roos and P. M. Siegbahn, J. Am. Chem. Soc. 99, 7716 (1977).
15. C. W. Bauschlicher, Jr. and I. Shavitt, J. Am. Chem. Soc. 100, 739 (1978).
16. D. L. Monts, T. G. Dietz, M. A. Duncan, and R. E. Smalley, Chem. Phys. 45, 133 (1980).

17. R. L. Nuttall, A. H. Laufer, and M. V. Kilday, J. Chem. Thermodyn. 3, 167 (1978).

18. D. R. Stuhl and H. Prophet. eds. JANAF thermochemical tables, 2nd Ed., NBS publication 37 (1971).

19. H. F. Schaefer III, private communication.

20. K. Balasubramanian, P. Saxe, P. A. Christiansen, K. S. Pitzer, and H. F. Schaefer III, submitted to J. Chem. Phys.

21. E. R. Davidson, D. Feller, and P. Phillips, Chem. Phys. Lett. 76, 416 (1980).

22. F. S. Rowland, C. McKnight, and E. K. C. Lee, Berichte der Bunsengesellshaft fur Physikalische Chemie, Bd. 72, Nr. 2, 236 (1960).

Table 1. Center-of-mass energy distribution parameters for the photodissociation of CH_2CO. Energies are in kcal/mole.

	E_p	E_T-E_p	E_p-E_1	β	Peak Height
351 nm dissociation CO product at 14° and 17°					
High energy peak	2.3	1.5	1.2	2.5	1.0
Low energy peak (Fig. 3 and Fig. 4)	0.45	0.40	0.40	1.3	0.3
351 nm dissociation CH_2 product at 35° (Fig. 3)	2.8	1.5	1.2	2.5	1.0
308 nm dissociation CO product at 14°, 17°, 20° and 25° (Fig. 5 and Fig. 6)	0.0	6.7	0.0	1.2	1.0
308 nm dissociation CO product at 14°					
Singlet	0.0	6.7	0.0	1.2	1.0
Triplet (Fig. 7)	9.2	6.0	4.8	2.5	0.1

FIGURE CAPTIONS

Fig. 1. Newton diagram for photodissociation of CH_2CO showing relations between laboratory and center-of-mass velocities and angles. V_{CH_2CO} and V_{CO} are laboratory velocity vectors, U_{CO} is a center-of-mass velocity vector. The origin of the lab coordinate system is the base of the vector for the initial CH_2CO velocity, and the origin for the center-of-mass system is the tip of the same vector. The circles have radii corresponding to the speed of the CO fragment in the center-of-mass frame for various amounts of translational energy release in the dissociation.

Fig. 2. Time-of-flight data at a lab angle of 14° for the CO fragment from CH_2CO photodissociation at 308 nm. The dots are the original data, and the solid line shows the data after subtraction of time dependent background. N(t) is the number of counts as a function of time (arbitrary units).

Fig. 3a. Time-of-flight data for fragments from ketene photodissociation at 351 nm. N(t) is the number of counts per time channel (arbitrary units). Dots are the data, the solid lines are the fits. E_T is the highest center-of-mass energy (kcal/mole) with non-zero probability in the energy distributions used for the computer simulation. The energy distribution has been shifted ±1 kcal/mole to show the sensitivity of the fits.

Fig. 3b. Time-of-flight data and computer generated fits for the CO fragment at 17° lab angle and the CH_2 fragment at 35° lab angle from ketene photodissociation with the laser operated at 351 nm.

Fig. 4. Center-of-mass energy distribution for ketene photofragmentation at 351 nm. The energy scale is in kcal/mole. This distribution was used to fit the data for the CO fragment at lab angles of 14° and 17°. The actual parameters are given in Table 1.

Fig. 5a. Time-of-flight data for the CO fragment from ketene photodissociation at 308 nm and 14° lab angle. N(t) is the number of counts per time channel (arbitrary units). Dots are the data, lines are the computer generated fits. The time-of-flight spectrum has been calculated for the center-of-mass energy distribution with parameters shown in Table 1, and with E_T shifted ± 1 kcal/mole.

Fig. 5b. Time-of-flight data and computer generated fits for the CO fragment from photodissociation of ketene at 308 nm and various lab angles.

Fig. 6. Center-of-mass energy distribution for ketene photodissociation at 308 nm. Energy scale is in kcal/mole. The distribution shown was used to fit all the CO time-of-flight data from the 308 nm dissociation. The parameters for this distribution are given in Table 1.

Fig. 7. The dots show the time-of-flight data for the CO fragment at 14° from CH_2CO photodissociation with 308 nm light. The solid line is the computer calculated time-of-flight spectrum for CO fragments if a center-of-mass energy distribution corresponding to CH_2 ($^3B_1$) production at this wavelength is added to the distribution actually used to fit the data. The parameters used to generate this figure are shown in Table 1.

Fig. 8. Energy level diagram for the ketene photodissociation process. All energies shown are in kcal/mole.

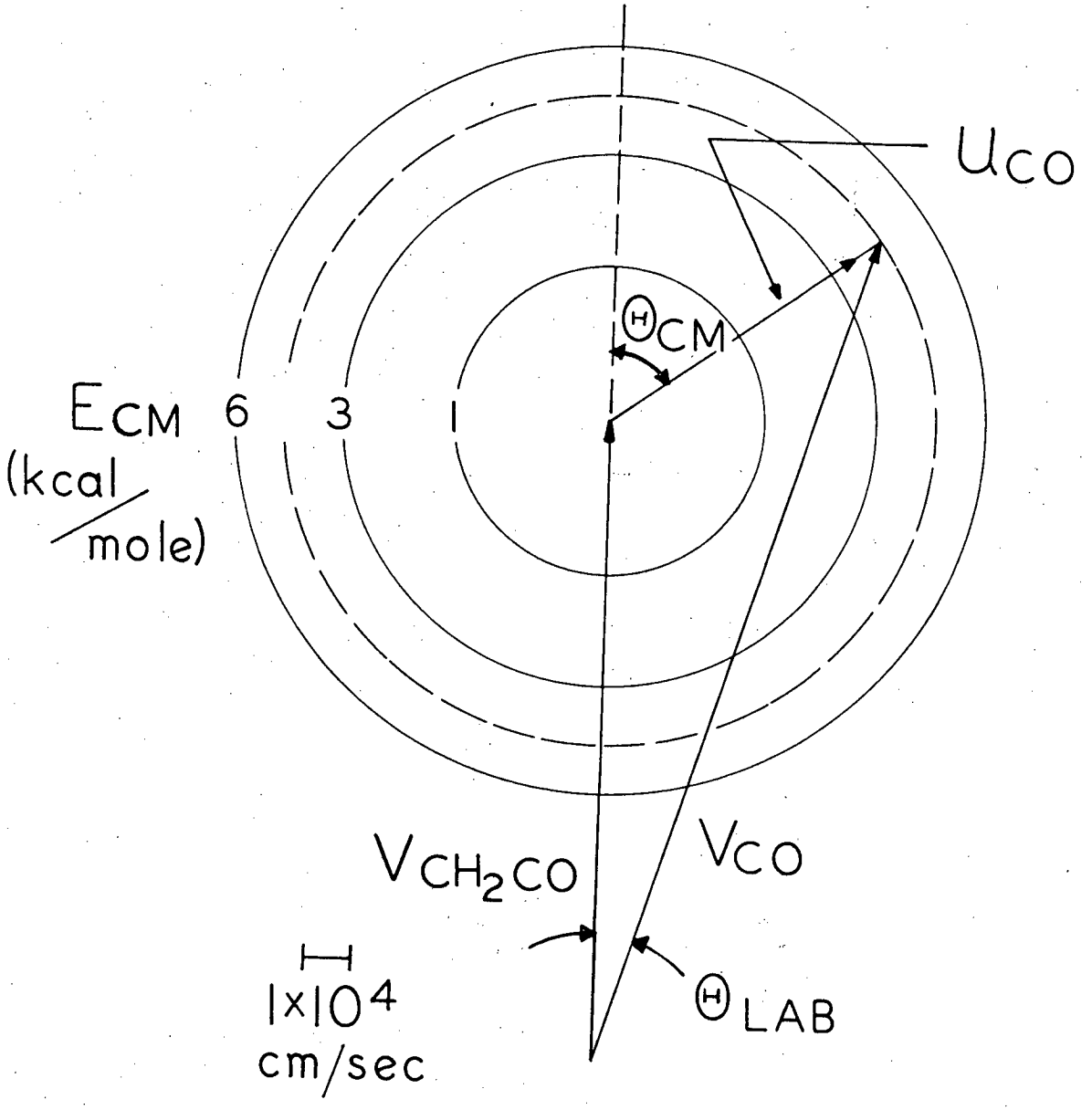

Fig. 1. XBL 811-7778

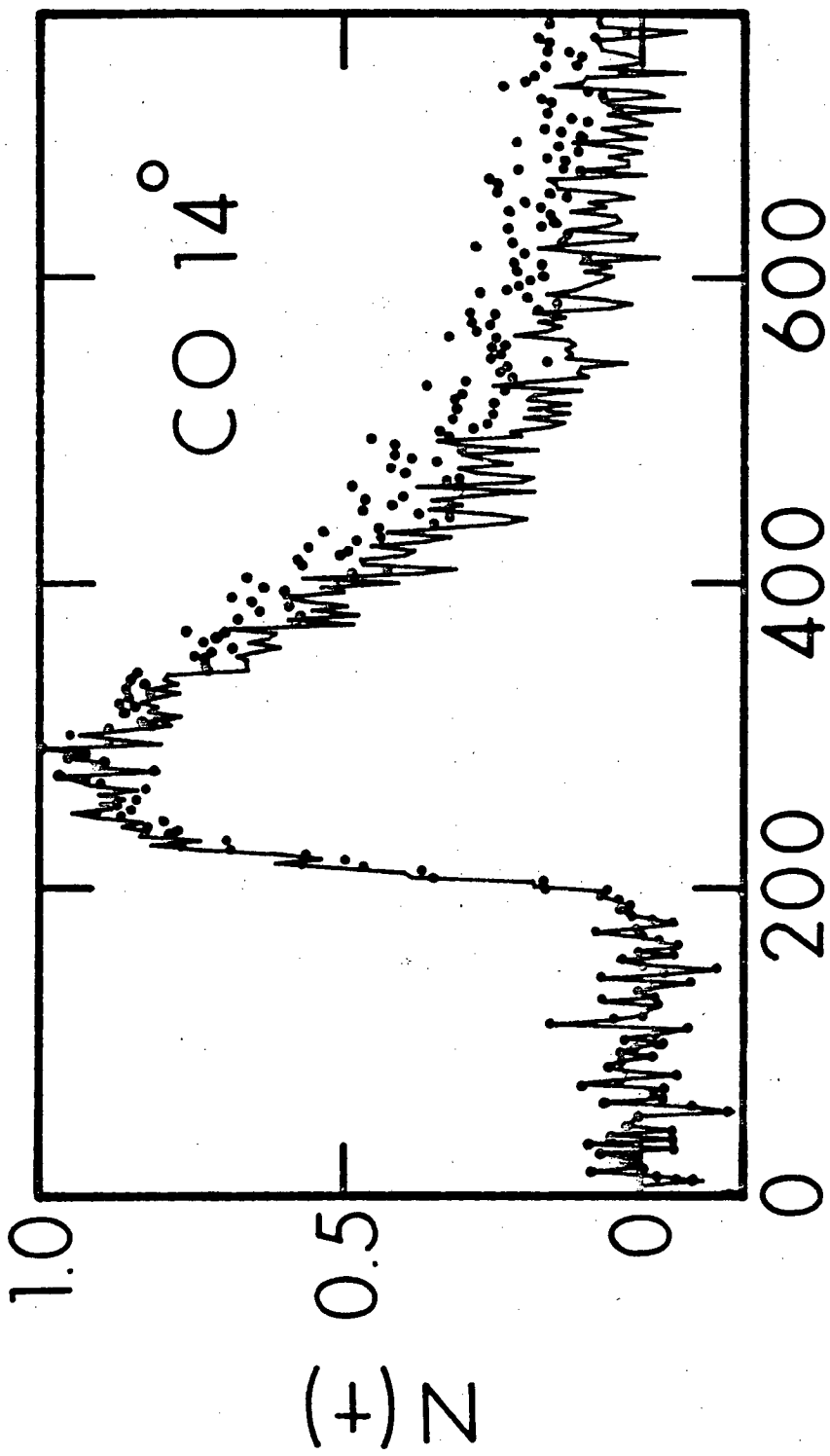

XBL 819-1991

Fig. 2.

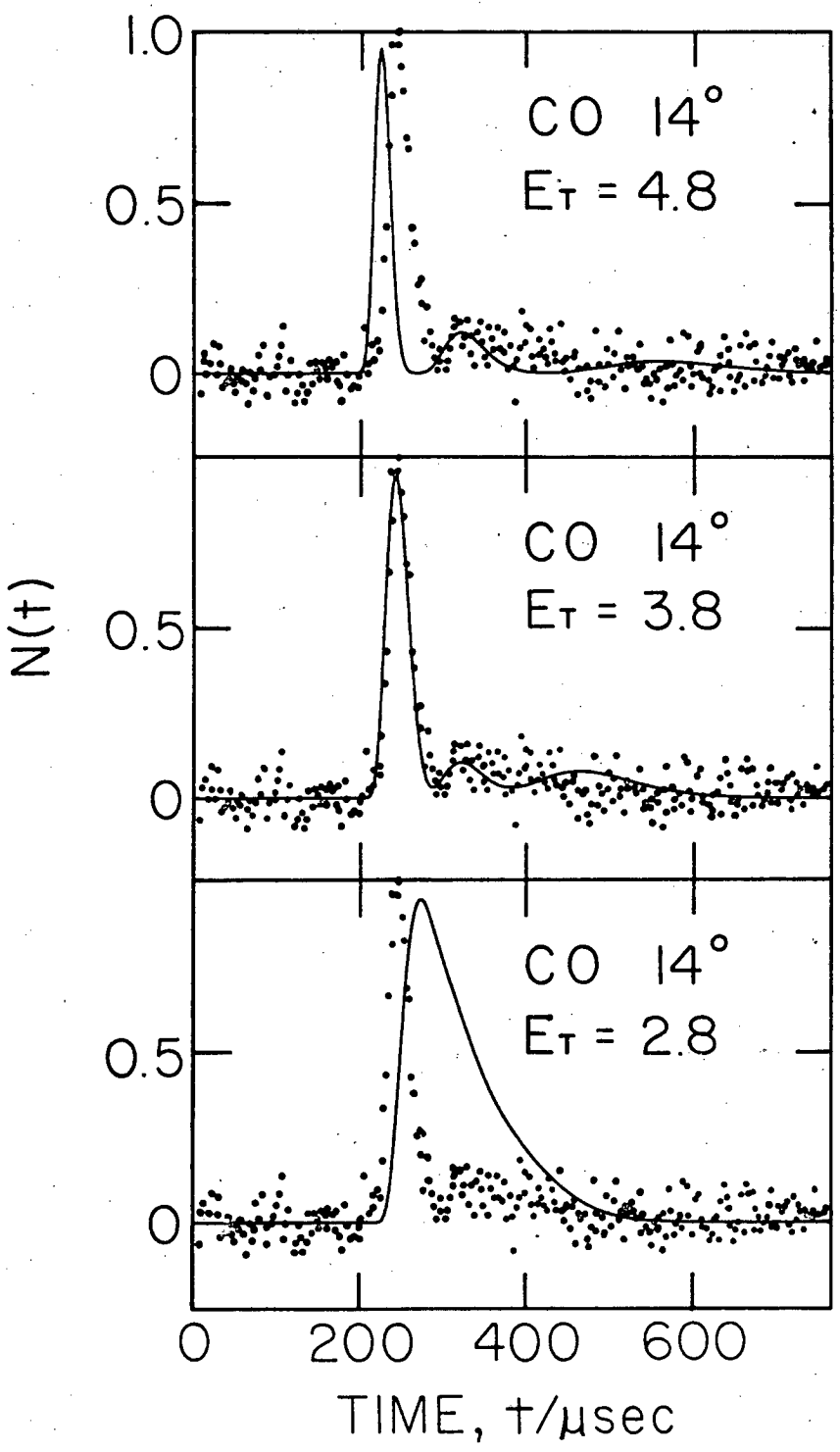

XBL 819-1797

Fig. 3a.

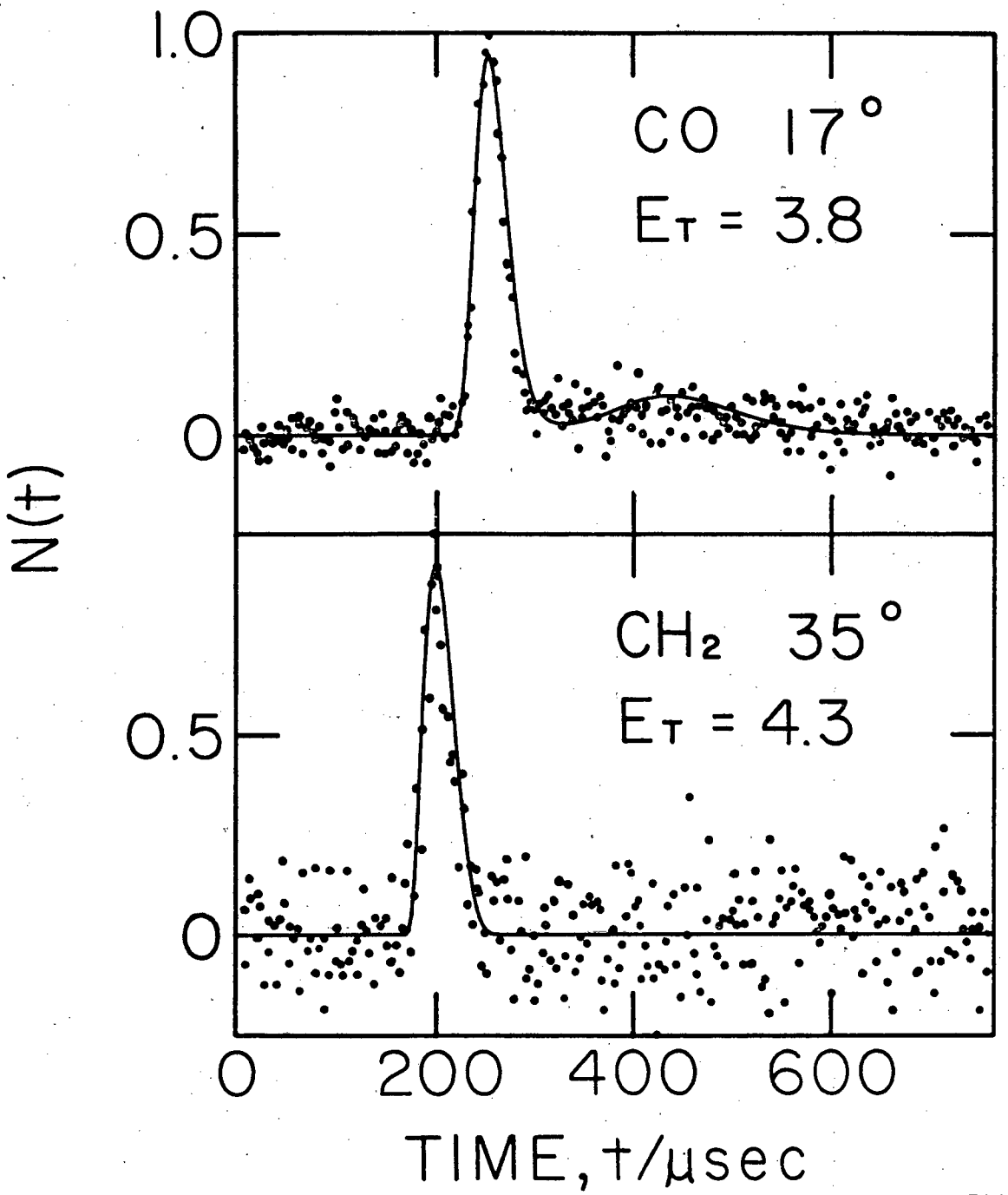

XBL 819-1796

Fig. 3b.

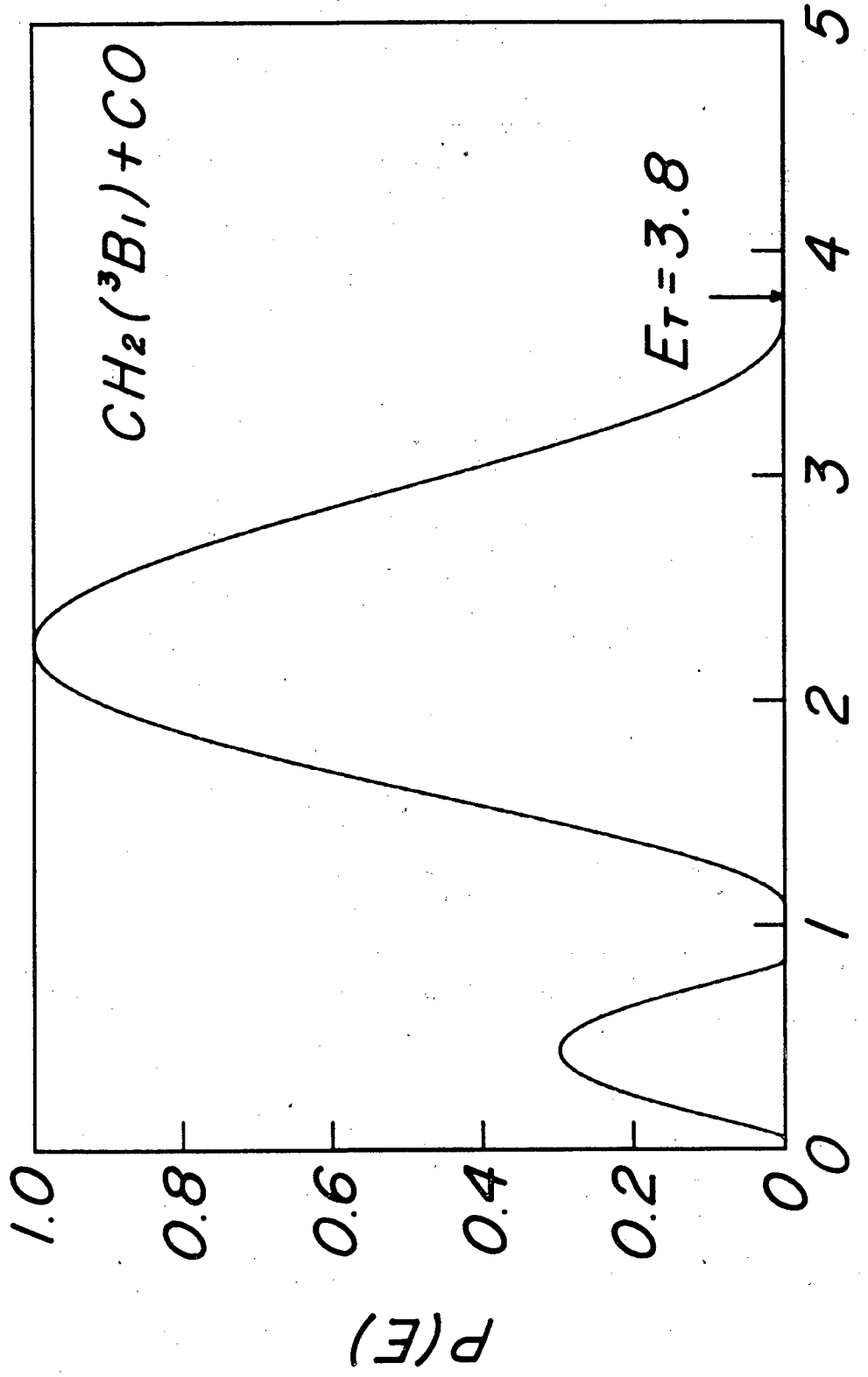

XBL 811-7782

Fig. 4.

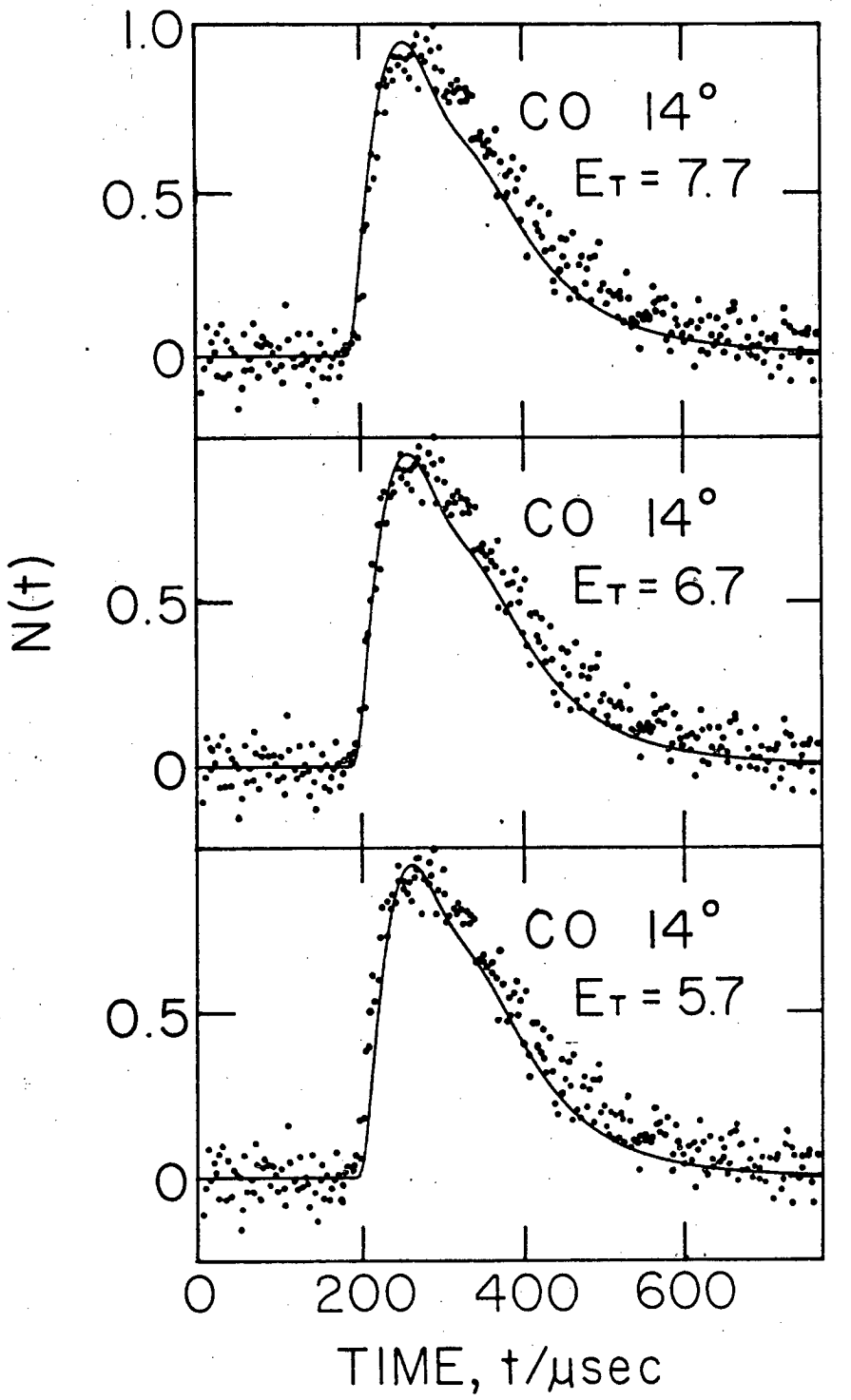

XBL 819-1798

Fig. 5a.

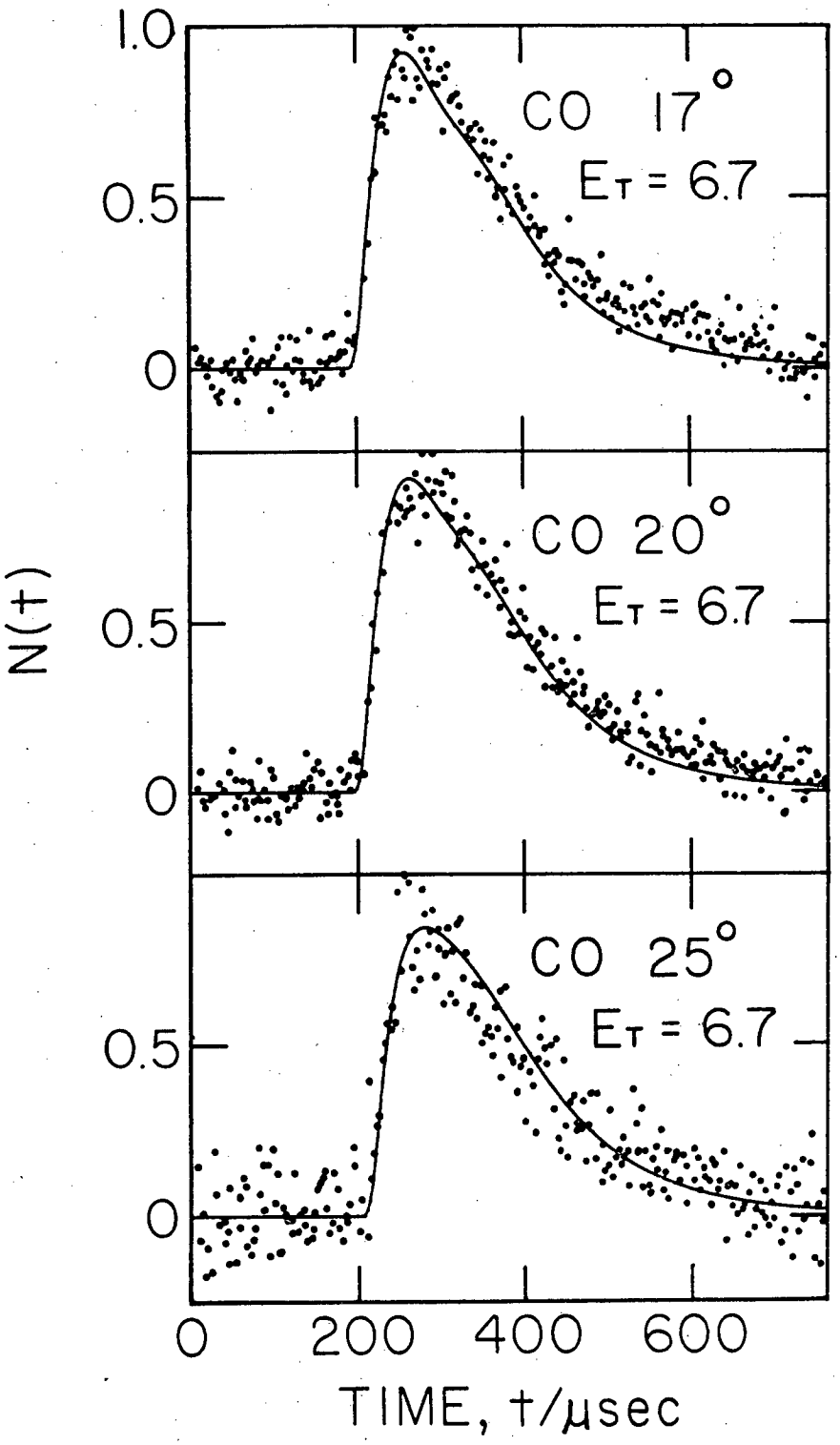

Fig. 5b. XBL 819-1795

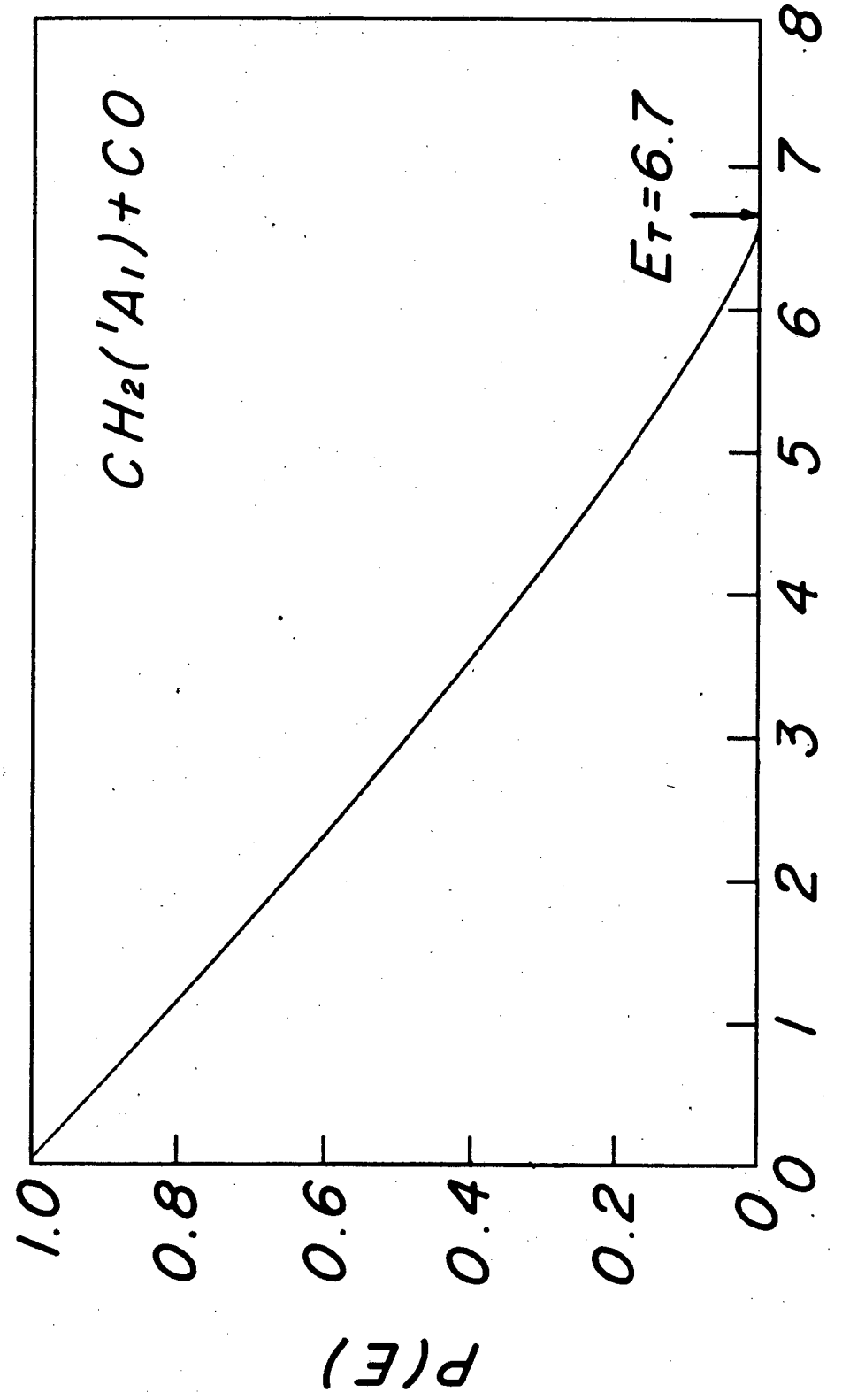

XBL 811-7783

Fig. 6.

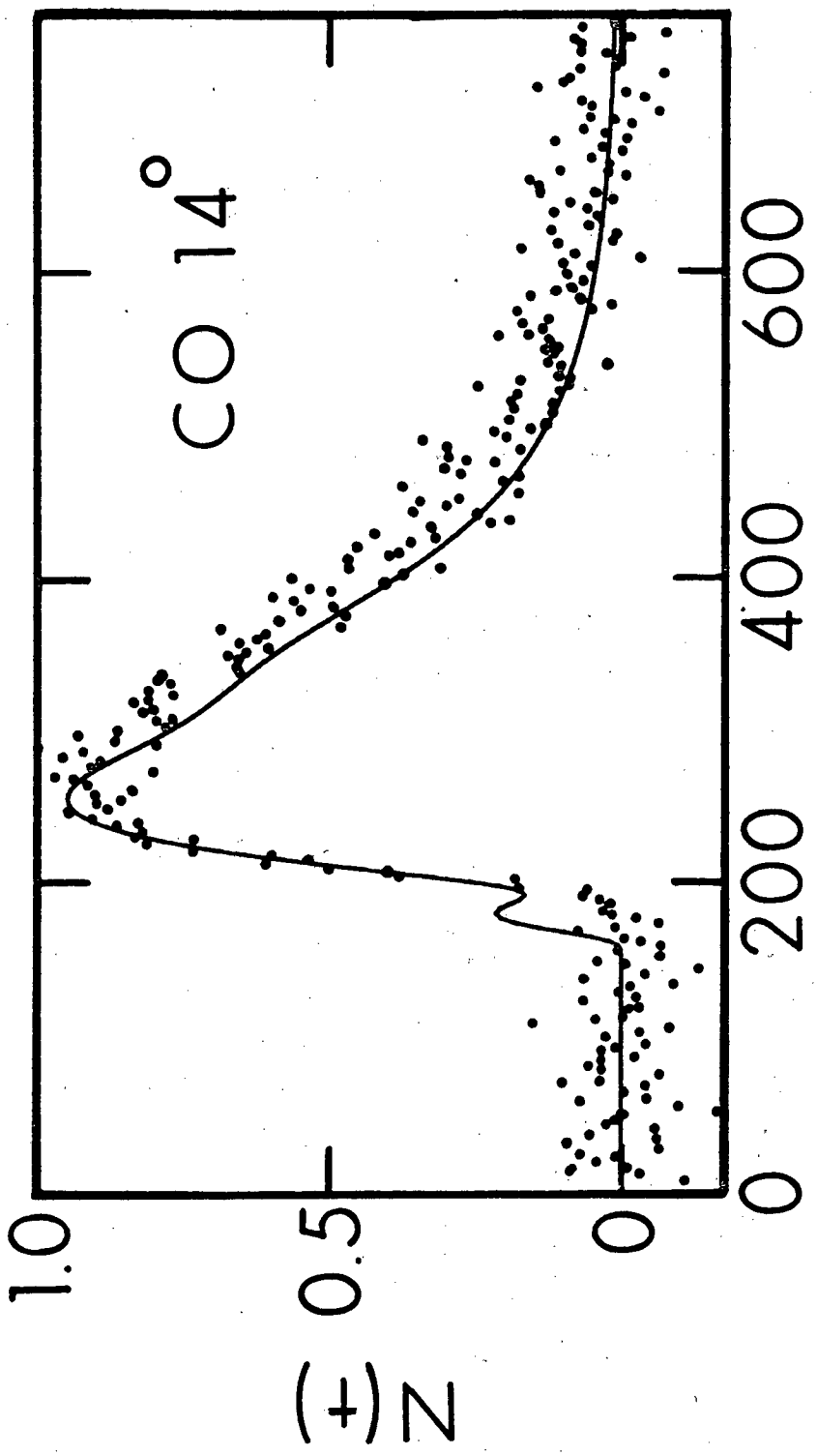

XBL 819-1992

Fig. 7.

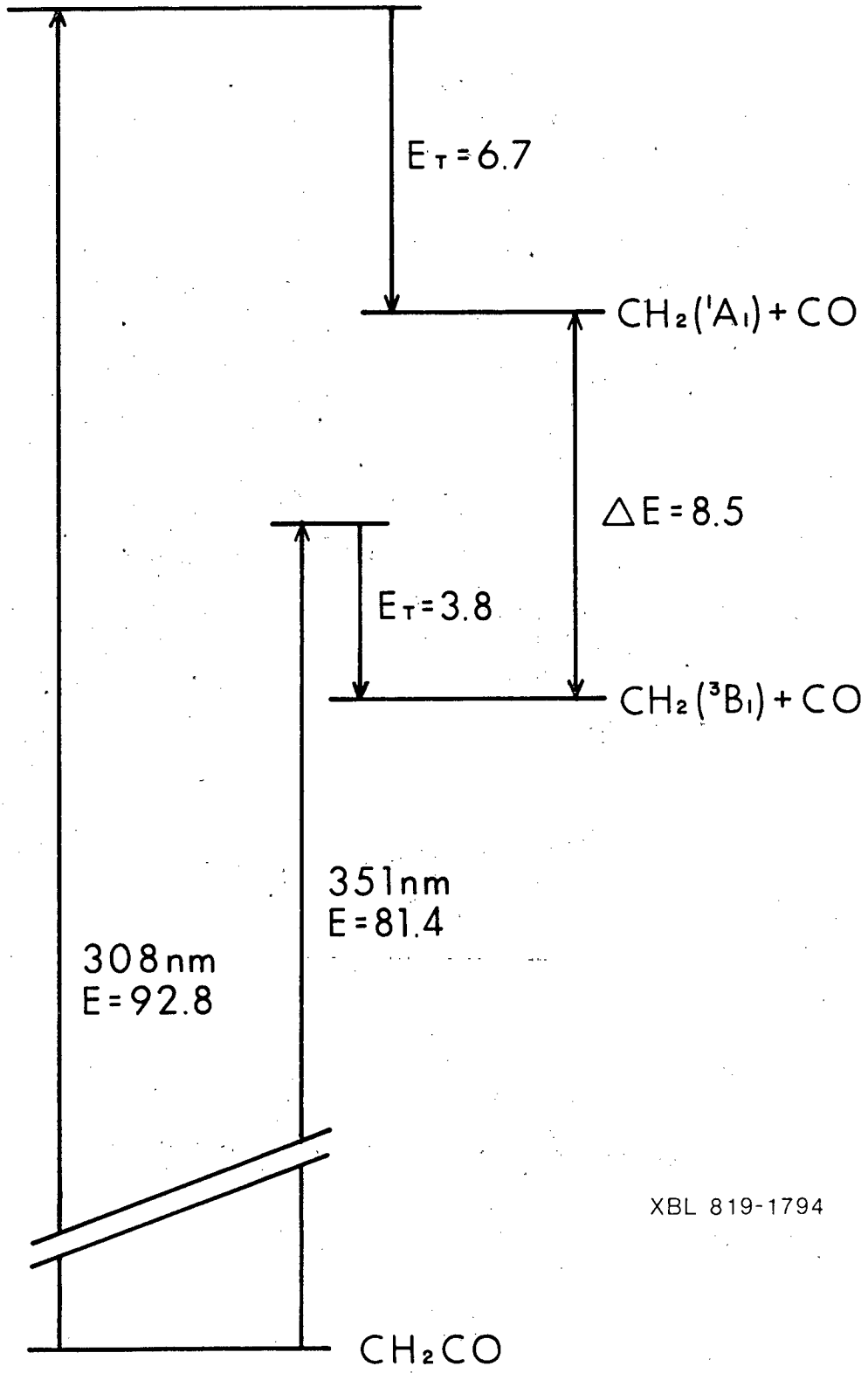
E T = 6.7
CH2 (1A1) + CO
△E = 8.5
E T = 3.8
CH2 (3B1) + CO
351nm
E = 81.4
308nm
E = 92.8
CH2CO
XBL 819-1794

Fig. 8.

TECHNICAL INFORMATION DEPARTMENT
LAWRENCE BERKELEY LABORATORY
UNIVERSITY OF CALIFORNIA
BERKELEY, CALIFORNIA 94720